CENTRO DE INVESTIGACIÓN Y DE ESTUDIOS AVANZADOS
DEL INSTITUTO POLITÉCNICO NACIONAL

UNIDAD ZACATENCO
DEPARTAMENTO DE FÍSICA

"Perspectivas para Medir Secciones Eficaces de Neutrinos en Detectores Cercanos (ICARUS y similares a DUNE-PRISM) y sus Implicaciones para Física de Precisión"

Tesis que presenta

Guadalupe Moreno Granados

para obtener el Grado de

Doctora en Ciencias

en la Especialidad de

Física

Director de tesis: Dr. Omar Gustavo Miranda Romagnoli
Dra. Minerba Betancourt

Ciudad de México Julio, 2024

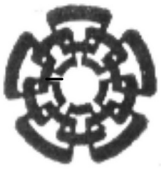

CENTER FOR RESEARCH AND ADVANCED STUDIES OF THE
NATIONAL POLYTECHNIC INSTITUTE

UNIT ZACATENCO
PHYSICS DEPARTMENT

“Perspectives for Measuring Neutrino Cross-Sections at Short Baseline Detectors (ICARUS and DUNE-PRISM-like Detector) and Their Implications for Precision Physics”

by

Guadalupe Moreno Granados

In order to obtain the

Doctor of Science

degree, speciality in

Physics

Advisor: Ph. D. Omar Gustavo Miranda Romagnoli
Ph. D. Minerba Betancourt

Mexico City July, 2024

Acknowledgments

I would like to express my deepest gratitude to everyone who has supported and guided me throughout my academic journey.

I will always lack words to express the gratitude I have for my family. To my mom, my dad, my brother Alex, and my sister Sere, thank you for your wholehearted support and love. Thank you for believing in me and for encouraging me to pursue my dreams. I couldn't have done this without you.

Similarly, I would like to express my immense gratitude to my advisors Omar Miranda and Minerba Betancourt. Your mentorship, support, understanding, and patience have been invaluable. Thank you for guiding me through this challenging journey, for your constant encouragement, and for helping me grow as a researcher.

To my synods Alexis Aguilar, Mauricio Carbajal, Luis Manuel Montaño, and Pablo Roig, I am grateful for your time, insights, and feedback. Your expertise has been crucial in shaping my research, and I appreciate your dedication to my academic progress.

In particular, I would like to express my gratitude to Steven Dytman for your time, insights, and suggestions for my research. I also appreciate the guidance, mentorship, and hospitality of Abigail Waldron, Linda Cremonesi, and Alex Booth.

To my friends at CINVESTAV Karen Meza, Johan Chávez, Elda Guzmán, and Raúl Agüero, I express my sincere gratitude. Your camaraderie and support have made this journey enjoyable and memorable. Thank you for the countless discus-

sions, collaborations, and shared experiences that have enriched my time here.

To my colleagues and friends at ICARUS and Fermilab—Bruce Howard, Jack Smedley, Tony Wood, Jaesung Kim, Promita Roy, Anna Heggestuen, Jacob Zettlemoyer, Ivan Caro Terrazas, Jamie Dyer, Brenda Cervantes, Diana Méndez, Iker de Icaza, Alice Campani, Maria Artero, Christian Farnese, and Jake Boza—working with such a talented and dedicated group of individuals has been a privilege. Thank you for your collaboration, support, and for making me feel welcome in the community.

To all my teachers and the secretaries (Marianita and Malu) at CINVESTAV, your guidance and assistance have been instrumental in my academic development. Thank you for your dedication and for always being there to help.

I would particularly like to thank the Consejo Nacional de Humanidades, Ciencia y Tecnología (CONAHCYT) for supporting me with the grant to pursue my doctoral studies and the CONAHCYT research grant A1-S-23238.

This thesis is a testament to the collective efforts and support of all these wonderful individuals. I am deeply grateful to each one of you.

Contents

Perspectivas para Medir Secciones Eficaces de Neutrinos en Detectores Cercanos (ICARUS y similares a DUNE-PRISM) y sus Implicaciones para Física de Precisión

por

Guadalupe Moreno Granados

Tesis de Doctorado. Departamento de Física, CINVESTAV

Resumen

La física de neutrinos está avanzando rápidamente con experimentos actuales y futuros que prometen datos de alta estadística, permitiendo una precisión sin precedentes en la medición de los parámetros del Modelo Estándar (SM) y proporcionando conocimientos cruciales sobre las interacciones neutrino-núcleo.

El experimento ICARUS, que utiliza tecnología LAr TPC, es fundamental en este crecimiento. Como el detector lejano del programa SBN en Fermilab, ICARUS está listo para investigar las anomalías de neutrinos observadas en LSND y MiniBooNE y prepararse para futuros experimentos de larga distancia como DUNE. Ubicado a lo largo del BNB y 5.75°fuera del eje del haz NuMI, ICARUS se beneficia de numerosas interacciones de neutrinos, lo que permite mediciones precisas de la sección transversal neutrino-núcleo de argón, que serán puntos de referencia para futuras mediciones de DUNE. Este trabajo presenta las perspectivas y el progreso en la medición de la sección transversal del canal inclusivo de ν_μ CC de NuMI en el experimento ICARUS.

Los datos de alta estadística también permitirán determinaciones precisas de parámetros fundamentales como el ángulo de mezcla débil y el radio de carga del neutrino (NCR), cruciales para probar el SM y explorar posibles nuevas físicas. Este trabajo incluye estudios de futuros detectores cercanos, como DUNE-PRISM, que son sensibles a las correcciones radiativas en la dispersión neutrino-electrón. La configuración de DUNE-PRISM permite el análisis de diferentes espectros de energía de neutrinos, augurando mediciones precisas del NCR con incertidumbres sistemáticas controladas.

Directores: Dr. Omar Gustavo Miranda Romagnoli, CINVESTAV y
Dra. Minerba Betancourt, Fermilab

Perspectives for Measuring Neutrino Cross-Sections at Short Baseline Detectors (ICARUS and DUNE-PRISM-like Detector) and Their Implications for Precision Physics

by

Guadalupe Moreno Granados

PhD. Thesis. CINVESTAV

Abstract

Neutrino physics is rapidly advancing with current and future experiments promising high-statistics data, enabling unprecedented accuracy in measuring Standard Model (SM) parameters and providing crucial insights into neutrino-nucleus interactions.

The ICARUS experiment, utilizing LAr TPC technology, is pivotal in this growth. As the far detector of the SBN program at Fermilab, ICARUS is set to investigate the neutrino anomalies observed in LSND and MiniBooNE and prepare for future long-baseline experiments like DUNE. Positioned along the BNB and 5.75°off-axis from the NuMI beamline, ICARUS benefits from numerous neutrino interactions, allowing for precise neutrino-argon nucleus cross-section measurements, which will benchmark future DUNE measurements. This work presents the prospects and progress in measuring the cross-section of the NuMI ν_μ CC inclusive channel in the ICARUS experiment.

High-statistics data will also enable precise determinations of fundamental parameters like the weak mixing angle and the neutrino charge radius (NCR), crucial for testing the SM and exploring potential new physics. This work includes studies of future near detectors, such as DUNE-PRISM, which are sensitive to radiative corrections in neutrino-electron scattering. The DUNE-PRISM configuration allows for the analysis of different neutrino energy spectra, promising accurate NCR measurements with controlled systematic uncertainties.

Thesis Advisors: Dr. Omar Gustavo Miranda Romagnoli, CINVESTAV

Dr. Minerba Betancourt, Fermilab

Chapter 1

Introduction

Neutrinos are among the most enigmatic and fascinating particles in the Universe: they have fundamental implications for particle physics, astrophysics, and cosmology. They could explain the matter-antimatter asymmetry in the Universe and thereby explain how there are stars and thus us in the present-day Universe, which is one of the most important open questions in physics today. Neutrinos have undoubtedly proved to be particles of extreme interest. There is evidence that their mass difference is non-zero, and they change flavor when traveling, resulting in the phenomenon called neutrino oscillation, which is the first clue of physics beyond the standard model of particle physics.

The neutrino oscillation phenomenon has been observed from different sources: the Sun, reactors, atmospheric, and accelerator beams. This phenomenon also confirms that the neutrino flavor eigenstates and the mass eigenstates are different, and they are related by a mixing matrix known as the Pontecorvo-Maki-Nakagawa-Sakata (PMNS) matrix. The neutrino oscillation probability includes the three squared mass differences Δm^2_{12}, Δm^2_{13}, and Δm^2_{23}, as well as the PMNS matrix parameters. These PMNS matrix parameters are typically expressed through three rotation matrices, which involve three mixing angles, θ_{12}, θ_{13}, and θ_{23}, and a sin-

gle complex CP-violating phase δ_{CP}. Undoubtedly, there is much needed to learn about neutrinos and their interactions. The still open questions about the nature of neutrino physics concern their absolute masses, whether they are Dirac ($\nu \neq \bar{\nu}$) or Majorana ($\nu = \bar{\nu}$) particles, whether there is leptonic CP violation, and the neutrino mass hierarchy. To answer these questions, we need a clear comprehension of neutrino interactions, including nuclear effects, which are very challenging to measure in our detectors. Experimental neutrino physics is going through a boom era due to upcoming high-precision measurements. Its development will contribute to one of the most relevant areas in recent decades, allowing the training of highly qualified human resources, both in the scientific and technical aspects and in the ability to work in a team.

The Fermi National Accelerator Laboratory (Fermilab) has a world-leading neutrino program. This program consists of two categories: the Short-Baseline Neutrino (SBN) program and the Long-Baseline Neutrino (LBN) program. The LBN program aims to search for a positive signal of the CP-violating phase in the neutrino sector, measure the neutrino mass ordering, and entirely test the three-neutrino mixing picture. These will bring clarity to us about the dominance of matter over antimatter in our present Universe. This program includes, among others, the NOvA and DUNE experiments. DUNE will be the next generation of neutrino detectors that will implement the Liquid Argon Time Projection Chamber (LAr-TPC) technology to measure the neutrino oscillation parameters at unprecedented precision using a high-intensity accelerator neutrino beam.

On the other hand, the SBN program aims to either find or rule out a fourth neutrino state called the sterile neutrino, which is a proposal to explain anomalies in short baseline neutrino experiments where the data obtained are not consistent with the expected estimate [1, 2]. The SBN program is designed to discover or definitively exclude a sterile neutrino mass region in the 1 eV scale [3] and also

verify or refute the evidence from the Neutrino-4 experiment [4] for a 7.3 eV^2, large mixing angle sterile neutrino. The SBN program consists of a near and far detector (SBND, ICARUS) that uses the LAr-TPC technology positioned along the Booster Neutrino Beamline (BNB). In addition to searching for sterile neutrinos, the SBN physics program includes searches beyond the standard model and the study of ν-Ar cross-sections with unprecedented precision with millions of interactions in the few hundred MeV to few GeV energy region, using the fluxes from two neutrino beams (BNB and NuMI), which will provide significant inputs to future measurements by DUNE, which will also use the LAr-TPC technology.

The ICARUS neutrino detector began operations in 2010 in the Gran Sasso National Laboratory in Italy in a successful 3-year physics run. Soon after that, it was moved to the CERN to be refurbished and finally was transported and installed at Fermilab in the U.S.A. to be part of the SBN program as its far detector. The principal purpose of ICARUS is to search for sterile neutrinos via the ν_e appearance [5]. The ICARUS detector is along the BNB and 5.9° off-axis from the NuMI beamline. This feature allows a large number of neutrino interactions from both beams. In particular, the NuMI beam at ICARUS provides a unique dataset before DUNE comes online, and it expects to have neutrino interactions from a few hundred MeV to several GeV (energy range expected in DUNE). This characteristic will allow ICARUS to perform measurements of the ν-Ar cross-section and beyond standard model searches in the range of a few GeV of energy.

ICARUS at Fermilab embarked on its scientific voyage by collecting data from cosmic rays and BNB and NuMI neutrino beams in March 2021, initially for commissioning purposes. On June 9, 2022, ICARUS initiated its data acquisition phase, marking the beginning of its first physics data run, lasting for one month. The data collected during this period have been instrumental in performing calibrations of both the physical components of the detector and the software used for event

reconstruction [5] and analysis.

In this work, I will present the prospects and progress to measure the cross-section of the NuMI ν_μ CC inclusive channel in the ICARUS experiment.

The thesis structure will be as follows:

In Chapter 2, the focus is on an overview of the current status of standard model neutrinos. The discussion encompasses the phenomenon of neutrino oscillation, its current status, known aspects, unresolved questions, and motivations for constructing detectors like DUNE in light of what we know and what remains unknown. Additionally, in this chapter, I will talk about the anomalies observed in short-baseline experiments that have motivated the development of theoretical models with sterile neutrino states and the main motivation for constructing of the SBN program at Fermilab.

The ICARUS detector as the far detector in the SBN program at Fermilab is introduced in Chapter 3. This experiment is dedicated to addressing anomalies in short-baseline neutrino oscillation experiments. The chapter outlines the current status of the ICARUS experiment, with a particular focus on my involvement in the collaboration spanning the commissioning phase to the present.

In Chapter 4, the focus narrows to the NuMI off-axis ν_μ CC inclusive channel, where the selection of events is presented along with perspectives on measuring the cross-section of this channel.

Looking ahead to future advancements, the potential for precision measurements of neutrino-electron scattering is explored in Chapter 5. This measurement is envisioned in the next generation of neutrino near detectors that use the Liquid Argon Time Projection Chamber technology.

Chapter 2

Neutrino Physics

After the boom in the discovery of radioactivity, Chadwick demonstrated the continuous nature of the β spectrum in 1914, distinguishing it from the single-energy α and γ rays. Ellis and Wooster later confirmed this result in 1927. Subsequently, Meitner demonstrated that the missing energy could not be attributed to neutral γ-rays, suggesting the possibility of a new particle or, as proposed by N. Bohr, that the conservation of energy might be applicable only in a statistical sense.

On December 4, 1930, W. Pauli [6, 7] proposed a solution to the issues of spin statistics and missing energy in β-disintegration. He introduced the concept of a weakly interacting neutral fermion, initially named the *neutron*. Afterward, Pauli presented his idea at the American Physical Society meeting in Pasadena in June 1931. Following J. Chadwick's 1932 discovery of the neutron [8], E. Fermi identified Pauli's particle as the *neutrino*. The first reference to the neutrino appeared in the Proceedings of the Solvay Conference in October 1933. In the same year, Fermi and Perrin [9] independently suggested that neutrinos might be massless.

In 1934, Fermi introduced the foundation for weak interactions through his β-decay theory, now known as Fermi theory. Building upon this work, Gamow and Teller [10] expanded the theory in 1936 to accommodate nuclear spin changes in

β-decays. The discovery of the muon (μ) in 1937 and subsequent observations of μ decay triggered discussions regarding the universality of Fermi interactions. This concept, later termed generation or family, emerged from debates involving Puppi, Klein, Tiomno, Wheeler, Lee, Rosenbluth, and Yang [11].

Despite the success of Fermi's theory, the neutrino remained elusive. Bethe and Peierls predicted challenging interactions in 1934. In the early 1950s, Pontecorvo [12] motivated Reines and Cowan [13] to devise a method for detecting inverse β-decay process, where an antineutrino generates a positron. Their 1956 experiment, utilizing a large flux of antineutrinos from a nuclear reactor, marked the inaugural reactor-neutrino experiment era and confirmed the existence of neutrinos. For this research, Reines was awarded the Nobel Prize 40 years later.

In this chapter, we briefly review the history of neutrinos, focusing specifically on the phenomenon of neutrino oscillation, its current status, known aspects, open questions, and motivations for building a new generation of detectors, such as DUNE.

2.1 Neutrinos in the Standard Model

The Standard Model (SM) is based on the symmetry group $SU(3)_C \otimes SU(2)_L \otimes U(1)_Y$. The group $SU(3)_C$ corresponds to the symmetry group of quantum chromodynamics (QCD), where the subscript C refers to color. On the other hand, the group $SU(2)_L \otimes U(1)_Y$ is the symmetry group of electroweak theory (EW), where the subscript L represents the left chirality of the particles involved, and the subscript Y refers to hypercharge. The SM was developed between the 1960s and 1970s by several scientists, including Sheldon Glashow [14], Steven Weinberg [15], and Abdus Salam [16], who laid the foundations for electroweak theory.

The SM consists of 4 electroweak gauge bosons and 8 gluons, corresponding to the 12 generators of the gauge group. The gauge bosons of the SM are vector bosons that mediate the electromagnetic, weak, and strong interactions. The mediator boson

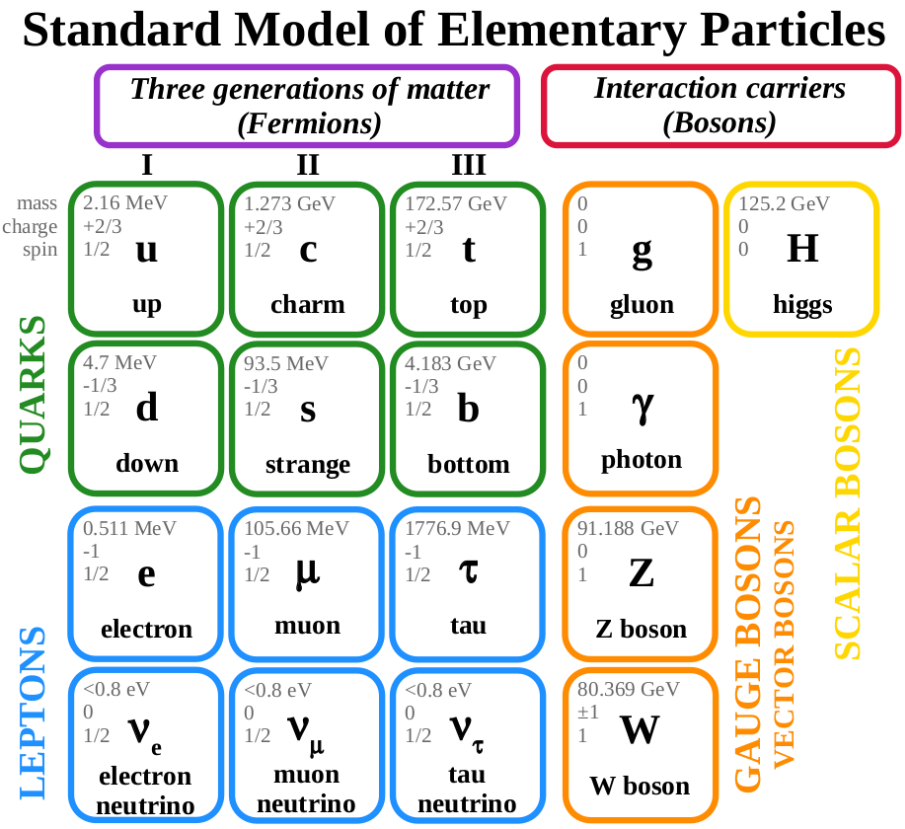

Figure 2.1: Fundamental particles of matter and interaction carriers in the Standard Model.

of the electromagnetic interaction is the photon (γ), while the weak interaction is mediated by three bosons: the Z and $W^{\pm}$ bosons. The strong interaction is mediated by eight gluons (g). Additionally, there is a scalar boson, the Higgs boson (ϕ), which not only provides mass to the 12 fundamental fermions [1] (to be mentioned below) but is also associated with the Higgs mechanism. This mechanism is essentially the

[1]It is not clear if the SM Higgs field gives mass to neutrinos, as this would require the existence of right-handed neutrinos (and left-handed antineutrinos), which we do not know if they do. The Higgs field allows certain right-chiral and left-chiral fermions to interact, giving them mass when the Higgs field's vacuum state is non-trivial. However, in the SM, neutrino masses are predicted to be zero because there are no right-chiral neutrino fields for left-chiral neutrinos to pair with. Therefore, for neutrinos to have mass, new fields and particles beyond the SM are needed [17].

process by which the Z and $W^{\pm}$ gauge bosons acquire mass.

In the SM, 12 fermions constitute the fundamental building blocks of matter, see Fig. 2.1. These fermions possess half-integer ($\frac{1}{2}$) spin and, so far, have not been observed to be composed of other particles. They are divided into two groups: leptons and quarks. There are six leptons, comprising 3 charged leptons—the electron (e), the muon (μ), and the tau (τ) −as well as 3 neutral leptons: the electron neutrino (ν_e), the muon neutrino (ν_μ), and the tau neutrino (ν_τ). Similarly, there are six flavors of quarks, classified according to their electric charge: those with a charge of $+\frac{2}{3}$ −the up (u), charm (c), and top (t) quarks −and those with a charge of $-\frac{1}{3}$ −the down (d), strange (s), and bottom (b) quarks.

The 12 fundamental fermions can be further grouped into families. So far, only 3 families have been observed, with the primary difference being the mass of the particles that compose them. The first family is the lightest, followed by the second family, which is lighter than the third family.

The particles of the SM interact through the electromagnetic, weak, and strong fundamental forces [2]. Depending on the interactions that the fundamental fermions experience, they will have different properties. All 12 particles are sensitive to the weak interaction. Except for electrically neutral neutrinos, the other 9 particles are electrically charged and thus sensitive to the electromagnetic interaction of Quantum Electrodynamics (QED). Moreover, the 6 quarks of the SM have color charge, making them the only particles sensitive to the strong interaction of Quantum Chromodynamics (QCD). A characteristic of these particles is that, so far, they have not been found in a free state; they are confined in bound states called hadrons, which can be formed by 3 quarks (baryons, such as the proton (p) or the neutron (n)) or in a quark-antiquark state (mesons, such as pions (π) or kaons (K)).

[2] Also interact through the gravitational force.

2.1.1 Electroweak Interactions

As mentioned earlier, neutrinos are neutral particles that interact through the weak interaction, mediated by the $W^{\pm}$ and Z bosons of the Standard Model, and through gravity. In the 1960s, S. Glashow, S. Weinberg, and A. Salam developed a model to unify the electromagnetic and weak forces, which is known as the electroweak theory. This unification is described by the gauge group $SU(2)_L \otimes U(1)_Y$.

Experiments conducted by Chien-Shiung Wu [18] and Maurice Goldhaber [19] had already demonstrated the left-handed nature of neutrinos, showing that the weak interactions involving charged currents couple exclusively to specific chiral states. The $SU(2)_L$ group naturally accommodates this property, as only the left-handed fermion fields (and the right-handed anti-fermion fields) have a non-trivial representation in the group.

In this framework, the left-handed fermion states are arranged in doublets,

$$L_e = \begin{pmatrix} \nu_e \\ e^- \end{pmatrix}_L , \qquad L_\mu = \begin{pmatrix} \nu_\mu \\ \mu^- \end{pmatrix}_L , \qquad L_\tau = \begin{pmatrix} \nu_\tau \\ \tau^- \end{pmatrix}_L , \tag{2.1}$$

while the right-handed states do not couple to the $W^{\pm}$ bosons and are represented as $SU(2)$ singlets

$$l_e = e_R \, , \qquad l_\mu = \mu_R \, , \qquad l_\tau = \tau_R \, . \tag{2.2}$$

In the Standard Model, the local gauge symmetry $SU(2)_L$ is associated with three gauge bosons, W^i_μ. The physical $W^{\pm}$ bosons, which are associated with charged weak currents, are identified as the following linear combination:

$$W^{\pm}_\mu = \frac{1}{\sqrt{2}} \left(W^1_\mu \mp i W^2_\mu \right) , \tag{2.3}$$

where W^+ corresponds to the positively charged current and W^- to the negatively charged current.

In the electroweak unification model, the neutral gauge field W_μ^3 of $SU(2)_L$ mixes with the $U(1)_Y$ gauge symmetry field B_μ. This mixing gives rise to the physical fields of the photon (A_μ) and the Z_μ boson associated with the neutral weak current [20]. The mixing of the fields W_μ^3 and B_μ occurs through the combinations:

$$A_\mu = B_\mu \cos\theta_W + W_\mu^3 \sin\theta_W \tag{2.4a}$$

$$Z_\mu = -B_\mu \sin\theta_W + W_\mu^3 \cos\theta_W, \tag{2.4b}$$

where θ_W is the weak mixing angle, also known as the Weinberg angle.

This electroweak unification implies that the coupling constants of the weak (g') and electromagnetic (g) interactions are related through:

$$e = g \sin\theta_W = g' \cos\theta_W. \tag{2.5}$$

Moreover, the weak mixing angle $\sin\theta_W$ has been measured in various ways, including the study of $e^+e^- \to Z \to f\bar{f}$. The average of these measurements [21] is:

$$\sin^2\theta_W = 0.23146 \pm 0.00012. \tag{2.6}$$

2.2 Neutrino Oscillations Theory

In 1957, Pontecorvo introduced the concept of neutrino oscillations [12,22], drawing inspiration from the oscillations observed in $K^0 - \bar{K}^0$ systems. Building upon this idea, Maki, Nakagawa, and Sakata [23] proposed a model in 1967 wherein ν_e and ν_μ are composed of two eigenstates of mass. In the same year, Pontecorvo predicted the solar neutrino problem as a consequence of the $\nu_e \to \nu_\mu$ mixing. All the mechanisms studied by Pontecorvo considered only vacuum oscillations. Afterward, the Homestake experiment [24] measured the neutrino flux coming from the Sun, showing a

deficit compared to the fluxes predicted by the solar models, initiating the so-called solar neutrino problem.

The neutrino oscillation mechanism is a quantum mechanical phenomenon that entails the non-conservation of lepton flavor during neutrino propagation [11]. The discovery of neutrino oscillations implies that neutrino flavor states are not mass eigenstates but rather a superposition of these states. A spectrum of mass eigenstates $|\nu_k\rangle$ can contribute with $k = 1, 2, ..., N$, where n, in general, can be larger than three. A well-defined neutrino flavor state, $|\nu_\alpha\rangle$ with $\alpha = e, \mu, \tau$, can be described in terms of the $|\nu_k\rangle$ mass eigenstates as,

$$|\nu_\alpha\rangle = \sum_{k=1}^{N} U^*_{\alpha k} |\nu_k\rangle \,, \tag{2.7}$$

where U is a unitary $N \times N$ matrix. This unitary matrix is the leptonic mixing matrix (analogous to the CKM quark mixing matrix [21]), also referred to as the PMNS matrix [21], named after Pontecorvo, Maki, Nakagawa, and Sakata. A typical lepton mixing matrix assumes that $k = 1, 2, 3$ and $\alpha = e, \mu, \tau$ and takes the form

$$U = \begin{pmatrix} U_{e1} & U_{e2} & U_{e3} \\ U_{\mu 1} & U_{\mu 2} & U_{\mu 3} \\ U_{\tau 1} & U_{\tau 2} & U_{\tau 3} \end{pmatrix} . \tag{2.8}$$

Since U is unitary, it satisfies the relation $UU^\dagger = U^\dagger U = I$, with I the identity matrix. Therefore, by inverting Eq. (2.7), we can describe the mass eigenstates in terms of flavor eigenstates as

$$|\nu_k\rangle = \sum_{\alpha} U_{\alpha k} |\nu_\alpha\rangle \,. \tag{2.9}$$

Now, consider that at a time t=0, a neutrino is created in a pure state $|\nu_k(0,0)\rangle$. As it propagates, it evolves as follows:

$$|\nu_k(\bar{x}, t)\rangle = e^{-i\phi(t)} |\nu_k(0,0)\rangle \,, \tag{2.10}$$

where $e^{-i\phi(t)}$ represents the time evolution state. Taking $\phi(t) = P_\mu X^\mu = Et - \bar{P}\cdot\bar{x}$, it will be obtained,

$$|\nu_k(\bar{x},t)\rangle = e^{-i(E_k t - \bar{P}_k\cdot\bar{x})}|\nu_k(0,0)\rangle = \exp\left(-i\frac{m_k^2 L}{2E}\right)|\nu_k(0,0)\rangle\,, \tag{2.11}$$

where $E \equiv E_k = E(\nu_k) = \sqrt{|P_k|^2+m_k^2}$ is the energy of the neutrino ν_k. It has also been considered that in the ultrarelativistic limit $|\bar{P}_k| >> m_k$. In addition, we assume that the origin is at $x = 0$. We consider that neutrinos travel at the velocity $c = 1$, which implies $x = t = L$, where L is the distance traveled by the ν_k. We also consider that the total energy of the neutrino is $E \approx |\bar{P}_k|$. The calculation details for Eq (2.11) are shown in Appendix A.

The transition amplitude for detecting a β-flavor neutrino (ν_β) at a point in space-time $(\bar{x},t)$, given that an α-flavor neutrino (ν_α) was generated at the origin, will be:

$$A\left(\left[\nu_\alpha(0,0)\to\nu_\beta(\bar{x},t)\right]\right) = \sum_k \exp\left(i\frac{m_k^2 L}{2E}\right)U_{\beta k}U_{\alpha k}^*\,, \tag{2.12}$$

then, the probability of oscillation will be the coherent sum of $P(\nu_\alpha \to \nu_\beta) = |A\left(\left[\nu_\alpha(0,0)\to\nu_\beta(\bar{x},t)\right]\right)|^2$, that is

$$\begin{aligned} P(\nu_\alpha\to\nu_\beta)(L,E) = \delta_{\alpha\beta} &- 4\sum_{k>j}\Re e\left[U_{\alpha k}^* U_{\beta k}U_{\alpha j}U_{\beta j}^*\right]\sin^2\left(\frac{\Delta m_{kj}^2 L}{4E}\right) \\ &+ 2\sum_{k>j}\Im m\left[U_{\alpha k}^* U_{\beta k}U_{\alpha j}U_{\beta j}^*\right]\sin\left(\frac{\Delta m_{kj}^2 L}{2E}\right)\,. \end{aligned} \tag{2.13}$$

This result assumes that a flavor eigenstate ν_α produced by a neutrino source propagates as a superposition of eigenstates of mass ν_k along a distance L toward a detector, where the flavor eigenstate ν_β is measured. For the oscillation effects to be observed, the phase of the sinusoidal functions must be of order 1.

$$\frac{\Delta m_{kj}^2 L}{E} \sim 1, \tag{2.14}$$

where $\Delta m^2_{kj} \equiv m^2_k - m^2_j$ represents the difference in squared masses. It should be emphasized that observations of the neutrino oscillation phenomenon imply that at least two neutrino species have non-zero mass.

Considering that the value of Δm^2 is determined by nature, various experiments can be designed to be sensitive to different values of Δm^2 by selecting appropriate values of the L/E ratio. In this manner, different types of neutrino oscillation experiments can be categorized based on the average value of the L/E ratio.

Short-baseline experiments ($L/E \lesssim 1\,\mathrm{km/GeV}$) are sensitive to $\Delta m^2 \gtrsim 1\,\mathrm{eV}^2$. Examples of experiments of this type include CHARM [25], NOMAD [26], LSND [1], MiniBooNE [27], and the ongoing SBN program [3].

On the other hand, long-baseline experiments ($L/E \lesssim 10^3\,\mathrm{km/GeV}$) are sensitive to $\Delta m^2 \gtrsim 10^{-3}\,\mathrm{eV}^2$. Some examples of experiments in this category include T2K [28], MINOS [29], Super-Kamiokande [30, 31], NOνA [32], and the upcoming Hyper-Kamiokande [33] and DUNE [34, 35] experiments.

2.2.1 Neutrino Oscillations Experiments

Neutrino oscillation experiments began with the pioneering work of John N. Bahcall [36, 37], computing the expected solar neutrino flux, and Raymond Davis Jr., who initiated the Homestake experiment [24] in the 1960s to detect solar neutrinos. Subsequent experiments involving reactor, atmospheric, solar, and accelerator-based studies revolutionized our comprehension of neutrinos. Due to its relevance, we summarize the main characteristics of these experiments.

Solar Neutrino Experiments: Detect neutrinos originating from the Sun's core through thermonuclear reactions that power its radiant energy. Investigations, such as the Sudbury Neutrino Observatory (SNO) [38], have significantly advanced our understanding of solar neutrinos and their oscillations, solving the solar neutrino problem and confirming neutrino flavor transitions. These ex-

periments exhibit exceptional sensitivity to very small values of Δm^2_{21}. This heightened sensitivity, surpassing that of other experiments, underscores the unique contribution of solar neutrino experiments in revealing the fundamental properties of neutrinos and their role in the Sun's energy production processes.

Atmospheric Neutrino Experiments: Investigate neutrinos produced by cosmic ray interactions in the Earth's atmosphere. Primary cosmic ray interactions produce pions and kaons, producing muons and muon neutrinos through their subsequent decay. Subsequent decays may result in electrons and muon neutrinos before reaching the Earth's surface. These experiments, designed to detect neutrinos, operate within a broad energy range, typically from 500 MeV to 100 GeV, and even higher in larger detectors such as IceCube [39]. The Super-Kamiokande [30] experiment in Japan, among others, has provided essential insights into neutrino oscillations by observing the distortion of the expected neutrino flux ratios. Atmospheric neutrino experiments have been instrumental in confirming the oscillation of muon neutrinos and electron neutrinos.

Reactor Neutrino Experiments: Play a key role in the study of neutrino oscillations, utilizing nuclear reactors as potent sources of antineutrinos produced by the β decays of heavy nuclei, primarily fission fragments of ^{235}U, ^{238}U, ^{239}Pu, and ^{241}Pu. The energy range of reactor $\bar{\nu_e}$'s typically falls within a few MeV. The initial experimental confirmation of neutrino oscillations emerged from reactor experiments, exemplified by the KamLAND experiment [40,41] in Japan. Reactor experiments exhibit a particular sensitivity to the phenomenon of electron antineutrino disappearance.

Accelerator Neutrino Experiments: Involve the study of high-energy neutrinos generated by particle accelerators. These experiments utilize beams of ν_μ,

generated through the decay of pions, kaons, and muons resulting from the impact of a proton beam on a target. Such experiments include MINOS (Main Injector Neutrino Oscillation Search) [29], NOνA [32], and T2K (Tokai to Kamioka) [28]. They are further categorized as appearance experiments when focusing on the observation of ν_e oscillating from the initial ν_μ or disappearance experiments when examining the reduction in ν_μ events due to oscillations. One distinctive feature of accelerator experiments is their ability to provide controlled beams of neutrinos, which allow precise measurements of oscillation parameters. The subsequent sections will delve into a detailed discussion of these experiments as they constitute the primary focus of this thesis.

The neutrino oscillation experiments have revolutionized our understanding of neutrino properties. Reactor, atmospheric, solar, and accelerator experiments collectively contribute to a complete picture of neutrino oscillations.

2.2.2 The Solar and Atmospheric neutrino problems

The solar neutrino flux problem was one of the first major discrepancies that challenged the SM. The Sun, through nuclear fusion, primarily produces electron neutrinos (ν_e). The Standard Solar Model (SSM) predicted a certain number of these neutrinos, but the Homestake experiment detected only about one-third of the expected flux [42]. Subsequent experiments like GALLEX [43], SAGE [44], and Kamiokande [45] confirmed this deficit.

This discrepancy, known as the solar neutrino problem, was resolved by the theory of neutrino oscillations. This theory was confirmed by the Sudbury Neutrino Observatory (SNO) [46] in Canada, which used heavy water (D_2O) to detect all types of neutrinos and found the total number of neutrinos from the Sun matched predictions when all flavors were considered.

The atmospheric neutrino flux problem deals with the observed discrepancies in

neutrinos produced by cosmic rays interacting with the Earth's atmosphere. High-energy cosmic rays produce showers of secondary particles, including muon neutrinos (ν_μ) and electron neutrinos (ν_e), with an expected ratio of approximately 2:1. However, experiments such as Super-Kamiokande [30] found a deficit in ν_μ, especially for those that traveled long distances. This indicated that ν_μ were oscillating into tau neutrinos (ν_τ), providing strong evidence for neutrino oscillations.

The resolution of both the solar and atmospheric neutrino problems through the discovery of neutrino oscillations had important implications. Neutrinos must have mass to oscillate between flavors, contrary to the original Standard Model assumption that neutrinos are massless. This discovery necessitated extensions to the Standard Model to incorporate neutrino masses and mixing. Understanding neutrino properties is crucial for models of stellar processes, supernova dynamics, and the evolution of the early universe.

In 2015, Takaaki Kajita [47] and Arthur B. McDonald [48] were awarded the Nobel Prize for their experimental work that confirmed the neutrino oscillation mechanism in the Super-Kamiokande and SNO experiments, respectively.

The neutrino oscillation from the "active" flavors neutrinos explains the Solar and Atmospheric neutrino fluxes problem. We need the mixing of at least 3 neutrino states to fully describe current experimental results.

2.3 Neutrino Anomalies

Despite the success of the SM in explaining many experimental observations with the three known neutrino flavors, several anomalies have been observed in short-baseline neutrino experiments that suggest the possible existence of a fourth, sterile neutrino. These anomalies are described below [49]:

LSND Anomaly. The Liquid Scintillator Neutrino Detector (LSND) experiment

[1] at Los Alamos National Laboratory used a decay-at-rest pion beam to produce muon antineutrinos in the energy range of 20-53 MeV. These neutrinos were detected about 30 meters from the source using a liquid scintillator-based detector via inverse beta decay (IBD) on carbon, $\bar{\nu}_e p \to e^+ n$. Over five years, LSND observed $89.7 \pm 22.4 \pm 6.0$ $\bar{\nu}_e$ candidate events above the expected background, corresponding to a 3.8 σ excess. This result, indicative of $\bar{\nu}_\mu \to \bar{\nu}_e$ oscillations with a mass-squared difference (Δm^2) in the 1 eV^2 region, suggests new physics beyond the three Standard Model neutrinos.

MiniBooNE Anomaly. The MiniBooNE experiment [27, 50, 51] at Fermilab measured neutrino interactions 540 m from the target of the Booster Neutrino Beam (BNB), producing a predominantly ν_μ beam peaking at 700 MeV. Neutrinos were identified through characteristic Cherenkov rings formed by muons and electrons in charged-current interactions. Over ten years of data collection, MiniBooNE [52] observed a 3.4 σ excess of ν_e candidates in neutrino mode (162.0 ± 47.8 events) and a 2.8 σ excess of $\bar{\nu}_e$ candidates in antineutrino mode (78.4 ± 28.5 events). The observed excesses are consistent with the LSND results, further suggesting the presence of sterile neutrino oscillations at short baselines. The excess events could be electrons or single photons, indistinguishable in MiniBooNE's Cherenkov detector. This ambiguity is being addressed by the MicroBooNE [53] experiment, which can differentiate between electrons and photons.

Reactor Neutrino Anomaly. The reactor neutrino anomaly [54] refers to the deficit of electron antineutrinos ($\bar{\nu}_e$) observed in numerous detectors located a few meters from nuclear reactors, compared to predicted rates [55–57]. The average ratio of observed to predicted events is $R_{avg} = N_{obs}/N_{pred} = 0.927 \pm 0.023$. This deficit was initially highlighted by reevaluations of inverse beta decay cross-sections and accounted for long-lived radioisotopes in

reactors. Recent updates slightly adjusted the predictions, yielding $R_{avg} = 0.936 \pm 0.005\,(\text{exp.}) \pm 0.023\ (\text{model})$ [58], representing a 2.6 σ deviation from unity. Additionally, uncertainties in reactor neutrino fluxes, including forbidden transitions, may contribute to systematic errors of a few percent. These discrepancies point towards potential sterile neutrino oscillations with $\Delta\text{m}^2 \sim 1\,\text{eV}^2$.

Gallium Anomaly. The SAGE [44] and GALLEX [43] solar neutrino experiments observed an overall deficit in the number of electron neutrino (ν_e) events from intense radioactive sources during calibration runs. The combined ratio of detected to predicted neutrino events is $R = 0.86 \pm 0.05$, corresponding to a 2.7 σ deficit. This anomaly, observed over very short baselines, suggests ν_e disappearance potentially due to oscillations with $\Delta\text{m}^2 \geq 1\,\text{eV}^2$.

These anomalies collectively indicate potential new physics beyond the Standard Model, particularly the existence of a sterile neutrino that mixes with the three known neutrino flavors. They underscore the need for further experimental and theoretical investigations to resolve these discrepancies and improve our understanding of the properties of neutrinos.

2.3.1 The (3+1) Neutrino Oscillations Scenario

One of the simplest and potentially viable solutions to address the short-baseline neutrino anomalies is the 3+1 neutrino oscillation scenario. This scenario proposes the existence of an additional sterile neutrino beyond the three active neutrino flavors (ν_e, ν_μ, and ν_τ) described by the Standard Model. Sterile neutrinos do not interact via the weak force and therefore cannot be directly detected through standard weak interaction processes.

In the 3+1 scenario, alongside the standard three active neutrino flavors, a fourth neutrino mass state, denoted as ν_s, is introduced. This sterile neutrino mixes with

the active neutrino flavors, leading to oscillations between active and sterile neutrinos. For a 3+1 mixing matrix,

$$\begin{pmatrix} \nu_e \\ \nu_\mu \\ \nu_\tau \\ \nu_s \end{pmatrix} = \begin{pmatrix} U_{e1} & U_{e2} & U_{e3} & U_{e4} \\ U_{\mu 1} & U_{\mu 2} & U_{\mu 3} & U_{\mu 4} \\ U_{\tau 1} & U_{\tau 2} & U_{\tau 3} & U_{\tau 4} \\ U_{s1} & U_{s2} & U_{s3} & U_{s4} \end{pmatrix} \begin{pmatrix} \nu_1 \\ \nu_2 \\ \nu_3 \\ \nu_4 \end{pmatrix} . \tag{2.15}$$

As long as Δm^2_{41} is much greater than both $|\Delta m^2_{31}|$ and Δm^2_{21}, oscillations in short-baseline experiments can be effectively described by a two-flavor vacuum oscillation formula [3],

$$P_{\alpha\beta} = \delta_{\alpha\beta} - 4|U_{\alpha\beta}|^2(\delta_{\alpha\beta} - |U_{\alpha\beta}|^2)\sin^2\left(\frac{\Delta m^2_{41} L}{4E}\right) . \tag{2.16}$$

Each oscillation channel ν_α to ν_β is governed by a distinct effective mixing angle $\theta_{\alpha\beta}$ as follows:

$$\nu_\mu \to \nu_e : \quad \sin^2 2\theta_{\mu e} \equiv 4|U_{\mu 4}|^2|U_{e4}|^2 \tag{2.17a}$$

$$\nu_e \to \nu_e : \quad \sin^2 2\theta_{ee} \equiv 4|U_{e4}|^2(1 - |U_{e4}|^2) \tag{2.17b}$$

$$\nu_\mu \to \nu_\mu : \quad \sin^2 2\theta_{\mu\mu} \equiv 4|U_{\mu 4}|^2(1 - |U_{\mu 4}|^2) . \tag{2.17c}$$

Sterile neutrino oscillations exhibit two key features. Firstly, their characteristic $\sin^2(\Delta m^2 L/4E)$ dependence can distinguish them from other potential explanations for anomalies. Secondly, short-baseline transitions $\nu_\mu \to \nu_e$ require non-zero U_{e4} and $U_{\mu 4}$, leading to probabilities of $\nu_\mu \to \nu_\mu$ and $\nu_e \to \nu_e$ that are less than one. This parameter dependence allows for stringent testing of the sterile neutrino hypothesis.

As mentioned, a possible explanation for the observed anomalies involves oscillations that include a light sterile neutrino; however, this explanation is disfavored by

other experimental findings [3]. One particularly interesting hypothesis posits a heavy decaying sterile neutrino (HDSN), as proposed in Refs. [61] and [62]. This scenario suggests the existence of a fourth neutrino mass eigenstate, ν_4, with a mass (m_4) ranging between 10 keV and 1 MeV. Importantly, ν_4 mixes with the muon flavor and decays into an electron neutrino and an undetectable light scalar field ϕ. This decay mechanism serves to replicate the excesses observed in both the LSND and MiniBooNE experiments. This model is currently being studied for application in a DUNE-PRISM-like experiment. It is a work in progress, and results are expected soon.

2.4 Cross-Sections of Neutrino Interactions

Neutrino cross-sections serve as fundamental quantities in understanding neutrino interactions with matter. These interactions occur through the exchange of $W^{\pm}$ bosons in charge current (CC) interactions or a Z boson in neutral current (NC) interactions with the target particle. The target particle with which the neutrino interacts can vary. Neutrinos primarily interact with nucleons within atomic nuclei or with electrons in the medium. The choice of target particle affects the cross-section due to differences in mass, charge, and interaction mechanisms, as we will see in the next chapters.

The interaction cross-section of neutrinos with nuclei via the charged current and neutral current channels can be classified into three main categories: quasi-elastic

[3]There is significant tension between the results of appearance and disappearance neutrino oscillation experiments. Additionally, cosmological limits place stringent constraints on the number of additional neutrino species that were relativistic in the early Universe [59]. Despite this, direct searches for a fourth neutrino are worth pursuing, as they could lead to a new paradigm in the structure of the Standard Model and its interactions. Some proposals link these anomalies to potential connections with the Dark Sector [60] in particle physics.

scattering, resonance production, and deep inelastic scattering. In addition, another important interaction is due to meson exchange currents. A brief description of each is given below.

Quasi-elastic scattering (QE): refers to the interaction between a neutrino and a nucleon (either a proton or a neutron) within a nucleus, resulting in the generation of a lepton [electron (e), muon (μ), or tau (τ)] and a recoiling nucleon as the final state of the interaction. The term "quasi-elastic" denotes its resemblance to the idealized elastic scattering process between a neutrino and an individual nucleon, although it occurs within the complex environment of the nucleus.

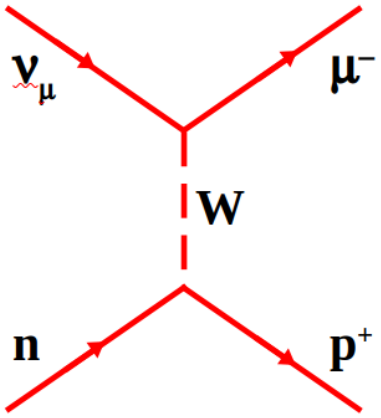

Figure 2.2: Example of charged current quasi-elastic (QE) scattering, in which a muon neutrino (ν_μ) interacts with a neutron (n) within the nucleus, exchanging a W boson, resulting in a muon (μ) and proton (p) final state.

This interaction mechanism is characterized by the conservation of energy and momentum, adhering to fundamental principles of particle physics. This process is a dominant mode in neutrino oscillation experiments due to its relatively straightforward nature and clear signature in neutrino detectors, especially at lower neutrino energies typical of accelerator-based experiments.

The quasi-elastic process plays a pivotal role in studying neutrino properties and researching neutrino oscillation phenomena owing to its clear experimental manifestations and well-understood kinematic properties.

Resonance Production (RES): involves the interaction of an incoming neutrino with a nucleon within the nucleus, leading to the excitation of the nucleon to a higher-energy state, referred to as a resonance process. This excited state subsequently undergoes decay, emitting a variety of particles, including pions, nucleons, and photons. Resonance production significantly contributes to the neutrino-nucleus cross-section, particularly in the intermediate energy regime.

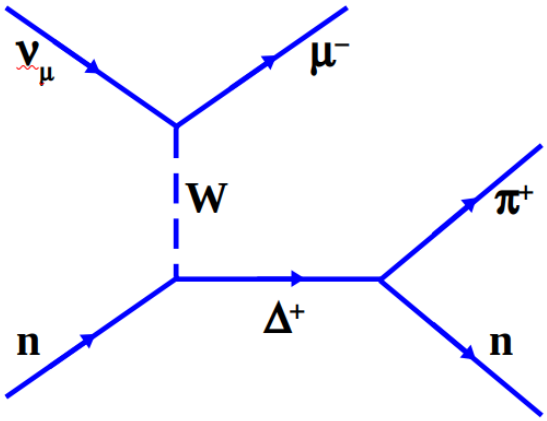

Figure 2.3: Example of charged current resonance production (RES), in which a muon neutrino (ν_μ) interacts with a neutron (n) within the nucleus, exchanging a W boson. This interaction results in a final state where the leptonic channel produces a muon (μ). In contrast, in the hadronic channel, a delta (Δ) resonant state decays into a pion (π) and a neutron (n).

Deep Inelastic Scattering (DIS): involves the interaction of high-energy neutrinos with individual quarks within nucleons. This complex process serves as a probe into the intricate internal structure of both nucleons and nuclei, thereby yielding valuable insights into parton distribution functions and quark-gluon

dynamics. DIS phenomena are particularly prevalent at high neutrino energies, providing sufficient energy for the break up of the nucleon.

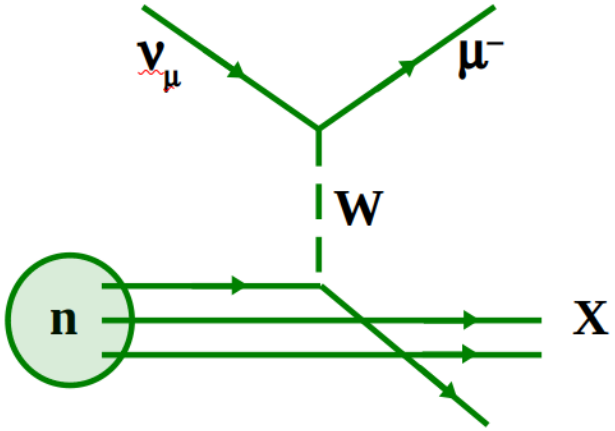

Figure 2.4: An example of charged current deep inelastic scattering (DIS), in which a muon neutrino (ν_μ) interacts with the quarks within a neutron (n), exchanging a W boson. This interaction results in a final state where the leptonic channel produces a muon (μ). In contrast, in the hadronic channel, different processes can occur, leading to the production of different particles (X) depending on the available energy in the phase space.

Meson exchange currents (MEC): involve the exchange of virtual mesons, such as pions, between nucleons (neutrons, protons) within the nucleus during neutrino interactions. This process plays a vital role in neutrino-nucleus scattering phenomena and contributes significantly to the cross-section of neutrino interactions with nuclei. This interaction occurs when a neutrino interacts with a nucleus through charged or neutral current interactions, leading to the excitation of nucleons within the nucleus. This excitation involves the correlated excitation of multiple nucleons within the nucleus, typically two nucleons (referred to as 2p-2h). The correlated excitation of nucleons allows for the exchange of virtual mesons between them. These mesons, often pions, mediate

the strong nuclear force interaction between the nucleons. The exchange of mesons contributes to the dynamics of the neutrino-nucleus interaction and affects the final state particles produced in the process. After the meson exchange process, the nucleus may transition to a different state, and various particles may be emitted or produced due to the interaction.

The neutrino cross-sections depend on the energy of the incident neutrino. At lower energies, coherent scattering prevails as the dominant interaction mechanism, while at higher energies, deep inelastic scattering becomes prominent. The energy dependence of cross-sections reflects the energy availability for particle production and the kinematics of the interaction processes. Fig. 2.5 shows various neutrino scattering mechanisms mentioned above.

The measurement and analysis of neutrino cross-sections play a vital role in diverse research areas, including neutrino oscillation experiments, astrophysics, and searches for new physics beyond the Standard Model.

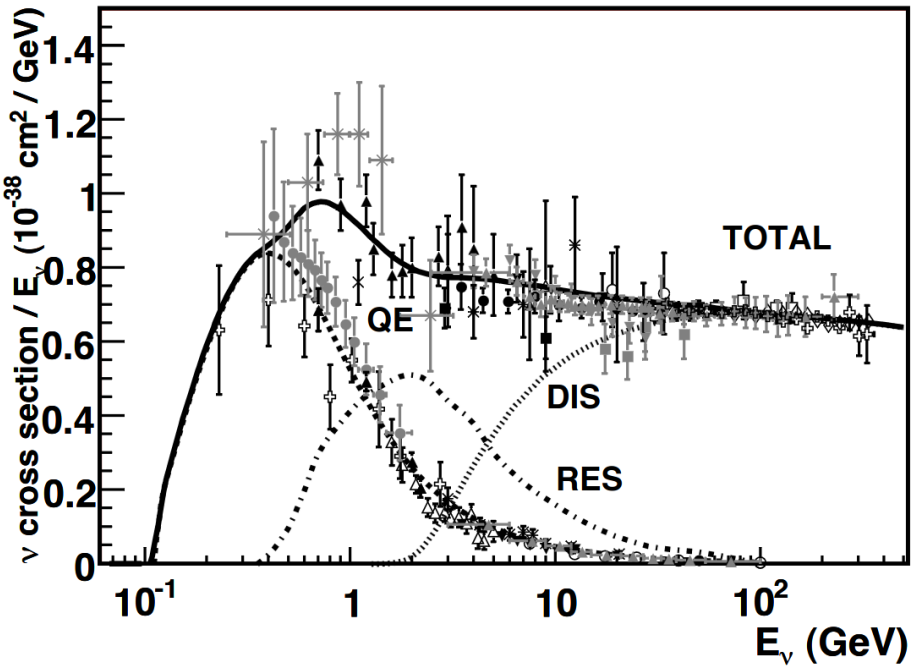

Figure 2.5: Total neutrino per nucleon CC cross-sections for an isoscalar target, normalized by neutrino energy and plotted against energy. The data points represent results from various experiments as described in [63]. Different processes are illustrated: QE scattering (dotted), resonance production (dot-dash), and DIS scattering (dashed). Taken from [63].

Chapter 3

ICARUS as the Far Detector of the SBN Program at Fermilab

Currently, several experiments are underway to discover or exclude the neutrino anomalies identified by the Liquid Scintillator Neutrino Detector (LSND) [1] and MiniBooNE [27, 52] short-baseline accelerator experiments. At Fermi National Laboratory in Illinois, USA (Fermilab), a dedicated Short-Baseline Neutrino (SBN) Program has been established with the primary aim of discovering or definitively excluding a region of sterile neutrino mass at the 1 eV scale [3]. Additionally, the SBN program will seek to verify or refute the observations posited by the Neutrino-4 experiment [4] regarding a 7.3 eV^2 large mixing angle sterile neutrino.

This chapter will be dedicated to discussing the ICARUS-T600 detector role within the SBN program at Fermilab, describing its technical specifications, current status, and its capacity to measure the neutrino-nucleus cross-section, particularly concerning neutrinos originating from the Main Injector (NuMI) beam. The neutrino energy spectrum expected by the NuMI beam at ICARUS is of the order of a few hundred MeV to multi-GeV [64], providing a unique dataset to offer valuable insights into neutrino interactions within a comparable energy range expected by DUNE [35].

The results of neutrino interactions from NuMI in ICARUS will be a benchmark for a future DUNE experiment.

3.1 The SBN Program

The Short-Baseline Neutrino (SBN) Program [3, 49] at Fermilab represents a multifaceted scientific effort dedicated to studying the properties of neutrinos, with a particular focus on addressing the possible existence of sterile neutrinos at the eV scale and exploring potential extensions of the Standard Model. Even if they exist, we cannot directly observe the sterile neutrino states since they will not interact with ordinary matter through weak interaction. However, the mixing between an active and a sterile state could generate new oscillations among the standard neutrino flavors. The search for light sterile neutrinos in SBN is motivated by a set of anomalous results in previous neutrino data, particularly from the LSND and MiniBooNE experiments.

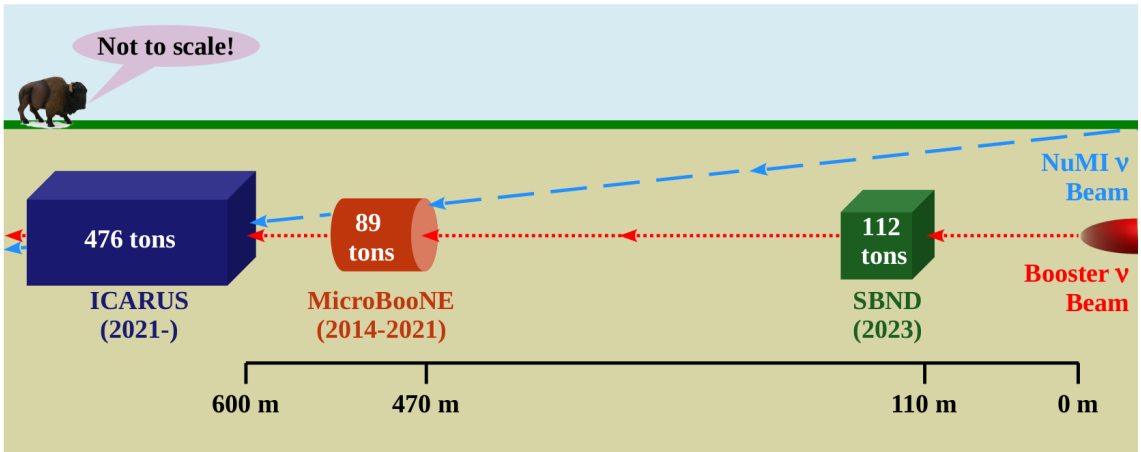

Figure 3.1: Diagram illustrating the positions of the detectors comprising the SBN program at Fermilab along the Booster neutrino beam, including the case of ICARUS, located on-axis along the Booster beam and approximately 6° off-axis from the NuMI beam.

The scientific potential of the SBN program transcends its primary goal of oscillation searches. High-precision detectors within the program capture millions of neutrino interactions with argon, facilitating an extensive research agenda in neutrino-argon scattering. This research carries significant implications for the use of liquid argon detectors in upcoming neutrino experiments, particularly the DUNE experiment. Furthermore, the SBN program has garnered substantial interest in studying New Physics beyond the Standard Model, including searches for light-dark matter, decaying sterile neutrinos, millicharged particles, and more.

The SBN program comprises three detectors utilizing liquid argon time projection chamber technology (LAr-TPC) [65]. Positioned along the Booster Neutrino Beamline (BNB) at varying distances from the target, as illustrated in Fig. 3.1, this configuration is pivotal for achieving the world-leading sensitivity of the experiment. The Short-Baseline Neutrino Detector, SBND [3,66], situated 110 m from the target, houses a 112-ton active-mass LAr-TPC. It aims to provide precise measurements of pre-oscillation neutrino interactions, thereby mitigating systematic uncertainties in the quest for downstream oscillation signals. The commissioning of this detector started at the end of 2023. Positioned 470 m from the target, the MicroBooNE detector [53] boasts an 85-ton active-mass LAr-TPC and has been collecting data since October 2015, completing seven years of data acquisition by 2021. Serving as the far detector of the SBN program, ICARUS [5] is located just downstream of MicroBooNE, 600 m from the BNB target. With an active mass of 476 tons of LAr-TPC, it furnishes complementary data to MicroBooNE and SBND, increasing the statistics for potential signal detection.

3.2 The LAr-TPC Technology

C. Rubbia originally proposed using LAr-TPC technology for a neutrino detector in 1977 [65]. Its operational principle is based on detecting the ionization charge

released by charged particles passing through a volume of LAr. These detectors collect both light and charge. When a neutrino enters the detector and interacts with an argon atom, this interaction produces tracks with ions and photons along them. The photons propagate inside the detector, and the scintillation light is collected by the photomultiplier tubes (PMT) for precise timing and calorimetry of the events. The ionized electrons will slowly drift toward the anode by applying a uniform electric field to the medium [67], as shown in Fig. 3.2. A system of three successive

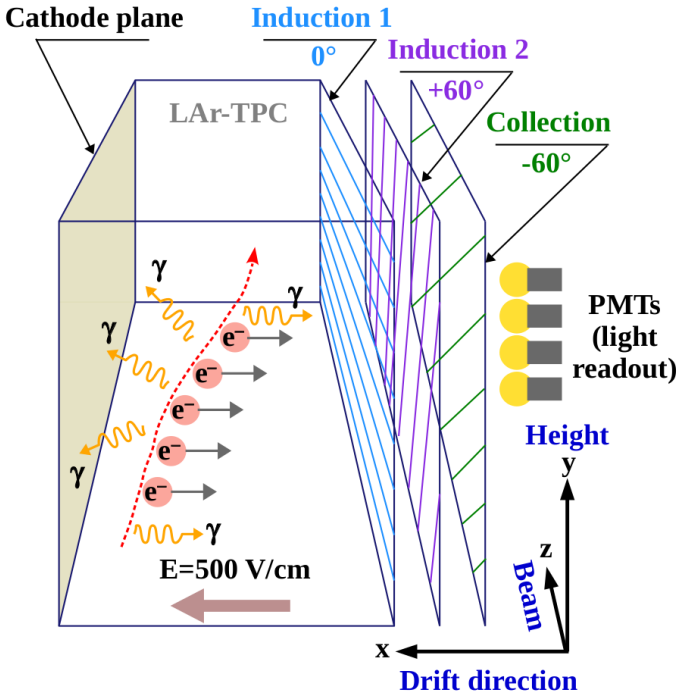

Figure 3.2: ICARUS LAr-TPC readout scheme.

wire planes polarized at different potentials allows simultaneous and independent detections of the drifting charge signal. The ionized electrons produce induction signals as they pass the first couple of wire planes and are collected on the last wire plane. The wires are oriented in each plane at different angles, Induction 1 at 0°, Induction 2 at +60°, and the Collection plane at -60°. Therefore, a three-dimensional image can be reconstructed by combining the coordinates of the wires in each plane

at a given drift time. The measurement of the T_0 *time*, associated with the passage of the particle through the active medium, along with drift velocity information, offers the tracks absolute position along the drift coordinate [68].

LAr-TPC detectors are highly sensitive and self-triggering, enabling them to provide excellent 3D imaging, calorimetric reconstruction of any ionizing particle, and efficient particle identification. Detailed images of particle trajectories provide crucial information on final states, and the high spatial resolution allows for precise tracking. Therefore, LArTPC technology facilitates the study of neutrino properties with high precision.

3.3 ICARUS Neutrino Beams: BNB and NuMI

The ICARUS-T600 detector is situated along two neutrino beamlines: it is positioned on the axis of the Booster Neutrino Beamline (BNB), and approximately 6° off-axis from the Neutrinos produced at the Main Injector (NuMI) beamline. The NuMI neutrino beam is generated at Fermilab using protons accelerated to 120 GeV from the Main Injector, while the Booster beam is produced using protons accelerated to 8 GeV from the Booster at Fermilab.

The particle acceleration process at Fermilab involves several stages (illustrated in Fig. 3.3), starting with the injection of gaseous hydrogen into the ion source to generate negatively charged hydrogen ions (H-) [69]. These ions are then extracted from the source at 18 keV and undergo pre-acceleration to reach a beam energy of 750 keV before being injected into the linear accelerator, known as the Linac. Within the Linac, the ions are accelerated to 400 MeV and subsequently directed to the Booster.

The Booster, a synchrotron with a radius of 75.47 meters, receives 500 MeV H- ions from the Linac, where the electrons are stripped off, and the remaining protons are accelerated to 8 GeV. This process involves 17 radio frequency (RF) cavities,

with the frequency ranging from 37.8 MHz at injection to 52.8 MHz at extraction to match the Main Injector (MI) frequency. The injection process lasts ten Booster turns, resulting in an average current of 420 mA. The injected beam comprises bunches equally spaced at the Linac RF frequency of 201.2 MHz.

Moving forward, the Main Injector, another synchrotron with a radius of 528.30 meters, operates with a 2.2-second acceleration cycle. It receives 8 GeV protons from the Booster and accelerates them to 120 GeV.

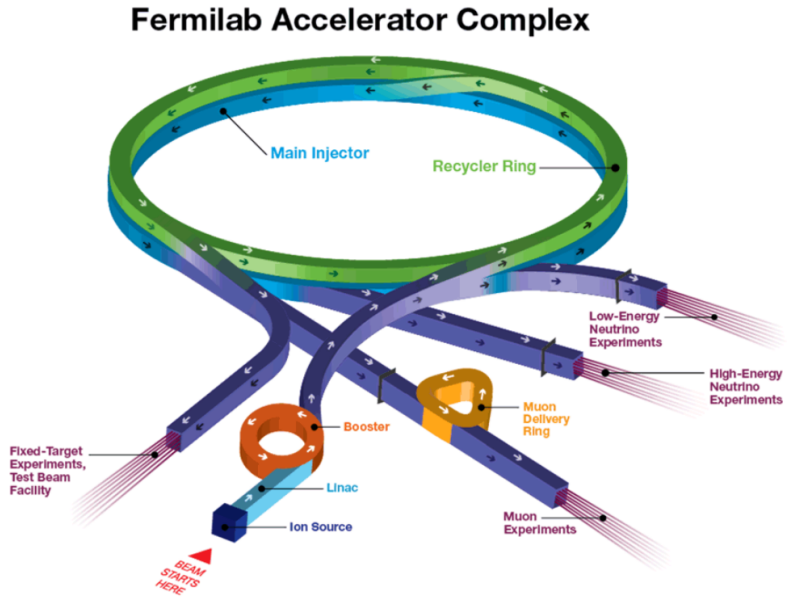

Figure 3.3: Fermilab Accelerator Complex. Image taken from [70].

3.3.1 Generating Neutrino Beams

Booster

The proton beam for the Booster begins as a flow of negatively charged hydrogen ions, H-. These ions undergo acceleration in a linear accelerator (Linac), where alternating electromagnetic fields propel them to a kinetic energy of 400 MeV. Electrons are stripped from the H- ions as they pass through a carbon foil. Subsequently, the

naked protons are injected into the Booster synchrotron, which boasts a circumference of 474.2 meters and operates at a frequency of 15 Hz. Within the synchrotron, the protons are ramped up to 8 GeV.

The protons are collected into *beam spills*, each one containing approximately 4×10^{12} protons distributed over a time window of 1.6 μs per spill [5]. These protons are then directed towards a dense beryllium target. Upon collision with the target, the protons generate particles, primarily pions (π) and kaons (K), with π being the dominant source.

The positively charged mesons resulting from the collision are focused, passing through a collimator before entering a 50-meter-long decay volume. Within this volume, the mesons decay into neutrinos, following the decay chains: $\pi^+ \rightarrow \mu^+ + \nu_\mu$ and $K^+ \rightarrow \mu^+ + \nu_\mu$ (the μ produced by these decays, in turn, can decay as $\mu^+ \rightarrow e^+ + \nu_e + \bar{\nu}_\mu$). The remaining mesons and muons are absorbed by the beam absorber situated at the end of the decay volume. The entire process is illustrated in Fig. 3.4.

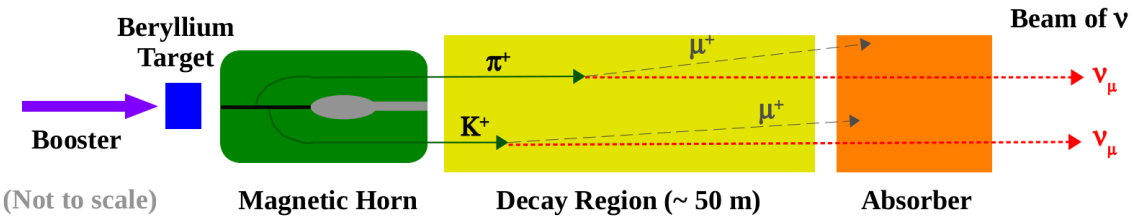

Figure 3.4: Schematic of neutrino production at BNB.

NuMI

The NuMI neutrino beam is generated by focusing 120 GeV protons from the main injector onto a graphite target [71]. This interaction produces mesons (pions and kaons) through hadronic interactions, predominantly pions. These mesons are then focused by pulsed toroidal magnets called *horns* and then enter a 675 m long decay pipe to produce a neutrino beam, when these horns are powered in forward horn

current (FHC) mode. A change of polarity of the current through the horns produces a beam of antineutrinos when the horns are powered in reverse horn current (RHC) mode. Mesons decay mainly through the channels $\pi^+ \rightarrow \mu^+ + \nu_\mu$ and $K^+ \rightarrow \mu^+ + \nu_\mu$, and muons, in turn, decay and produce $\mu^+ \rightarrow e^+ + \nu_e + \bar{\nu}_\mu$. At the end of the decay pipe is a hadron monitor in front of the 5 m thick absorber to record the residual hadron profile. The absorber attenuates these residual hadrons to negligible numbers. The absorber is followed by three muon monitors to measure the residual muon flux and a rock of about 240 m to stop the muons, leaving only the neutrinos to pass through.

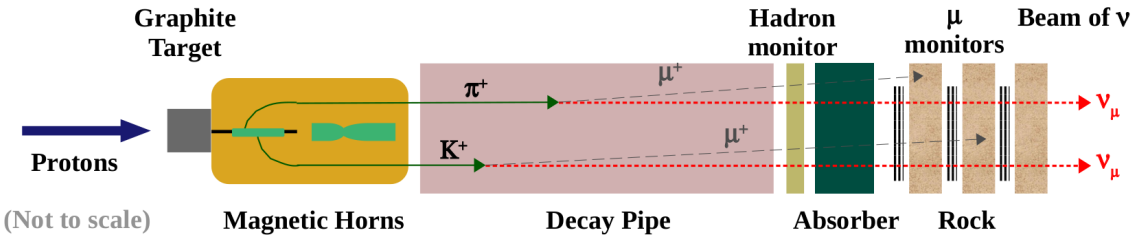

Figure 3.5: Schematic of neutrino production at NuMI.

In the next Chapter 4, we will study the interactions of neutrinos from the NuMI beam with the Argon nuclei of the ICARUS detector.

3.3.2 The Neutrino Energy

As discussed in the previous section, ν_μ beams are produced by allowing a focused beam of charged pions/kaons to decay into a long decay region, followed by an absorber to remove unwanted pions/kaons and muons. These neutrinos have an isotropic angular distribution in the rest frame of the decaying meson. The neutrino energy in the laboratory frame depends on the energy of the pions/kaons, $E_{\pi/K}$, and on the angle θ_ν between the resulting neutrino and the decaying pions/kaons. This energy is given by

$$E_\nu = \frac{m^2_{\pi/K} - m^2_\mu}{2E_{\pi/K}(1 - \beta\cos\theta_\nu)}\,, \tag{3.1}$$

here, $\beta = \sqrt{1 - \frac{1}{\gamma^2}}$, where β and γ are the Lorentz parameters of the pion/kaon with energy $E_{\pi/K}$ in the laboratory frame, m_μ is the muon mass, and $m_{\pi/K}$ is the mass of the pion/kaon.

For ultra-relativistic pions/kaons ($\gamma \gg 1$), neutrinos are typically produced at very small angles. In this case, the neutrino energy will be

$$E_\nu \simeq \frac{(1 - \frac{m^2_\mu}{m^2_{\pi/K}})E_{\pi/K}}{(1 + \gamma\theta^2_\nu)}\,. \tag{3.2}$$

Chapter 4 will show the ν_μ flux for the scenario of the NuMI beam incident on the ICARUS detector. It will be observed that neutrinos coming from pion decays are predominant at low energies (hundreds of MeV), whereas neutrinos from kaon decays dominate around an energy of 2 GeV.

3.4 The ICARUS-T600 Detector

The Imaging Cosmic And Rare Underground Signals experiment, ICARUS, represents a pioneering initiative in neutrino detection technology. The ICARUS-T600 detector is the first large-scale implementation of liquid argon time projection chamber technology (LAr-TPC) for neutrino detection, as proposed by Carlo Rubbia in 1977 [65].

Operating within the Italian Gran Sasso National Laboratory for 3 years, between 2010 and 2013 [72], the ICARUS-T600 detector showcased the operational efficacy of a large-scale, high-purity LAr detector in underground conditions. Moreover, it conducted pivotal studies, including the measurement of neutrino velocity and searches for neutrino oscillations, utilizing the CERN Neutrinos to Gran Sasso (CNGS) beamline, located 730 kilometers away in Switzerland [73].

Following its tenure at Gran Sasso, the ICARUS-T600 detector underwent refurbishment at the European laboratory CERN in 2014. This refurbishment aimed to prepare it for integration into the SBN program at Fermilab. Consequently, in 2017, the ICARUS-T600 detector was transported to its new home at Fermilab in Chicago, Illinois, USA.

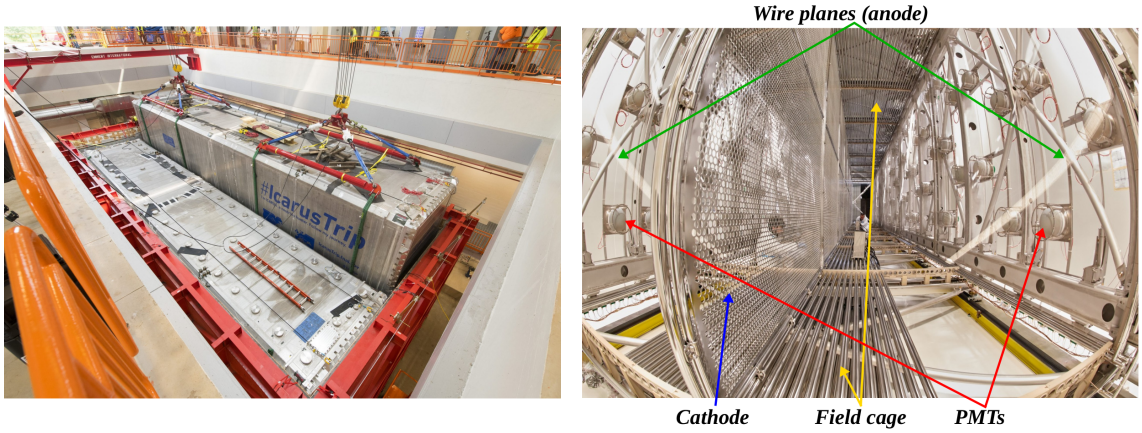

(a) Installation of the ICARUS-T600 modules.

(b) Inside an ICARUS-T600 module.

Figure 3.6: (a) Installation of the ICARUS-T600 modules into the SBN far detector building at Fermilab. (b) Internal view of an ICARUS-T600 module showcasing the wire planes, cathode, field cage, and PMTs of its two TPCs [74].

The ICARUS-T600 detector consists of two identical adjacent modules [5], see Fig. 3.6, each one with internal dimensions of 3.6 m along the drift direction, 3.9 m in height, and 19.6 m along the BNB direction. Together, the modules were filled with 760 tons of ultrapure liquid argon, resulting in a total active mass of 476 tons. Inside each module there are two LAr-TPCs, separated by a common cathode with a maximum drift distance of 1.5 m, corresponding to approximately 1 ms of drift time under the nominal electrical drift field of 500 V/cm.

The cathode consists of nine panels made of punched stainless steel, providing 58% optical transparency between the two drift regions. On the other hand, the an-

ode comprises three parallel wire planes positioned 3 mm apart, featuring stainless-steel wires with a thickness of 150 μm. The wires on each plane are oriented at different angles relative to the horizontal direction: Induction 1 at 0°, Induction 2 at +60°, and the Collection plane at -60°. In total, the detector is equipped with 53,248 wires, each one with a 3 mm pitch and lengths of up to 9 m. There are a total of 360 photo-multiplier tubes (PMTs) located behind the wire planes, as shown in Fig. 3.6b, used to collect the scintillation light produced by charged particles in LAr and for triggering the detector.

Figure 3.7: ICARUS-T600 CRT system surrounding the detector [5].

At Fermilab, ICARUS-T600 encounters a significant challenge due to its shallow depth. The influx of cosmic rays into the detector constitutes a primary source of background. Therefore, it is imperative to mitigate the impact of incoming cosmic ray events and effectively discern neutrino interactions from the cosmic ray background. To discriminate cosmic rays, a 3-m thick concrete overburden was engineered to attenuate contributions from charged hadrons and high-energy photons. However, approximately 11 muon tracks are observed per triggered event in the 1 ms TPC drift readout. Precision timing for every track captured by the TPC is vital for distinguishing the cosmic ray background. To achieve this goal, ICARUS employs an enhanced light detection system with high granularity. Additionally, an external cosmic ray tagger (CRT) encircling the detector has been incorporated, primarily

designed to identify muons traversing through or near the ICARUS cryostats. The ICARUS CRT comprises top, side, and bottom subsystems, as shown in Fig. 3.7. Timestamps associated with particles tagged by the CRT are cross-referenced with timestamps from PMT signals, both offering nanosecond resolution, to ascertain whether an interaction in the TPC originated from an external cosmic ray or an internal source.

3.5 Commissioning Period of ICARUS at Fermilab

After refurbishment activities at CERN, ICARUS-T600 moved to Fermilab in July 2017, and the two cryostats containing the TPCs were finally positioned in their shallow location within the SBN Far Detector Hall by August 2018. In May 2019, the collaboration installed and tested the electronics for the detector chimneys. Fig. 3.8 shows images of the electronics that we tested during this period. Subsequent efforts involved installing and testing of all major subsystems before cryogenic commissioning commenced in July 2019.

During the commissioning phase, which commenced in January 2020, testing was conducted on the TPC and PMT systems, which became operational by August 2020. Concurrently, ICARUS-T600 initiated data collection using the BNB and NuMI beams in March 2021. The data collected during this period served various purposes, including refining the trigger system, calibrating the detector, conducting reconstruction studies, and visually identifying the first neutrino interactions in ICARUS at Fermilab, as illustrated in Fig. 3.9.

In 2021, the installation of the CRT system surrounding the detector was completed, followed by operational and monitoring tests. Subsequently, in June 2022, a 3-meter layer of concrete (equivalent to 6 meters of water) above the top of the CRT system, acting as a cosmic ray shield for the detector, was completed.

Figure 3.8: In May 2019, I assisted with the installation and testing of the ICARUS chimneys, including testing the boards used for reading the detector data. At the top left, two ICARUS Low Voltage Power Supply (LVPS) modules [75] are shown, powering two adjacent mini-crates. The bottom left image displays an ICARUS mini-crate containing nine A2795 boards. On the right side is a view of the top of the detector.

3.6 Physics-Quality Data Runs and Current Status of ICARUS

It is important to emphasize that the commissioning period was completed after installing of the 3 m overburden. Until that moment, cosmic rays entering the detector constituted the primary source of particles, complicating the study of neutrino interactions within the detector. Consequently, after the installation of the overburden, which reduced the influx of cosmic rays to the detector, in June 2022, ICARUS initiated the collection of physics-quality data using both the BNB and NuMI neutrino beams. This initial data collection phase lasted approximately one month and was aimed to assess the performance of the detector, laying the groundwork for the first physics analyses of ICARUS.

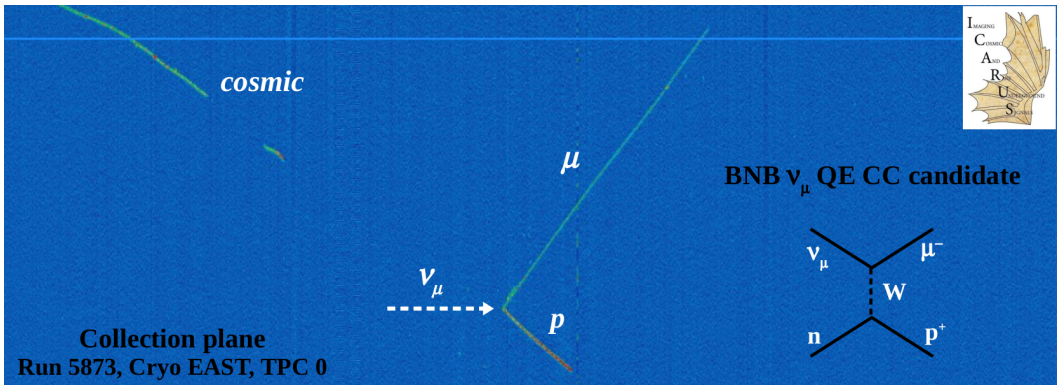

Figure 3.9: Visual identification of the first neutrino candidates during the commissioning period. This candidate corresponds to a Charge Current Quasi-Elastic ν_μ interaction from the BNB. It shows a view in the collection plane, where muon (μ) and proton (p) tracks can be observed as final states originating from a common point, corresponding to the interaction vertex.

During the first physics-quality data collection run (Run 1), various aspects of the detector were refined, including calibration, the TPC and PMT systems, and event reconstruction. Additionally, the performance of the CRT system was tested. Fig. 3.10 presents a plot from an initial study conducted with data collected during this period. The plot compares the manually measured z-coordinate of the interaction vertex for a BNB ν_μ candidate, visually identified, with the z-coordinate measured by automatic reconstruction of the same candidate. A more complete analysis of this study, involving candidates from the second physics run (Run 2), will be presented in Section 3.8.

Currently, the experiment is in the phase of analyzing data from the second period of physics data acquisition and taking data for the third physical run period.

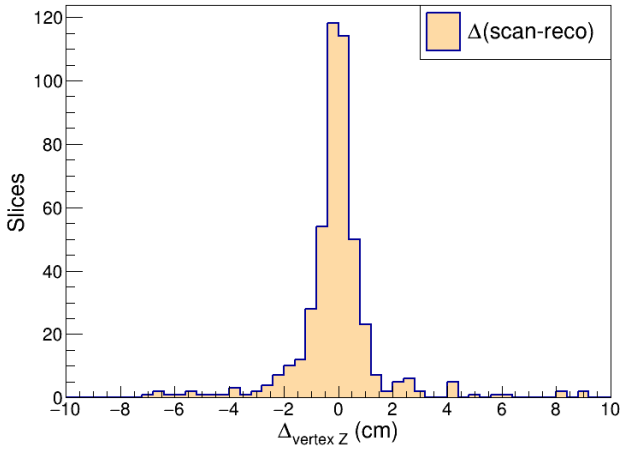

Figure 3.10: Difference between the z-coordinate (beam coordinate) measured by automatic reconstruction and manual measurement (visual scanning) of the interaction vertex for muon neutrino candidates from a sample of 476 ν_μ events in the BNB beam.

3.7 Event Reconstruction

The neutrino interactions analysis is based on the information provided by the different detector components, including the TPC, PMT, and CRT. The TPC records signals induced by ionization electrons during a drift time of approximately 1 ms. As previously discussed, it consists of three wire planes positioned at 0° and ±60° relative to the horizontal direction. The TPC provides a 2D visual image with a millimeter spatial resolution per wire plane. Combining the images from the three wire planes results in a 3D event reconstruction. Additionally, the TPC facilitates calorimetric reconstruction of deposited energy, particle identification by measuring dE/dx versus residual range for stopping particles, track and shower distinction, and discrimination of single electrons and gamma rays by measuring the initial dE/dx of the shower. The PMTs utilize scintillating light to provide event triggers, accurately time events, and locate them within the TPC. On the other hand, the CRT sys-

tem serves to reject cosmic rays by vetoing incoming ones, distinguishing between incoming and outgoing particles, and identifying out-of-spill events.

Below, we briefly describe the processing chain for TPC signal reconstruction. The TPC reconstruction process begins with raw data, consisting of waveforms representing the charge induced on the sense wires over drift time. Initially, these waveforms undergo a filtering algorithm to reduce noise introduced by the electronics. Following noise filtering, an algorithm identifies candidate peaks in the waveforms by requiring them to exceed a configurable threshold. These candidate peaks are fitted with a Gaussian function to derive a *hit*, indicating the charge deposited on a wire by an incident track. Following this, hits are grouped into clusters through a clustering algorithm designed to associate hits corresponding to the same particle signature, such as a track or a shower.

ICARUS at FNAL utilizes Machine Learning (ML) and the Pandora [76] multi-algorithm pattern recognition framework for TPC event reconstruction. The TPC event reconstruction method employed in this work will be that performed by Pandora, which reconstructs 3D particle trajectories from hits on the TPC wire planes. The output from Pandora [77] is organized into Particle Flow reconstructed particles, PFParticles. Each PFParticle is classified as either track-like (e.g., muons, protons, charged pions, etc.) or shower-like (e.g., electrons, photons, etc.), with their hierarchical parent-daughter relationships identified, describing the particle flow within observed interactions. Additionally, Pandora reconstructs the common vertex point where the interaction originates within the detector volume.

Calorimetry in LArTPCs is fundamental for measuring the energy deposited by charged particles as they travel through the detector. LArTPCs function by recording the ionization electrons produced when charged particles pass through liquid argon. These ionization electrons drift towards an anode under the influence of an electric field, where they are collected and digitized. The amount of charge

(ionization) collected is proportional to the deposited particle energy, which is a key aspect of calorimetry.

In the Pandora reconstruction tool, for each reconstructed track, Pandora calculates the total energy deposited by summing the charge collected along the track. This requires corrections for electron lifetime (to account for charge loss due to recombination) and variations in the electric field. It is possible to calculate the energy deposition per unit length (dE/dx) along the track. This quantity is essential for constructing the particle identification (PID), as different particles have characteristic dE/dx profiles. By comparing the calculated dE/dx with expected profiles for various particle types, Pandora can identify the most likely particle responsible for each track. The capabilities of this tool will be implemented for the selection and identification of muon neutrino candidates in Chapter 4 of this work.

In the data analysis performed for the MicroBooNE experiment, two Pandora algorithm reconstruction paths were developed [77]. These paths have been adopted for the analysis of ICARUS data, as well as other experiments such as SBND, 2x2, etc. On the one hand, the *PandoraCosmic* reconstruction path is dedicated to reconstructing cosmic ray muons and their daughter delta rays [1]. On the other hand, the *PandoraNu* path is focused on the reconstruction of neutrino interactions.

The *PandoraCosmic* reconstruction initially processes all hits identified within a specific readout window, generating a list of candidate cosmic ray particles. Subsequently, this particle list undergoes examination by a cosmic ray tagging module integrated within LArSoft, which identifies cosmic ray muons based on their initial

[1]Delta rays [78] are secondary electrons ejected from atoms when struck by a high-energy charged particle, such as a cosmic ray. These electrons can have enough energy to ionize other atoms along their path, creating additional ionization tracks.

The term 'delta ray,' introduced by British physicist J.J. Thomson, is sometimes used to describe any recoiling particle that causes secondary ionization. The Pandora software identifies these particles as showers [77].

and final positions and associated hits. Hits associated with particles identified as cosmic ray muons are then excluded from the input hit collection, creating a new collection of "cosmic ray removed hits." This secondary collection provides data for the *PandoraNu* reconstruction, which compiles a list of neutrino candidates.

It's important to note that while the *PandoraCosmic* and *PandoraNu* reconstruction paths share several similarities, there are differences between them, as follows [77]:

PandoraCosmic: This reconstruction path prioritizes tracking and predominantly identifies primary particles as cosmic ray muons. Showers are typically interpreted as delta rays and are incorporated as daughter particles of the most appropriate cosmic ray muon. The reconstructed vertex or starting point for the cosmic ray muon is determined by the y-high coordinate (top of the detector) of the muon trajectory.

PandoraNu: In contrast, this reconstruction path focuses on identifying a vertex for a neutrino interaction, utilizing it to guide the reconstruction of all particles emerging from this position. The reconstruction process involves careful tracking and shower reconstruction. A mother neutrino particle is created, and the reconstructed visible particles are then added as daughters of the neutrino.

In Pandora, the 3D hits are divided into slices. A *slice* represents a specific interaction or a group of interactions [77]. The slicing process involves segmenting the continuous stream of data recorded by the LArTPC into pieces. Each slice contains information about the ionization electrons produced by charged particles as they travel through the liquid argon, including their positions, times, and collected charges. The slicing process is essential for reconstructing individual particle trajectories and interactions.

Fig. 3.11 shows the reconstruction, conducted by Pandora, of a slice in each of the three wire planes. This slice corresponds to an interaction involving a muon neutrino

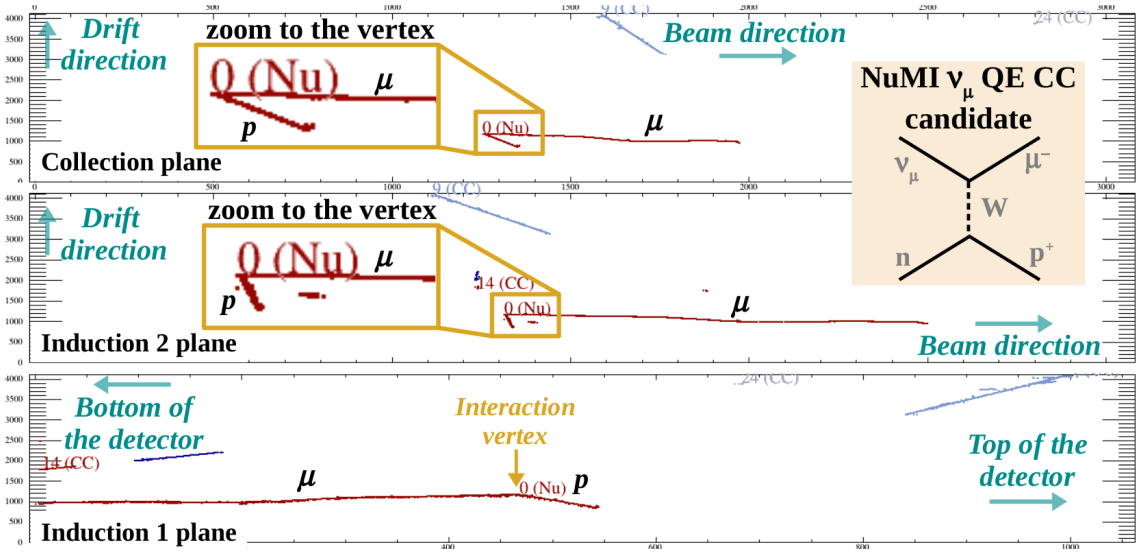

Figure 3.11: View of the LArSoft Event Display in slice mode, showing an example of a ν_μ candidate.

and an Ar nucleus of the ICARUS detector. The reconstructed slice consists of two distinct tracks: one representing a muon track and the other a proton track. These tracks are the final state of the interaction, converging at a common point, which corresponds to the vertex of the interaction.

3.8 Reconstruction of Muons from Muon Neutrinos Candidates

Several studies have been conducted to validate the TPC reconstruction processes. Among these, a cross-check was performed comparing the positions of both the interaction vertex and the ends of muon tracks between the reconstruction done by Pandora and the information obtained from a visual scan of the neutrino interaction candidates. The visual scanning process involves manually evaluating events using an event display and code that works with the waveforms of hits read directly from

the wires in the TPC planes. Neutrino candidates can be identified using this information and other considerations. However, this method becomes cumbersome when dealing with a large number of candidates, which is why validation with automated reconstruction software, such as Pandora, is necessary. This section will show and discuss the results obtained after performing the cross-check mentioned here.

3.8.1 Candidate Distribution in the ICARUS Detector

As mentioned in Section 3.4, the ICARUS detector is composed of two identical modules (i.e., two cryostats), each containing two TPCs. The active volume refers to the region within the detector where neutrino interactions can be detected and reconstructed. The geometrical dimensions of the active volume of the ICARUS detector are as follows:

- the x-direction, parallel to the drift direction (east $\rightarrow$ west):

  -358.49 cm $<$ x $<$ -61.94 cm and 61.94 cm $<$ x $<$ 358.49 cm,

- the vertical y-direction (bottom $\rightarrow$ top):

  -181.86 cm $<$ y $<$ 134.96 cm, and

- along the beam z-direction (upstream-downstream):

  -894.95 cm $<$ z $<$ 894.95 cm.

The gap between -61.94 cm and 61.94 cm along the x-direction (drift direction) is due to the physical separation of the cryostats.

Fig. 3.12 shows the active volume of the ICARUS detector, represented by the orange rectangles. Within this active volume, the interaction vertices of 422 ν_μ candidates from run 9435, part of the second physics-quality data acquisition run by the ICARUS experiment, are illustrated. It can be observed that the distribution of events is relatively homogeneous throughout the detector.

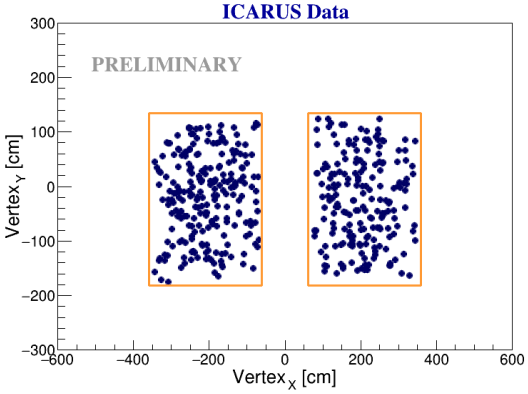

(a) Vertices x-y

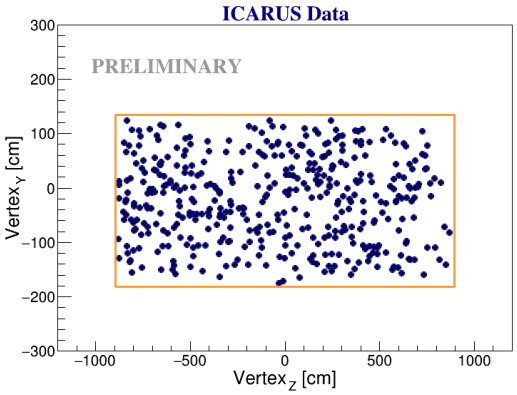

(b) Vertices y-z

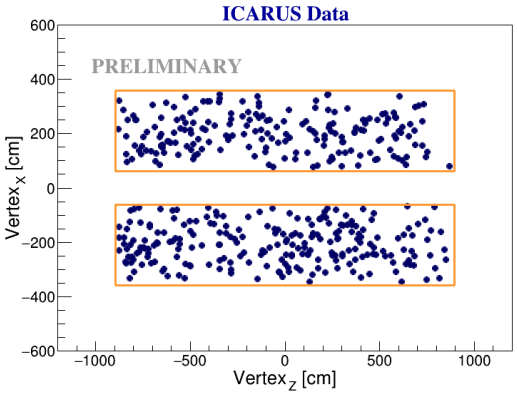

(c) Vertices x-z

Figure 3.12: 2D distributions of the interaction vertex positions for the 422 interactions from run 9435, reported by the scanning group, are shown along the (a) x vs. y, (b) y vs. z, and (c) x vs. z directions.

It should be noted that we consider events where the positions of both the interaction vertices and the ends of the muon tracks were found within the active volume of the detector, both with the reconstruction information and the visual scan information. In the following sections, we will study in more detail the comparison of the positions using the reconstruction information and the visual scan information for both the interaction vertices and the ends of the muon tracks.

3.8.2 Reconstruction of Interaction Vertices and End of the Muon Tracks

Fig. 3.13 shows an example of a muon neutrino (ν_μ) candidate from the Booster beam that interacted with the detector. At the top of the figure is an image of the candidate with the Event Display (TITUS) [79] in the collection plane used by the visual scan. The lower part of the figure shows the same event in the same plane but with an Event Display (LArSoft Event Display) used by the reconstruction. This is a fully contained event within the active volume of the detector.

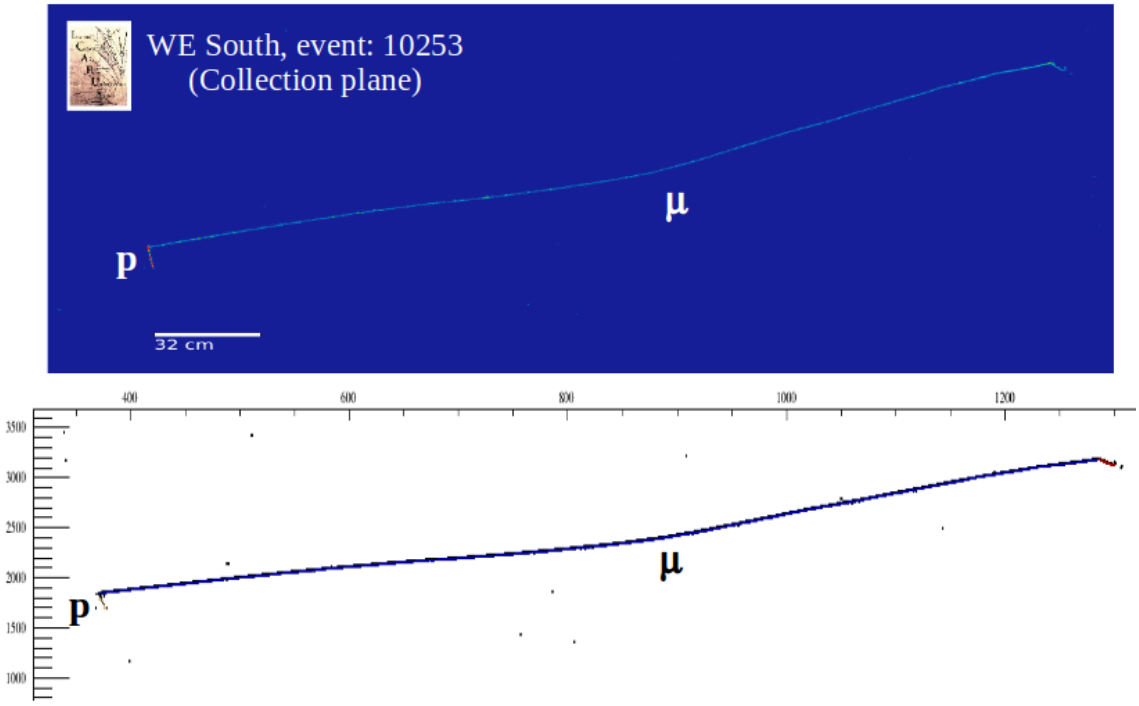

Figure 3.13: Fully contained ν_μ candidate where there are 1-muon with a length of 290 cm and 1-proton of 11 cm at the final state. Event display views of visual scan (upper panel) and reconstruction (lower panel). Further details in the text.

In this image, the interaction point can be seen on the left side, corresponding to the vertex from which the two tracks originate: the muon track and the proton

track. The lengths of the tracks are different because the proton, having a greater mass than the muon, decays more quickly, leaving a shorter track. The muon, which takes longer to decay, has a longer track. The muon decay in this figure can be seen at the end of the track on the right side. A small kink, which appears brown in the reconstruction event display, is observed. This kink corresponds to a Michel electron, characteristic of muon decay.

Figs. 3.14a, 3.14b, and 3.14c show the differences between the interaction vertex positions reported by the visual scan $(x, y, z)_{scan}$ and the positions obtained by the reconstruction $(x, y, z)_{reco}$:

$$\Delta(scan - reco) \equiv (x_{scan} - x_{reco}, y_{scan} - y_{reco}, z_{scan} - z_{reco})\,. \tag{3.3}$$

As can be seen, Gaussian distributions are obtained with means around 0, indicating good agreement between the values reported by the visual scan and those obtained by the reconstruction. The orange distribution corresponds to the differences of the 422 events. It should be mentioned that these differences vary from a few centimeters to even meters.

The green distribution shows the events with a difference $\Delta(scan-reco) \leq 15$ cm. As can be seen, 342 of the 422 events (81% of the total sample) have differences of less than 15 cm. Finally, in blue the events with $\Delta(scan - reco) \leq 2$ cm were studied. In this classification, 245 of the 422 events (58.1% of the total sample) had differences in the interaction vertex positions of less than 2 cm.

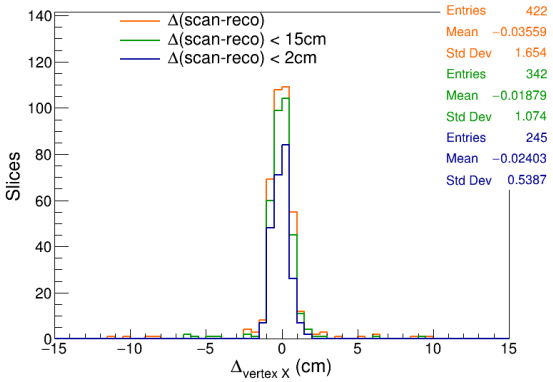

(a) Vertices X

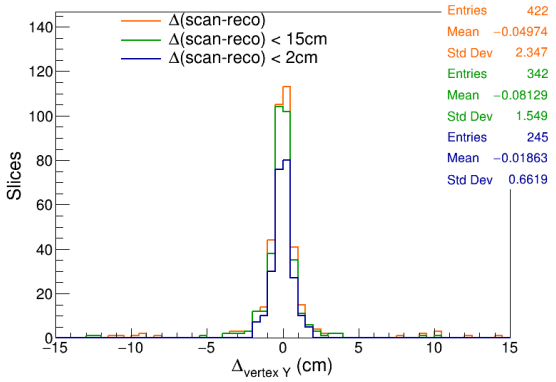

(b) Vertices Y

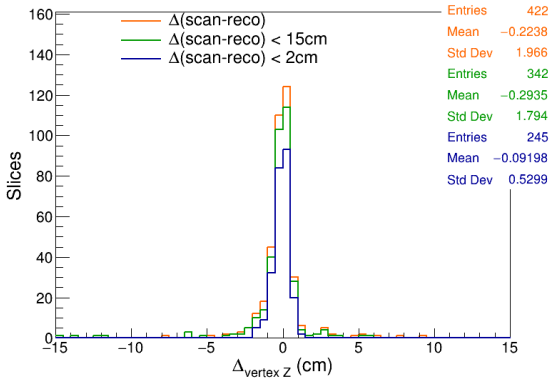

(c) Vertices Z

Figure 3.14: Distributions of the $\Delta(scan-reco)$ differences for the vertex positions: (a) x, (b) y, and (c) z. The orange distribution represents the $\Delta(scan-reco)$ of the total sample of 422 ν_μ candidates. The green distribution corresponds to $\Delta(scan-reco) \leq 15$ cm, and the blue distribution corresponds to $\Delta(scan-reco) \leq 2$ cm. Further details in the text.

A similar study was conducted for the ends of the muon tracks, yielding comparable results. It should be remembered that this study focuses on the final state of the interactions, specifically the μ tracks in this case (as a final state of ν_μ interaction). A similar study was initiated for proton tracks, but it is still ongoing.

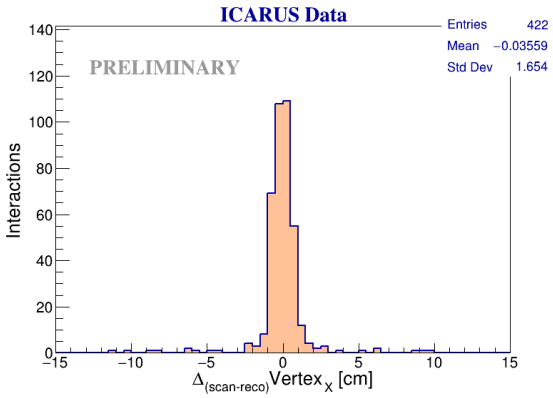

(a) Vertices X

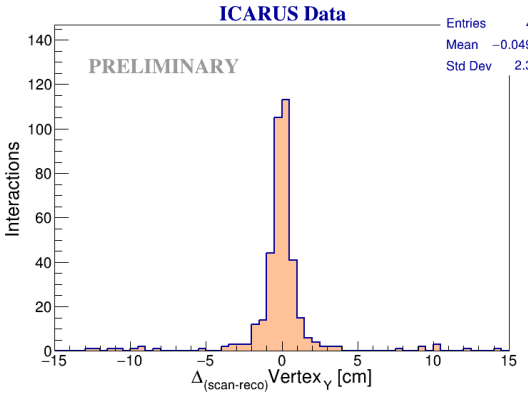

(b) Vertices Y

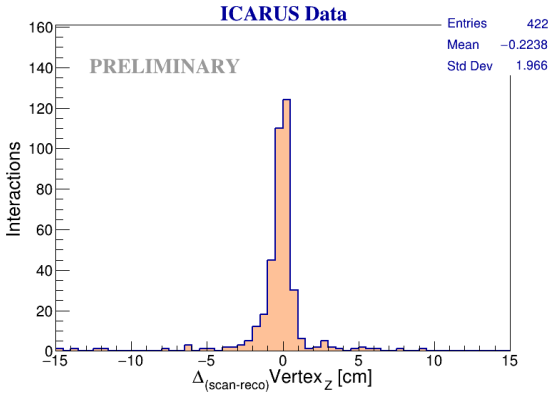

(c) Vertices Z

Figure 3.15: The visual scan and automatic reconstructions were compared for a sample of 422 candidate interactions from run 9435. In these plots a zoom in the range (-15,15) cm in the difference between scan and reco vertex coordinates (a) x, (b) y, and (z) z are drawn. As a result, 393/422 interactions are visible, meaning that the remaining 29 interactions lie on the tails of the distribution.

Again, in Fig. 3.15, the distributions of the 422 events are shown. A series of selection criteria were applied to the reconstructed events (similar to those that will be studied in Section 4.5 of Chapter 4), where various geometric parameters, Pandora reconstruction parameters, and calorimetry information were evaluated.

Below, these parameters and the results obtained by applying them to this sample of 422 ν_μ candidates are listed.

- The distance between the interaction vertex and the start of the candidate track is within 10 cm. In this classification, 336 events were found, equivalent to 79.6% of the total sample.

- The length of the muon track is $\geq$ 50 cm. In this classification, 397 events were found, meaning 94.1% of the sample showed distances greater than 50 cm.

- As studied in Section 3.7, Pandora can classify cosmic (as *PandoraCosmic*) and neutrino (*PandoraNu*) events. Applying this condition to the sample, 97.6% of the events (412 of 422) were classified as *PandoraNu* (or non-clear cosmic).

- It was found that 390 events, equivalent to 92.4% of the muons in the sample, had their *PFParticle* classified as a primary particle.

- On the calorimetry side, as can be seen in Fig. 3.16, 397 events (94.1%) had a χ^2_μ score < 30, while 405 events (96%) had a χ^2_p score > 60.

When applying these combined selection criteria, it was found that only 306 of the 422 events passed the entire selection, resulting in an efficiency of 72.5%.

Thanks to this study, several inconsistencies (or pathologies) were identified and resolved on both the reconstruction side and the visual scan side. All these adjustments and refinements have been implemented in the codes to process (or reprocess) the data, ensuring that the reconstruction tool used for the physics analysis is adjusted and calibrated to obtain and report reliable results.

The following section will present some of the pathologies that still persist in the reconstruction and are currently under study.

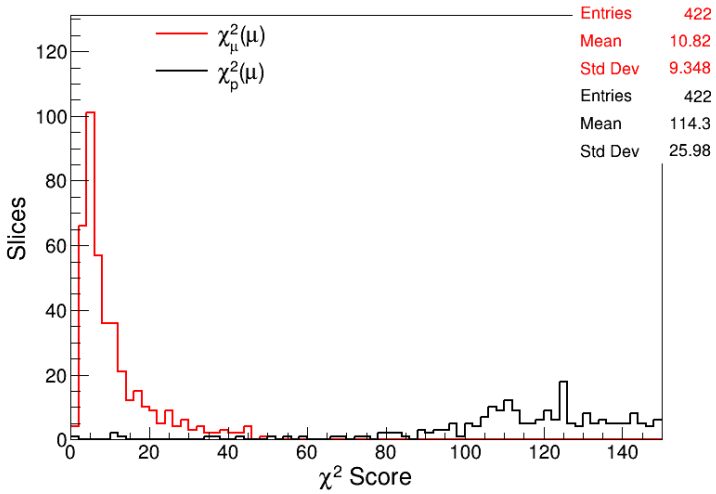

Figure 3.16: The χ^2-based Particle ID scores from the reconstructed muon candidates are shown. χ^2_μ (muons) is represented by the red distribution, while χ^2_p (protons) is shown in black. These distributions serve as thresholds to identify muon candidates in the event selection process.

3.9 Reconstruction Pathologies

Although the reconstruction performed by Pandora is generally good, several inconsistencies have been identified. In the sample of 422 events studied in the previous section, 68 events (corresponding to 16.1% of the sample) showed one or more of the following pathologies:

- Split Muon Tracks: In 22 events, the muon track was split into two parts. This pathology will be discussed in more detail below, as it contributes to systematic detector errors.

- Vertex and Track End Mismatch: In 19 events, either the reconstruction of the vertex or the end of the muon track was found to be in good agreement with that reported by the visual scan, but not both. Specifically, either the vertex was accurately reconstructed while the end of the muon track was not,

or vice versa. This issue may be due to multiple splits in the muon track, with some segments being misclassified as showers. This is still under investigation.

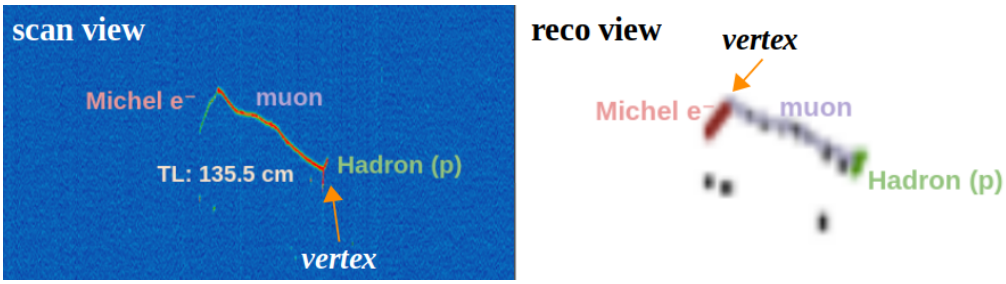

Figure 3.17: Event exhibiting the pathology of having the interaction vertex flipped with the end of the μ track, where it decayed into a Michel electron. The left panel shows the Event Display with the visual scan information, while the right panel shows the same event in the Event Display of the reconstruction, where the vertex appears at the location of the Michel electron.

- Flipped Vertex and Track End: In 16 events, the vertex of interaction and the end of the muon track were flipped. This generally occurs in events where the muon track decays.

  $$\mu \rightarrow e + \nu_e + \nu_\mu$$

  During muon decay, a Michel electron appears (which should be classified as a shower by Pandora), and in some cases, the reconstruction software incorrectly identifies this point as the vertex of the interaction, see Fig. 3.17. Studies are ongoing to understand and resolve this pathology. Preliminary work involves reanalyzing the events using a 2D deconvolution of the reconstruction software and refining the detector calibration.

- No Matches: In 7 events, no match was found with the track classification or any of the aforementioned pathologies. The issue of splitting tracks into multiple tracks, mixing with other events (e.g., cosmics), and/or the possibility of misclassification as showers are being explored.

Studies are ongoing to better understand the nature of these pathologies and to develop solutions. All adjustments and refinements will be implemented in the reconstruction software to ensure accurate and reliable results.

3.9.1 Split Tracks

The pathology of split tracks refers to the division of tracks (particularly muon tracks, which are being studied) into two or more parts. Specifically, cases where the reconstructed muon track is split into two tracks, will be studied, with one of these reconstructed tracks coinciding with the interaction vertex reported by the visual scan and the other coinciding with the end of the muon track from the visual scan.

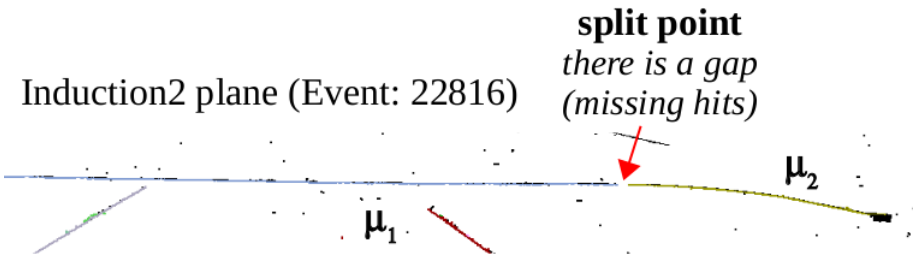

Figure 3.18: Example of the pathology where the muon track is split into two parts, μ_1 in gray and μ_2 in yellow. At the split point, there is a gap that divides both tracks.

Fig. 3.18 shows an example of the pathology of a split track. In this figure, it can be seen that at the split point some hits are missing, forming a gap of approximately 3 cm, between the track corresponding to the μ_1 chunk (in gray) and the track of the μ_2 chunk (in yellow). An interesting observation is that in addition to the gap, there seems to be a small bend causing the direction of the end of μ_1 to differ from the direction of the start of μ_2. This might be a reason why the Pandora algorithm did not relate both pieces as part of the same track.

Another case where the directions between the end of one chunk of the track and the start of the other chunk differ can be seen in Fig. 3.19. At the split point, there appears to be a kink; again, the direction of the end of μ_1 is different from the direction of the start of μ_2.

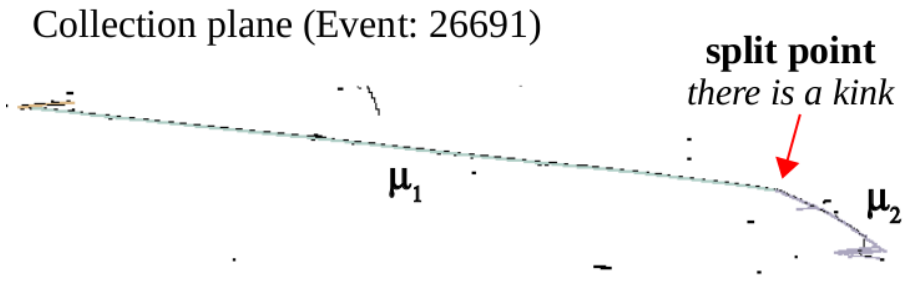

Figure 3.19: Example of the pathology where the muon track is split into two parts, μ_1 in cyan and μ_2 in gray. At the split point, there is a kink that changes the direction of the μ_2.

Depending on the point where the division occurred, i.e., the point in (x, y, z) where the track is split, the events were classified into three categories:

1. Cathode Crossing Splits: Events where the splitting point occurs when the tracks cross the cathode, along the x-direction (drift direction) at +210 cm and -210 cm. This is illustrated by the two peaks in the blue distribution in Fig. 3.20a.

2. Beam Direction Splits: Events where the splitting point occurs at z=0 (beam direction). This is shown in the orange distribution in Fig. 3.20b.

3. Unclassified Events: Events that do not fall into the above categories.

The focus was on studying the events that have the splitting point at $z = 0$. It was observed that these events were characterized by crossing the cathode and also crossing the contiguous TPC, thereby changing the z sign. Of the entire sample (422 of ν_μ candidates), 15 candidates satisfied this characteristic. Among them:

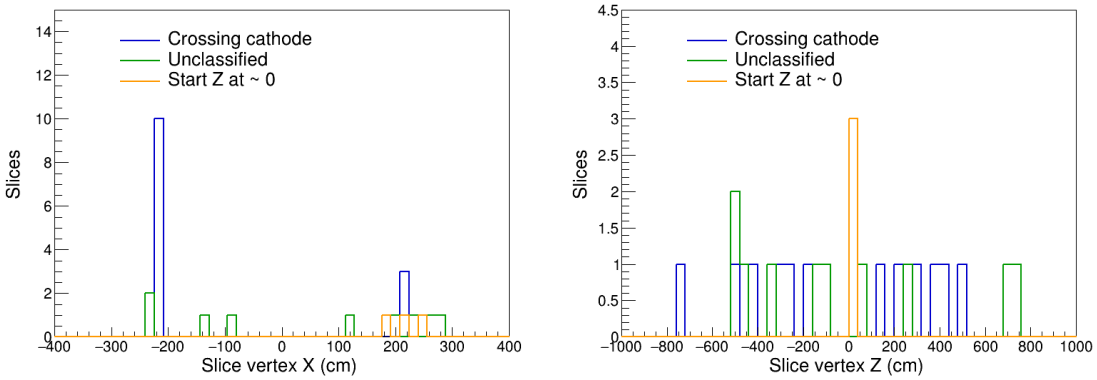

(a) X-direction (b) Z-direction

Figure 3.20: Split points along the (a) x and (b) z directions. The blue distribution corresponds to the events with the split point crossing the cathode, the orange distribution represents those with the split point around z=0, and the green distribution includes the unclassified cases.

- 9 had "good" reconstruction, meaning that the comparison of the μ track between the 3D vertex/end of the track scan positions and the 3D vertex/end of the track reconstruction positions was less than 15 cm $|\Delta_{vertex,endTrk}(\text{scan-reco})| < 15$ cm.
- 4 had the split of the track occur at $z = 0$.
- 2 had multiple splits of the track.

It was identified that events with the splitting problem exhibited a slight bend in the direction of the hits when transitioning from one TPC to the other (Fig. 3.21). There is ongoing dialogue with Pandora experts to explore a solution to this effect. This study is crucial because the identified issues contribute to the errors in the measurements being made.

Currently, it is possible to apply a selection cut that removes the events exhibiting this pathology, and efforts are being made to assign a systematic error to them.

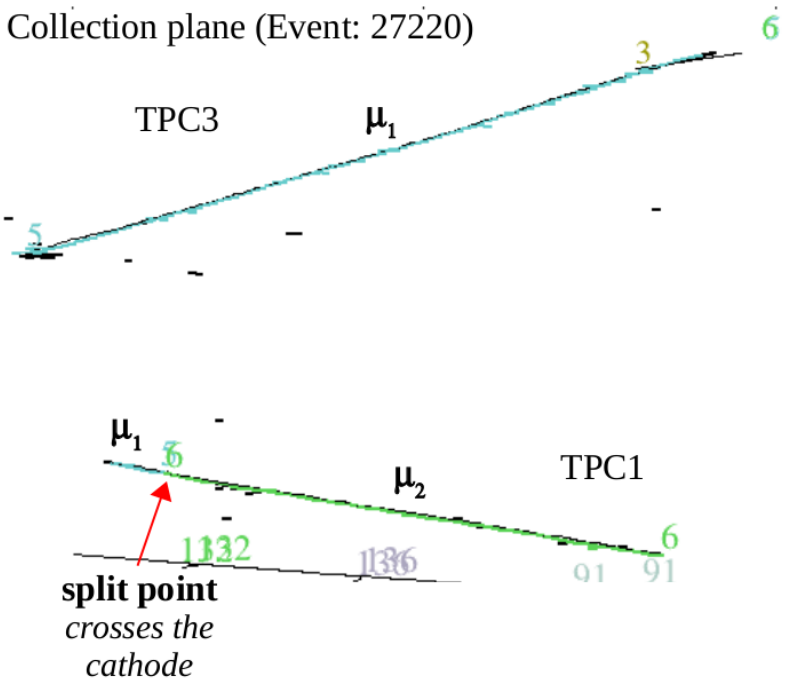

Figure 3.21: Example of the pathology where the muon track is split into two parts when it crosses the cathode, μ_1 in cyan at TPC3 and μ_2 in green at TPC1.

3.10 Summary and Future Prospects

This chapter introduced the ICARUS detector as part of the Short Baseline Neutrino (SBN) program, which aims to search for sterile neutrino signatures. ICARUS also offers diverse physical capabilities, including searches beyond the standard model and measurements of cross-sections. ICARUS is currently in its third period of physics-quality data collection.

The reconstruction of events is crucial for analyzing the physics under study, making it imperative to validate the reconstruction process. One validation method involved cross-checking the information from the visual scans of neutrino candidates with the information reconstructed of the TPCs by the Pandora software. These studies showed a good agreement between the visual scans and the reconstructed data. However, several inconsistencies (or pathologies) in the reconstruction were

also identified, which led to further research on these issues.

The study of reconstruction pathologies is ongoing and remains a significant focus for future work. In addition to the pathologies observed in muon track studies, misclassification between tracks and showers by Pandora is presented in proton track analysis. This was noted in a partial sample study, suggesting that a more complete examination could provide additional insights.

Overall, the reconstruction quality is good and is expected to contribute only a small percentage to the systematic errors in our measurements. Efforts are underway to quantify this contribution precisely and to minimize it further.

Future activities will include continued analysis of reconstruction pathologies. These improvements are essential to reduce systematic errors and enhance the reliability of the physics analyses conducted using ICARUS data.

Chapter 4

Cross-Section of NuMI neutrinos-Ar at ICARUS

Investigating their interactions with matter is central to the study of neutrino physics, typically quantified by their cross sections. Cross-sections are generally an expression of the underlying quantum mechanical probability of an interaction. In the case of neutrinos, cross-sections represent the probability of neutrinos interacting with target particles as they pass through matter [20]. Essentially, the cross-section (σ) represents the interaction rate with target particles ($Number\,of\,Events$) divided by the flux of incident particles (ϕ),

$$\sigma = \frac{Number\,of\,Events}{\phi}\,. \tag{4.1}$$

In this chapter, we will focus on this ratio, with particular emphasis on the numerator.

The accurate interpretation of neutrino oscillation experiments depends on our ability to predict and comprehend neutrino interactions with matter. Neutrino cross-sections not only determine the probability of neutrinos interacting with detector materials but also impact the observed event rates and energy spectra. A thorough understanding of neutrino cross-sections is crucial for distinguishing observed

neutrino signals from background and other systematic effects. Therefore, comprehending the neutrino cross-sections is fundamental for accurately interpreting data from neutrino oscillation experiments.

Utilizing the NuMI beam in the ICARUS experiment, we can perform precise measurements of the ν-Ar cross-section within the energy range of the DUNE experiment before it comes online. In this context, NuMI at ICARUS plays a crucial role: on the one hand, it will be able to perform measurements of the ν-Ar cross-section with high precision, in particular, we expect to have an unprecedented amount of 22.9×10^3 NuMI ν_e-argon interactions. On the other hand, the energy range of NuMI ν_μ interactions in ICARUS is in a similar energy range to that expected by DUNE, with NuMI in ICARUS being a benchmark for future DUNE measurements.

In this chapter, we will study the inclusive channel of NuMI ν_μ charged current (CC) events and establish the groundwork for measuring the ν-Ar cross-section in this channel. The study will include event selection, examination of cosmic ray background, and analysis of systematic effects, among other aspects.

4.1 NuMI Flux at ICARUS

In Chapter 3, we reviewed the Main Injector neutrino beam. In this section, we will study the flux of these neutrinos incident on the ICARUS detector. As previously mentioned, the NuMI beam is generated from collisions between protons accelerated to an energy of 120 GeV and a graphite target. These collisions initiate a particle cascade, producing particles such as pions and kaons, which decay to produce neutrinos. The electrically charged particles from this cascade are focused by magnetic horns. The focus direction depends on the electric current applied to the horns, whether in *forward horn current* (FHC) mode or *reverse horn current* (RHC) mode. Every 1.2 seconds, a 120-GeV/c proton beam is transported from the Main Injector to the NuMI target system, with a beam spill length of 9.6 μs. The highest

beam intensity recorded is 5.6×10^{13} protons on target (POT) per spill, according to Ref. [80] in Spring 2022.

The NuMI beam is directed 5.75°off the axis of the ICARUS origin. In ICARUS coordinates, the detector is situated at (315.12, 33.64, 733.63) m relative to the NuMI origin, approximately aligned with the front face of Horn 1 on the axis of the primary proton beam [64]. The composition of the NuMI neutrino flux in ICARUS is approximately 98% of $\nu_\mu + \bar{\nu}_\mu$ and 2% of $\nu_e + \bar{\nu}_e$ for energies above 250 MeV in FHC mode, as is shown in the left panel of Fig. 4.1. Similarly, in RHC mode, the flux composition is 98% of $\nu_\mu + \bar{\nu}_\mu$ and 2% of $\nu_e + \bar{\nu}_e$, as shown in the right panel of Fig. 4.1. For the subsequent analysis, data from the NuMI beam in FHC mode are utilized.

Figure 4.1 shows the simulated NuMI off-axis flux at ICARUS for various neutrino flavors in both FHC and RHC modes. These figures employ the central value flux, calculated by adjusting the hadron interactions based on experimental hadron interaction cross sections. It's worth noting that the Package to Predict the Flux (PPFX) [64] corrects neutrino flux predictions and computes systematic uncertainties associated with hadron production cross-sections, which we will explore later. For the ν_μ neutrino mode and $\bar{\nu}_\mu$ antineutrino mode, two peaks are observed: the first, at low energies (hundreds of MeV), is primarily attributed to pion decay ($\pi \rightarrow \mu + \nu_\mu$), while the second peak, around 2 GeV, is predominantly a result of kaon decay ($K \rightarrow \mu + \nu_\mu$).

4.2 The Muon Neutrino CC Inclusive Channel

Currently, we are in an era of measuring neutrino cross-sections in experiments utilizing nuclei such as iron, water, or argon as target materials. Argon (Ar), in particular, possesses heavier nuclei where nuclear effects play a crucial role in understanding neutrino-nucleus interactions. These nuclear effects include the absorption of the W

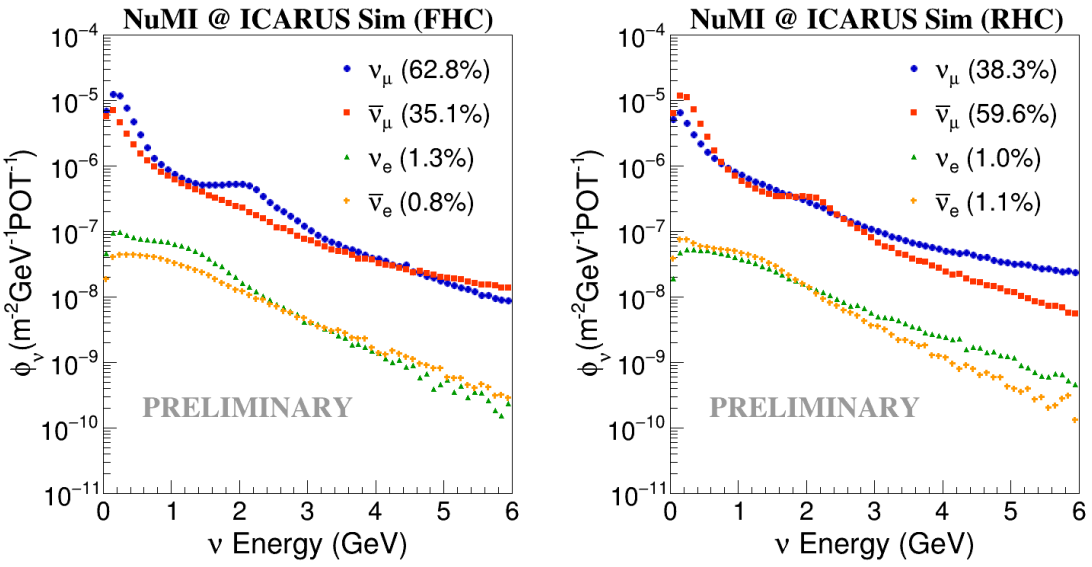

(a) Neutrino mode

(b) Antineutrino mode

Figure 4.1: Simulation of the NuMI off-axis flux at ICARUS, considering the PPFX-corrected flux with central values. In the (a) FHC mode, and (b) RHC mode. The blue circles represent the ν_μ energy spectrum, the red squares depict the $\bar{\nu}_\mu$ energy spectrum, the green triangles correspond to the ν_e energy spectrum, and the orange plus symbol denotes the $\bar{\nu}_e$ energy spectrum.

boson by a single nucleon, resulting in the so-called 1p1h excitation. Additionally, it is important to consider the coupling to nucleons within correlated pairs (referred to as short-range nucleon-nucleon correlations) and contributions from two-nucleon currents arising from meson exchange (MEC). These processes lead to the excitation of multi-nucleon or 2p2h states. The muon neutrino charged current (ν_μ CC) inclusive channel is particularly sensitive to these effects as it facilitates the measurement of the overall cross-section comprising various types of interactions, including quasi-elastic scattering (QE), resonance production (RES), deep inelastic scattering (DIS), among others, as discussed in Chapter 2. Previous experiments such as Sci-

BooNE [81], NOMAD [82], MINOS [83], MINERvA [84], T2K [85], ArgoNeuT [86], and MicroBooNE [87,88] have also measured the ν_μ charged current (CC) inclusive cross-section. The process is illustrated in the diagram presented in Fig. 4.2.

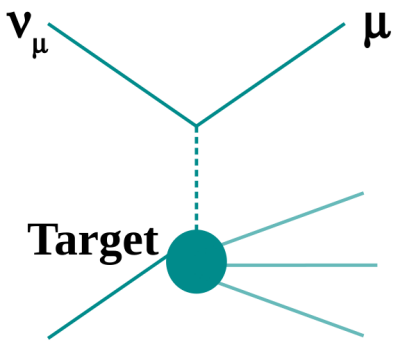

Figure 4.2: Diagram illustrating the ν_μ CC inclusive channel, where the final state consists of a μ track without imposing constraints on the hadronic system.

In addition, the ν_μ CC inclusive channel involves examining the kinematics of the final-state muon (μ) resulting from the interaction of ν_μ with the argon nuclei of the detector in ICARUS-T600. This analysis is conducted without imposing constraints on the hadronic system.

Fig. 4.3a presents the neutrino energy spectra of charged current (CC) and neutral current (NC) interactions of ν_μ and $\bar{\nu}_\mu$, resulting in muons within the predicted fiducial volume (FV). These spectra are based on approximately one year of nominal NuMI neutrino mode (forward horn current, FHC) data, equivalent to approximately 6×10^{20} POT. Table 4.1 shows the expected number of interactions in each case.

Fig. 4.3b provides a breakdown of different CC ν_μ and $\bar{\nu}_\mu$ interactions. It is evident that the predominant interaction arises from QE events, constituting 42% of the total, with a peak occurring at low energies around 500 MeV. This is followed by 32% RES interactions, peaking around 2 GeV. At higher energies, 14% is attributed to DIS interactions. Notably, the interactions attributed to MEC, comprising 11% of the total, present energy ranges similar to QE interactions, highlighting the im-

	Number Interactions per 6.0×10^{20}POT	
	Charged Current (CC)	Neutral Current (NC)
$\nu_\mu + \bar{\nu}_\mu$	378843	92444
$\nu_e + \bar{\nu}_e$	17951	4325

Table 4.1: The number of interactions per one year of nominal NuMI neutrino mode data, equivalent to approximately 6×10^{20} POT, for CC and NC interactions of ν_μ (and $\bar{\nu}_\mu$) and ν_e (and $\bar{\nu}_e$), in the predicted FV.

portance of distinguishing between these interactions.

Additionally, it is worth highlighting that the ν_μ CC energy spectrum of the NuMI beam in ICARUS is conducive to exploring interactions at neutrino energies aligning closely with the expected energy range in DUNE.

The ν_μ CC inclusive channel, besides its inherent physics implications, plays a pivotal role in developing reconstruction and selection tools in ICARUS.

Given ICARUS's shallow depth location, it is constantly bombarded by cosmic rays, constituting the primary background when searching for neutrino-induced μ tracks. The cosmic background will be further studied in the subsequent sections.

4.3 The Experimental Cross-section

As previously mentioned, significant efforts are underway to enhance our understanding of neutrino interactions with atomic nuclei in the energy range of a few GeV. This effort is crucial for maximizing the discovery potential of upcoming accelerator-based neutrino oscillation experiments, such as Hyper-Kamiokande and DUNE. Achieving control of systematic uncertainties at the percent level is essential in this context [89].

Neutrino cross-section measurements play an important role as a vital resource

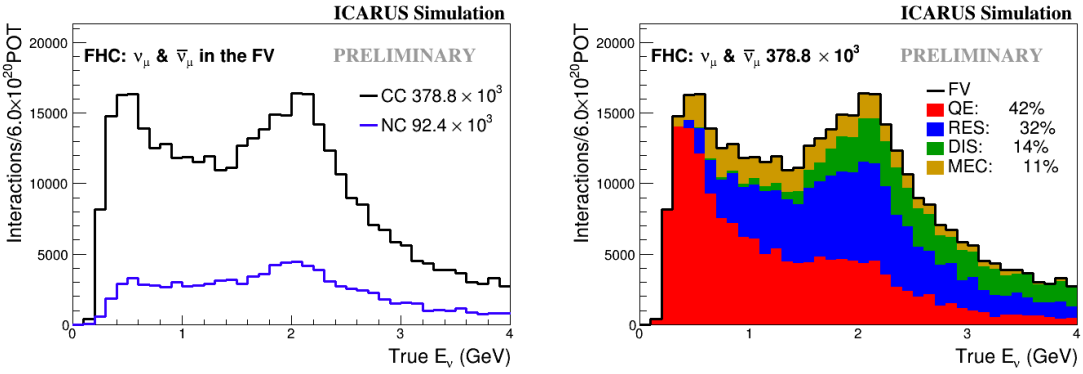

(a) $\nu_\mu + \bar{\nu}_\mu$ CC and NC

(b) $\nu_\mu + \bar{\nu}_\mu$ CC modes

Figure 4.3: Neutrino energy distributions of NuMI ν_μ and $\bar{\nu}_\mu$ obtained by Monte Carlo simulations. a) The solid black line corresponds to the CC spectra, while the solid violet line represents the NC spectra of the NuMI ν_μ and $\bar{\nu}_\mu$ interactions in the fiducial volume (FV) of the ICARUS detector. These spectra are based on 6×10^{20} POT, equivalent to approximately one year of nominal Forward Horn Current (FHC) data. b) Breakdown of different CC ν_μ and $\bar{\nu}_\mu$ interactions. The red distribution corresponds to QE interactions, the blue distribution represents RES interactions, the green one denotes DIS interactions, and the brown one indicates the MEC distribution.

for benchmarking calculations and refining nuclear theory and simulations to meet the required standards. Due to the complexity of accurately reconstructing the energy of incident neutrinos on an individual event basis and the wide spectrum of energies present in accelerator neutrino beams, contemporary neutrino scattering measurements frequently rely on flux-averaged differential cross sections,

$$\left\langle \frac{d^n\sigma}{dx} \right\rangle \equiv \frac{1}{\Phi} \int \phi(E_\nu) \frac{d^n\sigma(E_\nu)}{dx} dE_\nu \,. \tag{4.2}$$

The term $d^n\sigma(E_\nu)/dx$ denotes the energy-dependent differential cross-section, which varies with n kinematic variable(s) x of interest. On the other hand, Φ is the beam

flux integral over neutrino energy:

$$\Phi \equiv \int \phi(E_\nu) dE_\nu \,. \tag{4.3}$$

In a neutrino cross-section analysis, the process begins by determining the topology of signal events and identifying the observable(s), x, to be quantified. Criteria for event selection are established to distinguish signal events from background noise, and a binning scheme is defined to categorize the selected events. The migration of events between bins is evaluated through simulations, employing two sets of bins: true bins (representing actual observable values) and reconstructed bins (reflecting measured values). The final step in cross-section extraction involves adjusting the observed event counts in each reconstructed bin to account for background noise, detector efficiency, and bin migrations. Considering this, the differential cross-section can be written as

$$\left\langle \frac{d^n\sigma}{dx} \right\rangle_\alpha = \frac{\sum_i U_{\alpha i}(S_i - B_i)}{\Phi T \Delta x_\alpha} \,, \tag{4.4}$$

where S_i and B_i represent the total number of selected events and the number of background events, respectively in the i-th reconstructed bin. $U_{\alpha i}$ denotes the unfolding matrix, whose elements are interpreted as the conditional probability that a signal event measured within the i-th reconstructed bin belongs to the α-th true bin, considering the efficiency for signals belonging to the α-th true bin. This will be discussed in the following sections. In addition, T represents the number of targets, and Δx_α is the product of the n bin widths for the α-th true bin.

The following sections will present the study conducted to measure the numerator of the Eq. (4.4) used to calculate the cross-section of the NuMI ν_μ CC inclusive channel at ICARUS.

4.4 Monte Carlo Simulation and Data Samples

This section will examine the samples of Monte Carlo (MC) simulations and the data for selecting the signal and background events for the ν_μ CC inclusive channel.

4.4.1 Monte Carlo Simulation Samples

Monte Carlo simulations offer predictive models for various processes that generate diverse interactions within the detector. These simulations utilize probabilistic algorithms to model the behavior of particles as they propagate through the detector medium, interact with detector materials, and produce various observable signals. By simulating the entire experimental setup, including the detector geometry, material composition, and response characteristics, Monte Carlo simulations allow researchers to estimate the expected event rates, energy depositions, and particle trajectories for different types of interactions. This comprehensive approach enables the assessment of detector performance, optimization of event reconstruction algorithms, and estimation of background contributions, ultimately aiding in the interpretation of experimental data and the extraction of significant physics results.

In our case, the studied events can be classified as follows:

- ν_μ CC: Monte Carlo (MC) simulation generating particles originating from ν_μ or $\bar{\nu}_\mu$ charged current interactions, including all interaction topologies. In the NuMI ν_μ CC inclusive selection, this sample of ν_μ CC corresponds to the signal.

- ν_e CC: MC simulation originating from ν_e or $\bar{\nu}_e$ charged current interactions, including all interaction topologies. While this is part of the background for the study presented later, it is not the most predominant.

- NC: MC-generated particles from neutrino-neutral current (NC) interactions, considering all topologies. Similar to ν_e CC, NC contributes minimally to the background in the NuMI ν_μ CC inclusive selection.

- Cosmic: MC simulation cosmic ray particles produced by CORSIKA [1] [90]. This is the primary background, and a subsequent section will present a study of its impact on the NuMI ν_μ CC inclusive selection. These events will be discussed in more detail in Section 4.6 below.

Fig. 4.4a presents the event distribution of the cosine of the angle between the direction of the NuMI beam and the muon track direction ($\cos(\theta_{NuMI})$, as schematized in Fig. 4.4b) across various event types in the MC simulation samples described earlier. It is important to notice that the distribution due to cosmic ray events is predominant and presents a symmetric behavior. It clusters around zero due to the geometry of these events, primarily entering from the detector top. On the other hand, the spectrum of the ν_μ CC interaction signal predominantly clusters around $\cos(\theta_{NuMI}) = 1$, as expected, given their origin from the NuMI beam. Additionally, these distributions reveal that the contribution from other backgrounds, such as neutral currents (NC) and ν_e CC, is significantly smaller compared to the cosmic ray event background.

4.4.2 Data Samples

For collecting data samples, we used the *Majority trigger* configuration. The basis of this configuration is a hardware trigger that activates when a majority of PMT light signals coincide with the beam gate. We used two kinds of data sets (illustrated in Fig. 4.5a):

[1] CORSIKA (COsmic Ray SImulations for KAscade) is a software program designed to simulate air showers triggered by high-energy cosmic ray particles in detail.

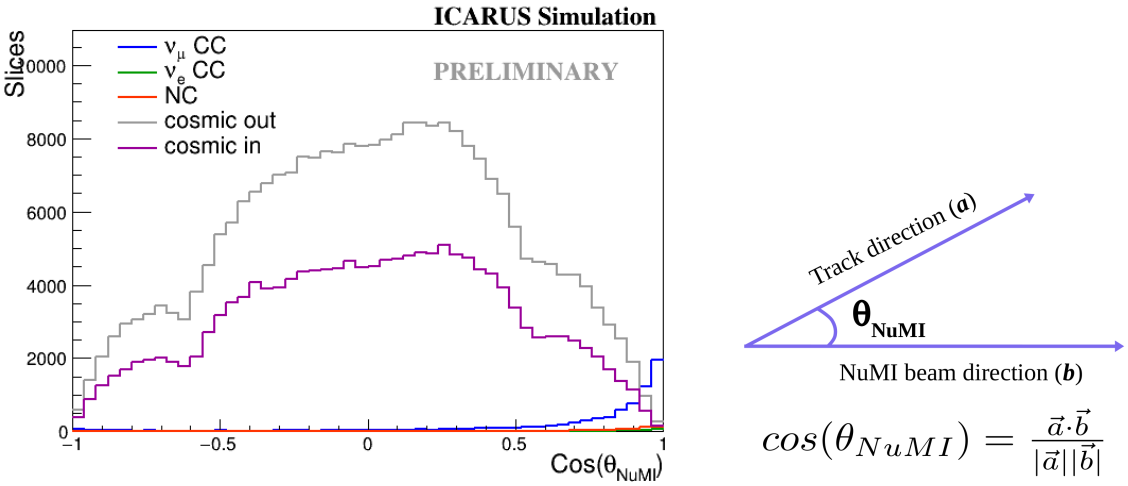

(a) (b)

Figure 4.4: (a) Spectra of the cos(θ_{NuMI}) distribution obtained from Monte Carlo (MC) simulation samples. The blue line represents the ν_μ CC signal, while the gray line depicts the cosmic ray spectrum, the orange line shows the neutral current (NC) event spectrum, and the green line corresponds to ν_e CC events. (b) The sketch illustrates the angle formed between the direction of the NuMI beam and the muon track direction, cos(θ_{NuMI}).

- On-beam data: This sample contains neutrino candidates from the beam and cosmic rays crossing during the beam spill. The activity is in coincidence with beam spill, i.e., beam physics trigger.

- Off-beam data: These are interactions collected when the beam is off, predominantly originating from cosmic production activity between spills. This sample is utilized as a control background sample, data-driven cosmic ray events.

The data sample used in this study, both on-beam and off-beam, corresponds to a partial sample from the first physical run, specifically covering runs 8505 through 8507, which is equivalent to approximately 6.6 days of data collection. Although this is a partial sample, it has been instrumental in validating several analysis tools,

such as the Barycenter Flash Matching analysis tool (which will be described in Section 4.5). Efforts are underway to apply these analysis tools to the complete sample from the first two physics-quality runs at ICARUS. It is anticipated that these tools will be fully implemented on the entire data sample in the coming months.

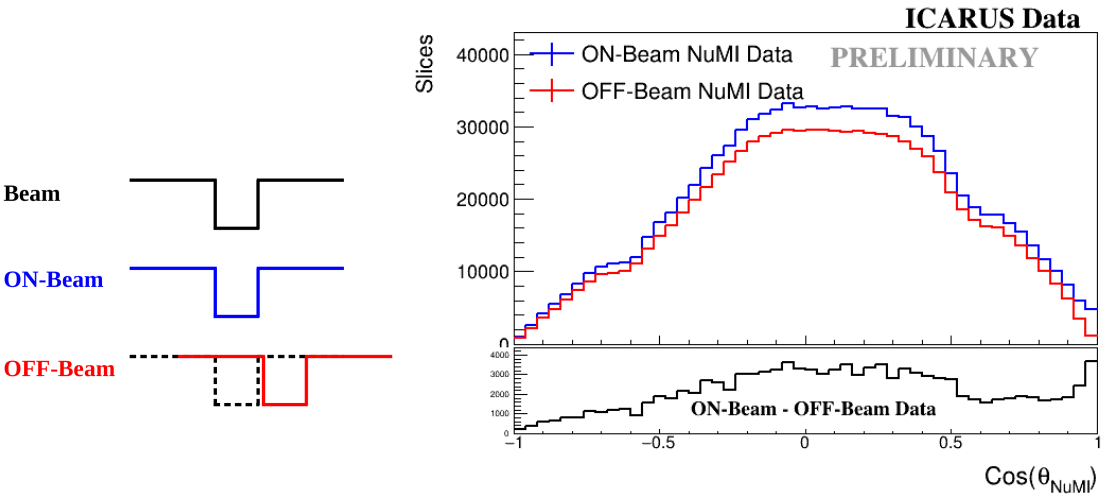

(a) (b)

Figure 4.5: (a) The sketch illustrates the data collected during the beam spill time (data on-beam) and the data collected between spills (data off-beam). In the NuMI beam, the spill time is 9.6 μs. (b) Spectra of the cos(θ_{NuMI}) distribution obtained from the data samples. The blue distribution corresponds to the spectrum of the data when is on-beam, while the red distribution represents the spectrum of the off-beam data. At the bottom of these distributions, the black spectrum corresponds to the subtraction of data on-beam from data off-beam.

Fig. 4.5b shows the distribution of the cos(θ_{NuMI}), both when the NuMI beam is on and when it is off, before applying any event selection criteria. It is noteworthy that both distributions have a similar trend, particularly around zero. This similarity arises because, at this level, cosmic ray events dominate over the neutrino interaction events. This observation becomes more evident when subtracting the distribution

corresponding to the background when the beam is off (represented by the red line) from the distribution associated with the beam being on (represented by the blue line), resulting in the black distribution below Fig. 4.5b. This resultant distribution shows the clustering of events around zero, attributable to the cosmic background as explained above, together with a peak around one indicative of the signal from ν_μ interactions.

In section 4.5, we will present a set of selection criteria to be applied to the data samples, aiming to reject background events while retaining the ν_μ CC signal events. These selection criteria were studied using MC simulation samples.

4.5 Event Selection

This section will describe the event selection criteria applied to the data samples aimed at filtering out background events while keeping a considerable number of ν_μ CC events, as these constitute the signal for studying the ν_μ CC inclusive channel. The event selection process can be categorized into a pre-selection, which aims to mitigate contamination resulting from cosmic ray events, and a selection of μ track events. These selection criteria will be presented below.

4.5.1 Pre-Selection (for Cosmic Rays Background Rejection)

As cosmic rays constitute the primary background for the ν_μ CC inclusive channel signal, a pre-selection process is implemented to minimize their presence in the data. We apply the following pre-selection criteria.

Remove everything that is Pandora clear cosmic. As explained in the previous Chapter, *PandoraCosmic* identifies primary particles of cosmic ray muon tracks using their initial and final positions, along with associated hits. In the ν_μ CC inclusive selection, interactions positively tagged by the Pandora

reconstruction algorithm as "clear cosmic" events (i.e., interactions that were positively classified by the *PandoraCosmic* reconstruction path) are rejected.

Fiducial Volume. The fiducial volume (FV), contained within the active volume (AV) of the ICARUS detector, is defined as follows: in the x-direction, parallel to the drift direction (east → west), and in the vertical y-direction (bottom → top), the FV extends 25 cm from the AV. Along the beam z-direction, it spans 30 cm upstream and 50 cm downstream from the AV, as indicated by the red dashed lines in Fig. 4.6. This FV definition is intended to minimize contamination by cosmic ray muons entering the detector, whose initial and final positions may be inaccurately determined due to space-charge effects or poor reconstruction. For this analysis, the interaction vertex must be contained within the FV, whose boundaries are:

$$-333.49 \text{ cm} < \text{x} < -86.94 \text{ cm} \quad \text{and} \quad 86.94 \text{ cm} < \text{x} < 333.49 \text{ cm}$$
$$-156.86 \text{ cm} < \text{y} < 109.96 \text{ cm}$$
$$-864.95 \text{ cm} < \text{z} < 844.95 \text{ cm}.$$

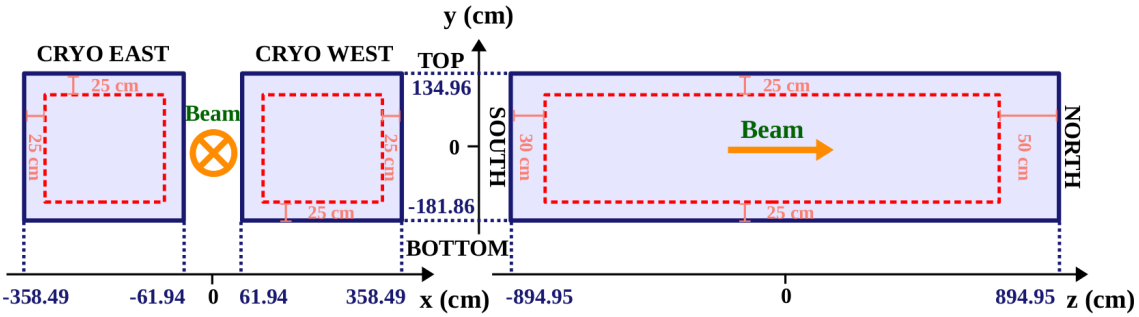

Figure 4.6: Diagram of the fiducial volume (FV) in the ICARUS detector. The red dashed lines represent the FV used for this analysis.

Longest track Y-direction (under Cosmic Ray hypothesis). Motivated by the long tracks characteristic of cosmic rays, this selection cut identifies the

relative direction of the event's longest track with respect to the Y-axis direction. This variable represents the cosine of the angle between the longest track and the Y-axis. Therefore, since the beam is perpendicular to the Y-axis direction, values around zero are expected ($\cos(\pi/2) = 0$) for neutrino events, while cosmic rays, primarily entering from the detector top, opposite to the Y-axis direction, are expected to have values around -1 ($\cos(\pi) = -1$). This situation is illustrated in Fig. 4.7a.

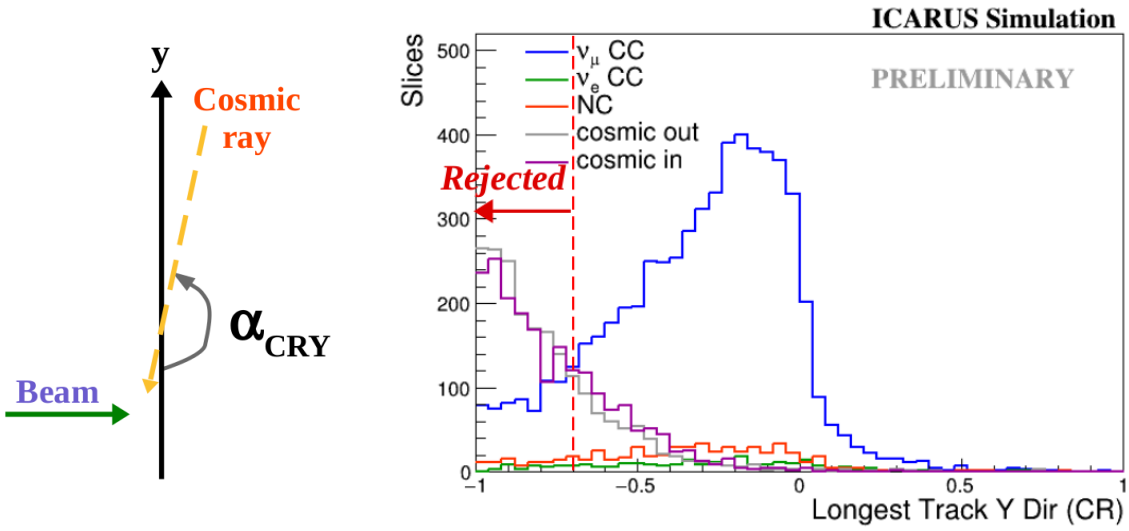

(a) (b)

Figure 4.7: (a) Illustration of the variable longest track Y-direction, represented by the cosine of the angle between a cosmic ray track and the Y-axis. (b) MC sample spectra of the variable longest track Y-direction. The gray line represents the cosmic ray distribution, the blue line corresponds to the ν_μ CC signal distribution, while the distributions for neutral currents (NC) and ν_e CC are presented in orange and green lines, respectively.

Efficiency studies performed on this variable using MC simulation samples determined that values greater than -0.7 are an appropriate cutoff to reject

the most considerable amount of cosmic rays without sacrificing too many ν_μ CC signal events. Fig. 4.7b shows the MC sample spectra of this variable, with the distribution of cosmic rays (whose main peak is around -1) shown in gray. The figure also shows the distribution of ν_μ CC signal events in blue, with a principal peak around -0.2. The distributions corresponding to neutral currents (NC) and ν_e CC are displayed in orange and green, respectively, with a low number of events and a relatively uniform distribution along the range from -1 to 0.1. The selection cut for this variable will be set at *CRLongestTrackDirY* values greater than -0.7.

Barycenter Flash Matching. This selection criterion incorporates the TPC-PMT matching tool, which is based on the charge and light barycenters. Previous studies utilized the Flash Match Score tool developed by the SBND collaboration, which matches charge flashes to scintillation photons to provide T_0 for each event and distinguish neutrino interactions from cosmic rays. Recently, ICARUS introduced the Barycenter Flash Matching tool, which aligns optical flashes (OpFlashes) with slices by minimizing the YZ distance between the weighted charge center of the slice and the weighted center of the flash. This tool also rejects out-of-time slices based on the flash timing.

Studies using hand-scanned muon tracks from BNB ν_μ CC candidates reveal that the longitudinal distance between the light and charge barycenters for the same particle is less than 1 m. Consequently, this criterion has been adopted to select ν_μ CC signals and reject cosmic ray events.

In preliminary studies, when comparing the efficiency of the barycenter flash matching tool to that of the flash match score tool, it was observed that the latter had an efficiency of 26% on signal samples. In comparison, the barycenter flash matching tool achieved an efficiency of 80% on the signal samples. This improvement in efficiency with the barycenter flash matching

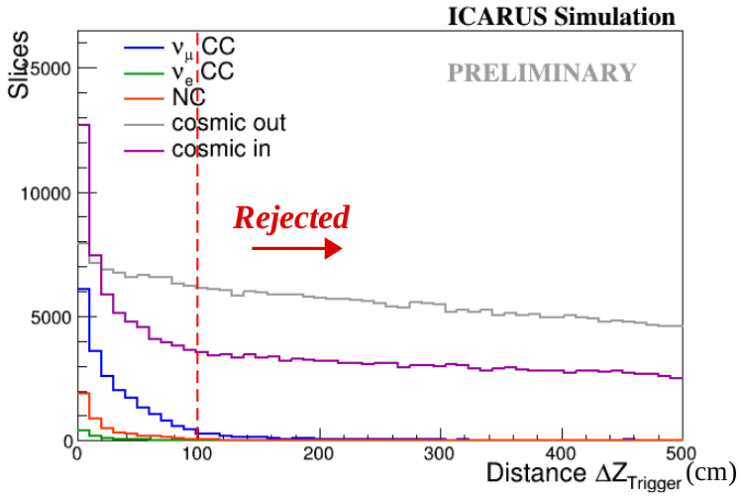

Figure 4.8: MC sample spectra of the distance between the weighted charge center of the slice and the weighted center of the flash along the Z-axis, considering the trigger. The gray line represents the cosmic ray distribution, the blue line corresponds to the ν_μ CC signal distribution, while the distributions for neutral currents (NC) and ν_e CC are shown in orange and green, respectively.

tool compared to the previous flash matching score tool is also evident in the signal and background samples purity. The barycenter flash matching tool rejects a good fraction of cosmic rays, and after the NuMI ν_μ CC inclusive selection, we get 74% of the signal and 26% of the background, compared to the 60% signal and 40% background obtained with the flash match score tool. Section 4.7 will provide further discussion on the purity and efficiency of the signal and background samples.

Figure 4.8 illustrates the spectrum of the distance between the weighted charge center of the slice and the weighted center of the flash along the Z-axis, taking the trigger into account. It is evident from this figure that values greater than 100 cm are primarily associated with cosmic ray events (gray solid line), whereas most ν_μ CC signal events (blue spectrum) exhibit values below 100 cm

for this variable. Therefore, an appropriate selection criterion for this variable is to reject values greater than 100 cm.

4.5.2 Muon Selection

The event selection process, based on reconstructed variables, seeks to refine the sample preserving as many ν_μ CC events as possible by requiring at least one muon in the final state. Selection criteria for primary muon tracks include considerations such as track length, calorimetry information, and whether the track is fully contained in the detector volume or exits the detector. These criteria will be discussed further below.

Muon track signals. The reconstructed particles within a track are examined to identify the presence of a muon in the signal. The track must originate within 10 cm of the vertex and be classified as a primary particle in the Pandora reconstructed interaction. For fully contained tracks, we require a length of more than 50 cm, with the endpoint contained within 10 cm of the outer boundaries of the active detector volume. Additionally, the track must exhibit Chi2 PID scores (in the collection plane) consistent with a muon over a proton, with a muon score of less than 30 ($\chi^2_\mu(\mu) < 30$) and a proton score greater than 60 ($\chi^2_p(\mu) > 60$). The motivation behind using these Chi2 PID score thresholds is illustrated in the distributions shown in Fig. 4.9. However, if the muon track is exiting, the Chi2 PID scores are not applicable, as the Bragg peak at the end of the muon trajectory is not observed (and the residual range as the muon escapes is unknown). The longest reconstructed track satisfying these criteria is designated as a muon candidate.

Fig. 4.10a shows the distribution of the variable $\cos(\theta_{NuMI})$ after applying the selection criteria studied in this section (*inclusive selection*). Notably, the ν_μ signal

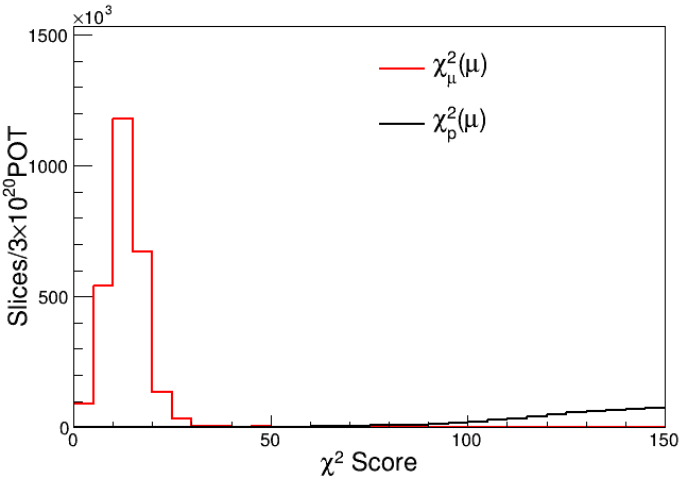

Figure 4.9: The χ^2-based Particle ID scores from the simulation are represented for reconstructed particles matched back to true stopping muons identified from truth-level data. Scores indicating muons ($\chi^2_\mu(\mu)$) are represented in red, while scores indicating protons ($\chi^2_p(\mu)$) are shown in black. These distributions serve as the basis for the score thresholds used in identifying muon candidates during the selection process.

predominates, while the contribution from backgrounds (cosmic rays, ν_e, and NC) is minimal. A similar trend, with the signal dominating over the background, is observed in the track length variable, illustrated in Fig. 4.10b. In the subsequent section, we will conduct a quantitative analysis of the efficiency and purity of both signal and background samples following the implementation of the event selection criteria discussed herein.

4.6 Cosmic Ray Background

As previously mentioned, ICARUS is a surface detector constantly bombarded by cosmic ray events. These events constitute the primary background for studying the ν_μ CC inclusive channel. In this section, we will examine the background caused

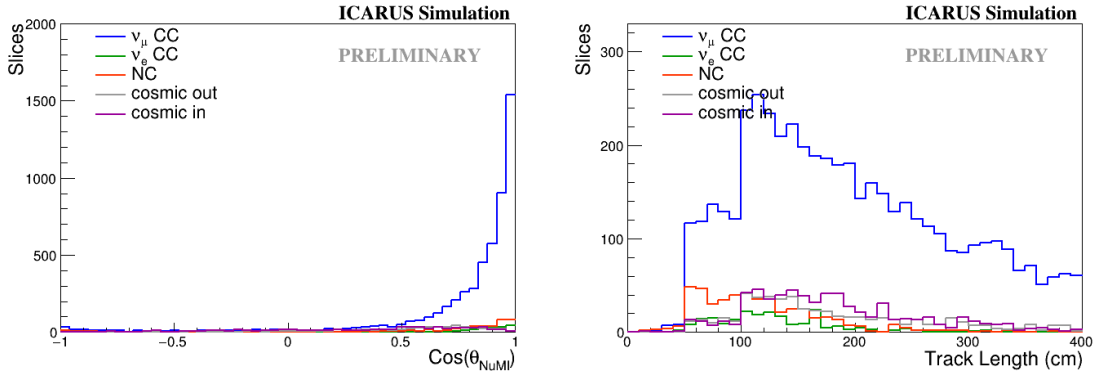

(a) (b)

Figure 4.10: Distributions of MC simulation samples after applying cuts to select ν_μ CC inclusive channel events for the variables (a) $\cos(\theta_{NuMI})$ and (b) track length. The ν_μ CC signal events are shown in blue, while the cosmic ray distribution is represented in gray. The orange line corresponds to neutral currents (NC), and the green line represents ν_e CC events. It is important to emphasize that after applying the selection cuts, the signal contribution surpasses that of the different backgrounds.

by these cosmic rays, focusing particularly on the stopping muon sample, as these events can closely mimic the signal events from ν_μ CC interactions.

More information on the production of cosmic rays reaching the ICARUS detector can be found in Appendix B, along with details about the specialized cosmic ray simulation software, CORSIKA, which is used in ICARUS and other experiments [86] to produce their MC simulation cosmic ray samples.

4.6.1 Cosmic Ray Samples

Cosmic Ray MC Simulation

MC simulation samples of cosmic ray interactions are crucial for distinguishing between genuine signal events and background events induced by cosmic rays. To accurately model these backgrounds, experiments such as ICARUS use the specialized cosmic ray simulation software CORSIKA (COsmic Ray SImulations for KAscade) [90, 91]. CORSIKA simulates the extensive air showers created when high-energy cosmic rays interact with the Earth's atmosphere, producing secondary particles that reach the detector.

The simulation starts with primary cosmic rays, such as protons, light nuclei, or photons. These primary particles interact with atmospheric nuclei, generating secondary particles in a cascading process. The simulation traces these secondary particles to the detector level, modeling their interactions and energy losses along the way. This includes simulating the response of the detector to these particles, such as producing signals in various detector components (e.g., TPC, PMT, CRT).

Two types of cosmic ray MC simulation samples are available in ICARUS: in-time cosmics and out-of-time cosmics. These are illustrated in Fig. 4.11 and will be described below.

In-time cosmics. Refers to cosmic ray events that occur during the data acquisition window, i.e., within the same time period as the beam spill. These events can directly interfere with the detection of genuine neutrino interactions, as they are recorded along with the desired signal. Cosmic-in-time events are particularly challenging because they temporally overlap with the signal, making it difficult to distinguish between the signal and the background based on time alone.

Out-of-time cosmics. These are cosmic ray events that occur outside the data ac-

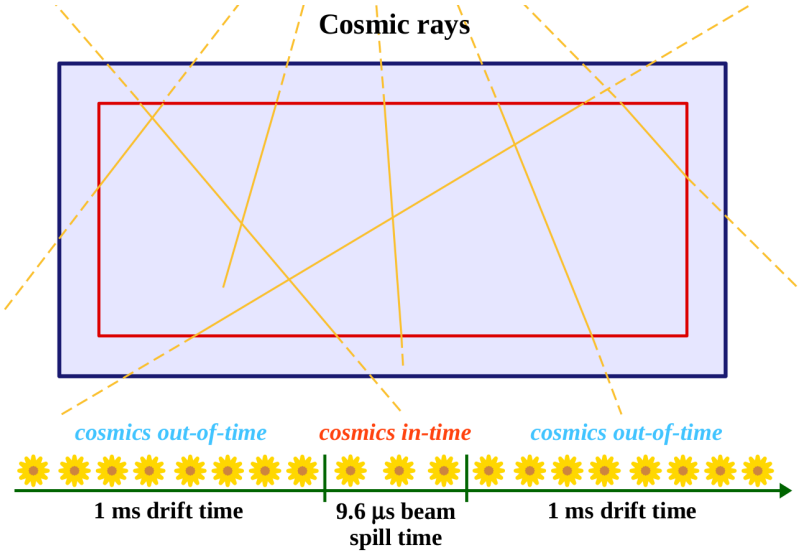

Figure 4.11: Illustration of the cosmic ray MC simulation samples, in-time and out-of-time, available in ICARUS. See text for further details.

quisition window. These events happen before or after the period in which the detector actively records beam-spill data. Although they do not directly overlap with the signal temporally, they can still affect the data if their remnants or delayed signals are recorded.

Cosmic ray data

In the context of data samples corresponding to the background, specifically Off-beam data, there are two configurations: the Majority trigger and the Minimum Bias trigger, described as follows:

Majority Trigger. This is a hardware trigger based on a majority of PMT light signals coinciding with the beam gate. The *OffBeamNUMIMAJORITY* configuration refers to off-beam (cosmic) events that are majority-triggered, ideally capturing events with in-time cosmic activity. These events are crucial for understanding and modeling cosmic ray backgrounds that coincide with the

beam spill, providing a realistic background sample.

Minimum Bias. This configuration collects events coinciding with the beam spills but does not require the PMT light signal condition. The *OffBeamNUMIMINBIAS* configuration refers to off-beam (cosmic) events that are minimum bias, meaning these events may or may not have in-time cosmic activity ("unbiased"). This allows for collecting a more diverse set of background events, which can be helpful for various studies.

Fig. 4.12 shows the distribution of muon track lengths for both off-beam data sample configurations. A reasonable agreement between the two configurations is observed.

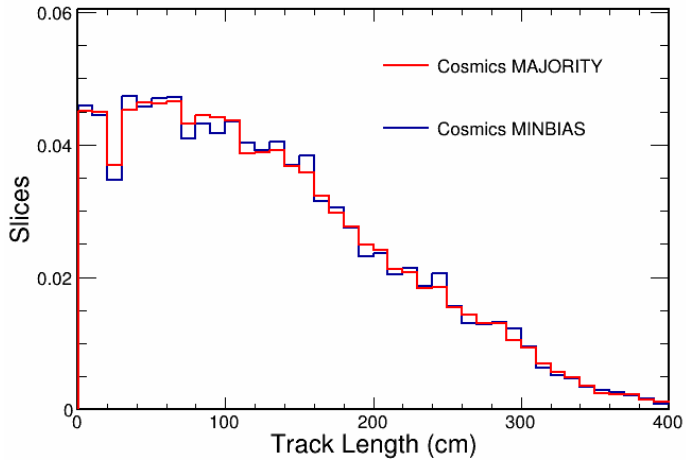

Figure 4.12: Distribution of the muon track length using both off-beam data samples, majority trigger and minimum bias, available in ICARUS. Both distributions are area normalized and have the fiducial volume cut applied.

For the studies presented below, the Majority Trigger configuration is used. The off-beam data majority trigger sample will be utilized as the in-time cosmic ray sample in subsequent analyses. This approach ensures that the background model

closely matches the conditions under which the genuine signal events are detected, thereby improving the accuracy of background rejection algorithms and overall analysis reliability.

4.6.2 Stopping muons

Stopping muons travel through a medium and lose energy until they decay. These events lose energy primarily through ionization and radiative processes as they pass through matter. The rate of energy loss depends on the material through which they travel and their initial energy [92].

When a muon decays in a material, it typically decays into an electron, an electron neutrino, and a muon neutrino. This decay process is a characteristic signature used to identify stopping muons in detectors.

Stopping muons pose a significant challenge as they can mimic a ν_μ CC neutrino interaction originating within the detector. These muons are identified if a Michel electron [93] or a Bragg peak [92] is detected in the track's energy loss profile or if the pattern of multiple Coulomb scattering (MCS) [94] suggests a direction consistent with an entering and stopping particle.

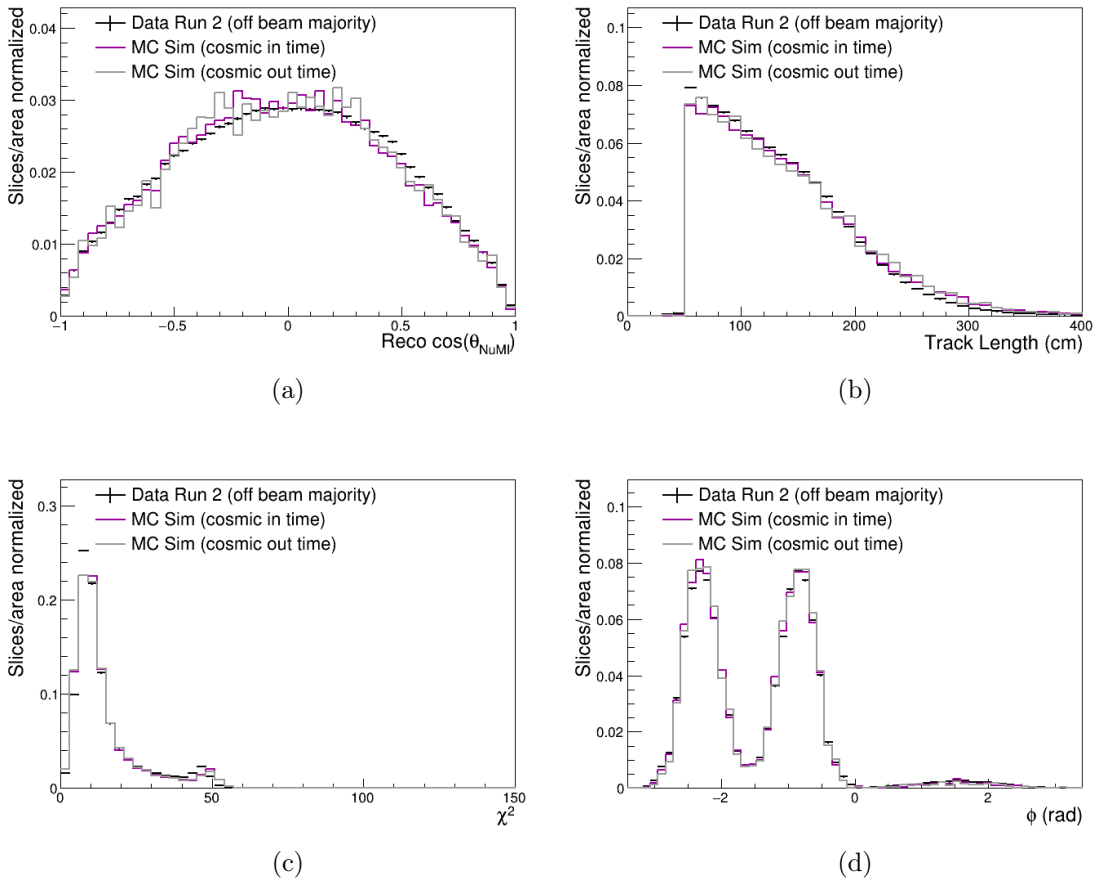

Figure 4.13: Distributions of reconstructed information for the selected stopping muon events for variables (a) $\cos(\theta_{NuMI})$, (b) muon track length, (c) χ^2 score, and (d) ϕ angle. The black crosses represent the data distribution, the purple line corresponds to the in-time cosmic MC simulation, and the gray line represents the out-of-time cosmic MC simulation. All distributions are area normalized.

A control sample with stopping muons has been developed to ensure that the propagation of cosmic muons through the detector is accurately modeled. These muons must be reconstructed as fully contained events. Figs. 4.13a and 4.13b show the variables of $\cos(\theta_{NuMI})$ and track length for the selected stopping muon events in both data and simulation, demonstrating good agreement between data and MC

simulation. This control sample will be used as a direct constraint in the inclusive selection study.

Similarly, Figs. 4.13c and 4.13d show good agreement between the MC simulation and data samples for the variables χ^2 score (indicating tracks consistent with being muon-like) and ϕ angle (the angle of the initial track direction in the x-y plane), respectively.

4.7 Efficiency and purity of signal and background samples

The performances of the event selection discussed in the preceding section are quantified in terms of efficiency represented by

$$Efficiency = \frac{selected\ signal}{all\ signal}\,, \tag{4.5}$$

where the *selected signal* in the numerator represents events after applying selection cuts, while the *all signal* in the denominator represents events without any selection cuts.

On the other hand, the purity of the sample is defined as

$$Purity = \frac{selected\ signal}{selected\ signal\ +\ background} \tag{4.6}$$

where the numerator represents the selected events after applying the selection cuts, while the denominator includes both these selected events and the background events that also passed the selection cuts.

Fig. 4.14a shows the distribution of the variable $\cos(\theta_{NuMI})$ for the ν_μ CC signal, considering the true values of the MC simulation sample under study. The pink distribution represents the ν_μ CC signal before applying any selection cuts, while the

blue distribution represents the same variable after applying the inclusive selection cuts (that is, the event selection criteria discussed in the previous section).

In contrast, Fig. 4.14b illustrates the efficiency distribution of the $\cos(\theta_{NuMI})$ variable for the ν_μ CC signal, considering the true values of the MC simulation sample shown in Fig. 4.14a. Here, it can be seen that qualitatively, the average efficiency after applying the inclusive selection criteria is 20%. While for values close to one, the $\cos(\theta_{NuMI})$ efficiency is approximately 26%, the efficiency for $\cos(\theta_{NuMI})$ values less than 0.5 appears to be around 14%.

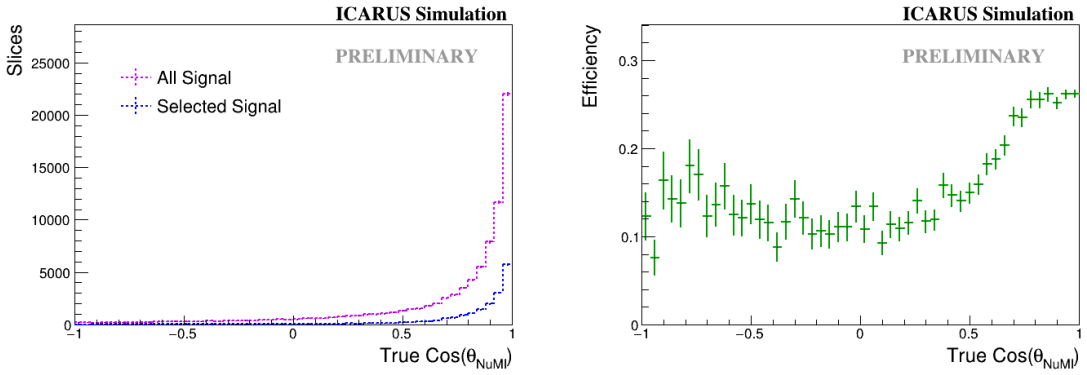

(a) (b)

Figure 4.14: (a) Distribution of the $\cos(\theta_{NuMI})$ variable with true values of the MC sample of the ν_μ CC signal. The pink spectrum has no selection cut, while the blue distribution corresponds to the spectrum applying the inclusive selection. (b) The efficiency of the inclusive ν_μ CC selection, Eq. (4.5), applied to the variable $\cos(\theta_{NuMI})$, showing an average efficiency of 20%.

Table 4.2 presents the number of slices from various MC simulation samples (including the ν_μ CC signal, background from NC, ν_e CC, and cosmic rays) after sequentially applying each selection cut: fiducial volume, Pandora clear cosmic rejection, primary muon track selection, longest track Y-direction (under Cosmic Ray hypothesis), and the barycenter flash matching cut. The efficiency of each sample

after applying these cuts is provided in parentheses. The last two columns contain the purity of both signal and background samples after applying each of the selection cuts.

	Number of Slices			Purity	
Cuts	ν_μ CC (eff)	ν_e + NC (eff)	Cosmics (eff)	Signal	Bkgd
NO CUT	27079.0 (1.00)	7157.0 (1.00)	2176712 (1.00)	0.01	0.99
Fid	12685.0 (0.47)	4054.0 (0.57)	665721 (0.31)	0.02	0.98
+Clc	12229.0 (0.45)	4016.0 (0.56)	129495 (0.06)	0.08	0.92
+Trk	7549.0 (0.28)	1045.0 (0.15)	61775 (0.03)	0.11	0.89
+Lty	6712.0 (0.25)	879.0 (0.12)	16068 (0.01)	0.28	0.72
All	5402.0 (0.20)	703.0 (0.10)	1218 (0.001)	0.74	0.26

Table 4.2: The first column of this table shows the sequence of cuts applied to the MC simulation samples. These cuts are applied consecutively, with each subsequent cut building upon the results of the previous ones. **Fid** represents the cut for the *Fiducial Volume*, **Clc** denotes the removal of *Pandora clear cosmic* events, **Trk** indicates the selection for *muon track signals*, **Lty** signifies the *longest track Y-direction cut (under Cosmic Ray hypothesis)*, and **All** are all previously mentioned cuts plus the *Barycenter Flash Matching*. The second column corresponds to the ν_μ CC signal, while the third and fourth columns represent the backgrounds due to ν_e+NC and cosmic rays, respectively. The efficiencies of each sample, obtained using Eq. (4.5), are provided in brackets. The last two columns denote the purity of the samples, with the fifth column indicating the purity of the ν_μ CC signal sample and the sixth column representing the purity of the background sample (encompassing ν_e, NC, and cosmic rays).

Based on the efficiency and purity results described by Eqs. (4.5) and (4.6), obtained from the MC simulation samples presented in Table 4.2, it can be seen that,

upon applying all-inclusive selection cuts, the efficiency of the ν_μ CC signal is 20%. Additionally, as anticipated in the previous section, the purity of the sample indicates that the signal exhibits a purity of 74%, while the total background accounts for 26%. Within this background, 16% is attributed to cosmic rays, while the remaining 10% is associated with background from ν_e CC and neutral current (NC) interactions. Currently, efforts are ongoing to enhance the selection efficiency by exploring other tools available in ICARUS, such as the implementation of CRT-PMT matching, which will be discussed later in section 4.11.

4.8 Results of inclusive selection in data and MC simulation

In previous sections, the inclusive selection criteria for identifying ν_μ CC events were studied. These criteria were developed to maximize the signal purity while effectively suppressing background events, particularly those originating from cosmic rays.

This section will focus on applying these selection criteria to the actual data collected by the ICARUS detector. In addition, the variables of interest, such as the $\cos(\theta_{NuMI})$ and the track length, will be shown to illustrate the level of agreement between the observed data and the expected outcomes based on MC simulations.

Fig. 4.15 shows the spectra corresponding to the $\cos(\theta_{NuMI})$ variable for the on-beam (blue line) and off-beam (red line) data samples after applying the inclusive selection criteria studied in Section 4.5. In the same figure, the spectrum resulting from subtracting the off-beam sample from the on-beam sample is shown at the bottom. In this subtracted spectrum, it can be seen that the contribution from the cosmic ray background has significantly decreased, making the signal contribution (that has values close to one) more visible.

This example demonstrates that the inclusive selection effectively removes a sig-

nificant amount of the cosmic ray background. As shown in Fig. 4.15, compared to Fig. 4.5b where no selection cuts were applied, the bunch of events at zero $\cos(\theta_{NuMI})$ disappeared, indicating that cosmic ray removal was effective.

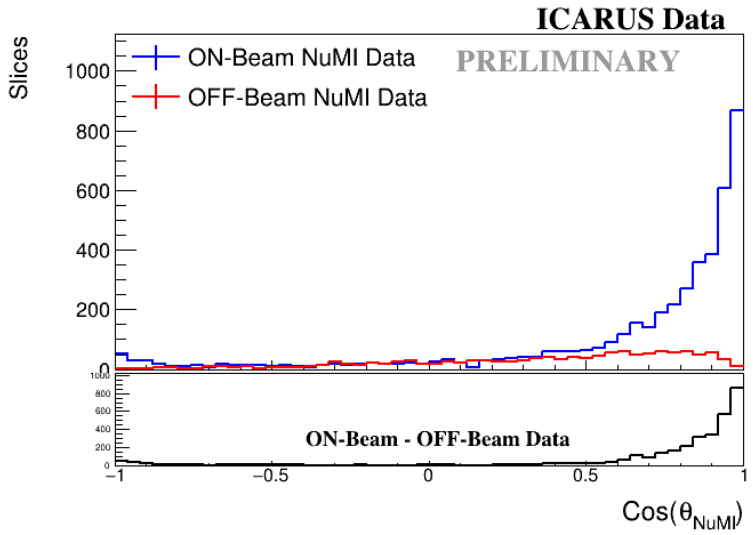

Figure 4.15: Spectra of the $\cos(\theta_{NuMI})$ distribution obtained from the data samples after applying the inclusive selection criteria. The blue distribution corresponds to the on-beam data spectrum, while the red distribution represents the off-beam data spectrum. At the bottom of these distributions, the black spectrum corresponds to the result of subtracting the off-beam data from the on-beam data.

Next, we will compare the MC simulation samples and the data samples. This comparison is expected to show the agreement between the MC simulation model and the actual data collected. These comparisons are crucial for validating the accuracy of the simulation and ensuring it accurately represents the actual behavior observed in the detector.

4.8.1 Data vs MC simulation comparisons

It is essential to compare the simulation results with actual data collected by the detector to validate the accuracy of the MC simulations and ensure the reliability of the analysis. This comparison verifies that the MC models accurately represent the physical processes occurring within the detector and can reliably reproduce observed phenomena.

This section will present comparisons between the data samples and the corresponding MC simulation samples. Different variables, such as $\cos(\theta_{NuMI})$ and the length of the track, will be studied, highlighting the level of agreement between the simulated and real data. This process not only helps in fine-tuning the simulation parameters but also enhances confidence in the event selection criteria and background rejection techniques.

Fig. 4.16 shows the distribution of the $\cos(\theta_{NuMI})$ variable. It compares the on-beam sample (black distribution) with the off-beam sample plus the MC simulation (red distribution). In this way, we are using in the red distribution the off-beam sample as an in-time cosmic sample. It is worth mentioning that both distributions are area-normalized. In general, there is a good agreement between the on-beam data and the MC simulation (plus the off-beam data) samples. Overall, their ratio is around 1 (as shown by the blue distribution at the bottom of the figure).

Although there is a good agreement, in general, between the on-beam data and the MC simulation (plus the off-beam data) samples, it is important to note that some inconsistencies are still under study, such as the small peak observed at values around -1 in the on-beam data sample, which could indicate neutrino candidates moving backward to the beam direction. Reconstruction studies, such as those mentioned in Chapter 3, suggest that the issue could be due to split tracks where some segments have an opposite direction. Another possibility is a misidentification of the interaction vertex, where the vertex is incorrectly identified at the end of the

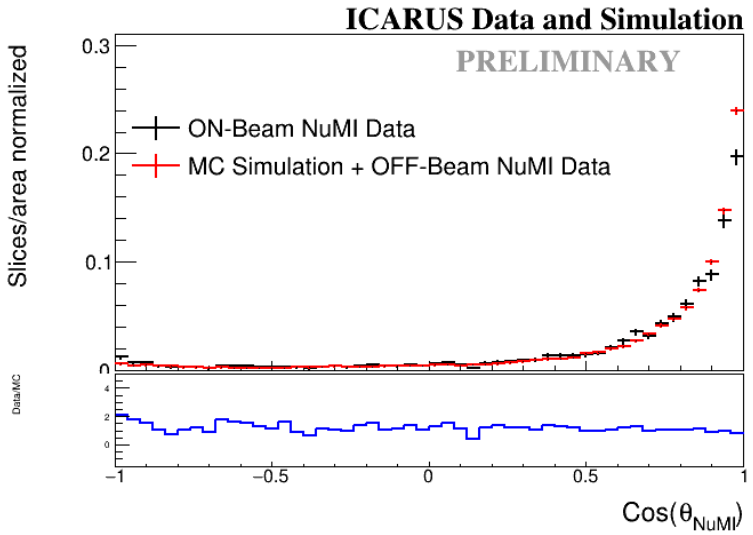

Figure 4.16: Spectra of the $\cos(\theta_{NuMI})$ distribution obtained from the on-beam data and MC simulation plus the off-beam data samples after applying the inclusive selection criteria. The black distribution corresponds to the on-beam data spectrum, while the red distribution represents the MC simulation in addition to the off-beam data spectrum. At the bottom of these distributions, the blue spectrum shows the ratio between the on-beam data and the MC simulation (plus the off-beam data) samples drawn above.

track. As mentioned previously, these pathologies are currently under investigation.

4.9 Unfolding matrix

As discussed in Section 4.3 (see Eq. (4.4)), the unfolding matrix $U_{\alpha i}$ is a mathematical tool that corrects for detector resolution effects and biases in measured event distributions. The unfolding matrix represents the conditional probability that a signal event measured within the i-th reconstructed bin also belongs to the α-th true bin ($P_{\alpha i}$), divided by the efficiency (ϵ) for signal events belonging to the α-th true bin [89] [95]:

$$U_{\alpha i} = \frac{P_{\alpha i}}{\epsilon_\alpha} \,. \tag{4.7}$$

Detectors do not measure true values directly but instead provide a smeared representation due to factors such as energy resolution, detector efficiency, and angular resolution. Fig. 4.17 illustrates this smearing effect.

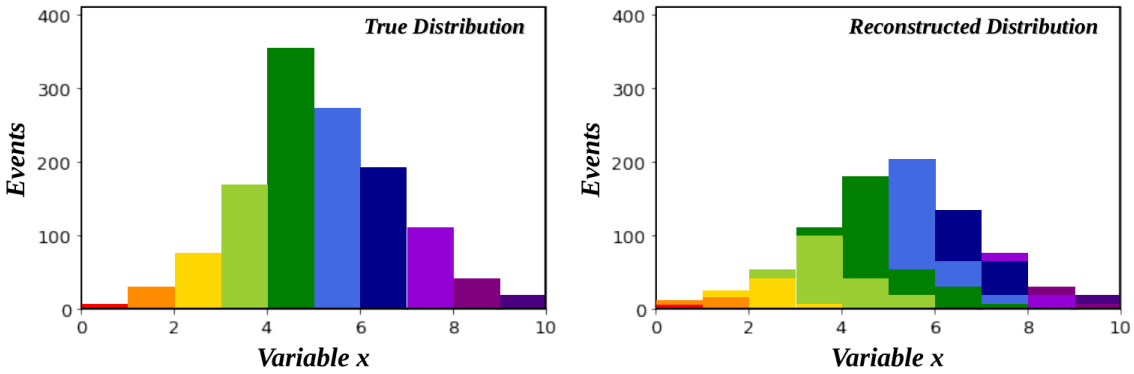

Figure 4.17: Illustration of the true distribution of events (left panel) for a variable x and the reconstructed distribution of events (right panel) for the same variable x. The key point to note is that the reconstructed distribution exhibits a smearing of events across different bins around their true values.

Before applying the unfolding matrix to experimental data, it is validated using MC simulation samples where the true distributions are known. This validation ensures that the unfolding procedure accurately recovers the true distribution and properly accounts for detector effects.

Fig. 4.18a shows the signal ν_μ CC distributions of the variable $\cos(\theta_{NuMI})$ after applying the inclusive selection for both the true information and the reconstructed information in the MC simulation sample. It can be observed that there is consistency between both distributions. This agreement in particular can be appreciated in Fig. 4.18b, which provides a close-up view of values between 0.5 and 1 in 2D, comparing the true distribution with the reconstructed distribution of this variable.

In this kind of 2D plot, the points along the diagonal indicate a strong correlation between the histograms that we are comparing, in this case, the true and reconstructed values of the $\cos(\theta_{NuMI})$. If the points lie exactly on the diagonal, it means that each reconstructed value matches the true value, indicating no smearing or distortion. Contributions in bins off the diagonal represent smearing effects where events from one true bin are reconstructed into neighboring bins. This is common due to detector resolution limits, noise, or imperfect reconstruction algorithms.

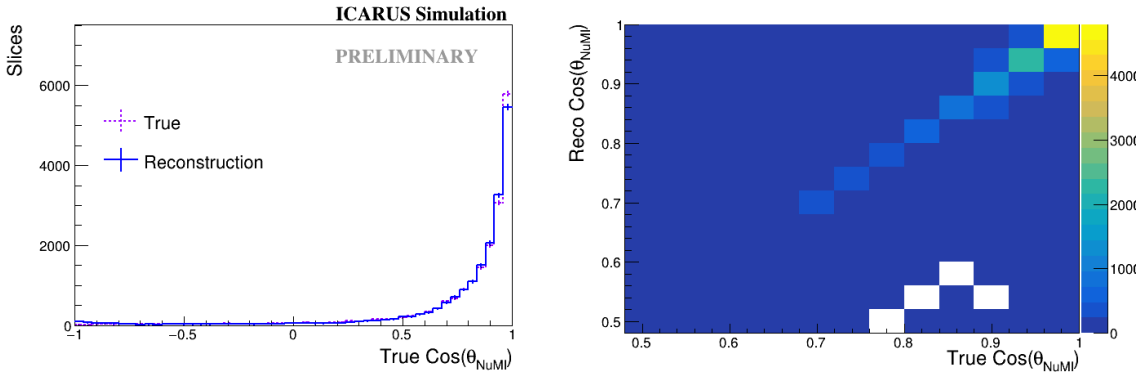

(a) (b)

Figure 4.18: (a) Distributions of the ν_μ CC signal for the $\cos(\theta_{NuMI})$ variable after applying the inclusive selection. The blue solid line represents the reconstructed spectrum, while the pink dashed line shows the true spectrum. (b) 2D comparison of the true and reconstructed distributions of the $\cos(\theta_{NuMI})$ variable, zoomed in on values from 0.5 to 1.

Fig. 4.19 shows a preliminary result of the 2D comparison of the histograms of the ν_μ CC signal for the $\cos(\theta_{NuMI})$ variable using true and reconstructed information from the MC simulation under study after applying the inclusive selection. The histograms are normalized by columns (i.e., by true bin), and the fraction of events in each reconstructed bin for that true bin is indicated.

Ideally, in the plot of Fig. 4.19, each bin on the diagonal should show 100%.

However, as discussed earlier, there is smearing in the reconstructed distribution into neighboring bins. As a result, while the majority percentage remains on the diagonal, there is also a contribution in the bins adjacent to the diagonal. Additionally, although to a lesser extent, there is some contribution from smearing in bins further away from the diagonal. The following steps for this work are part of the future perspectives, where a study of the binning will be conducted. Specifically, the bin width will be analyzed to determine if the agreement can be improved. Additionally, it is planned to extend this study to more variables, such as muon momentum. We will discuss this and other prospects in Section 4.11.

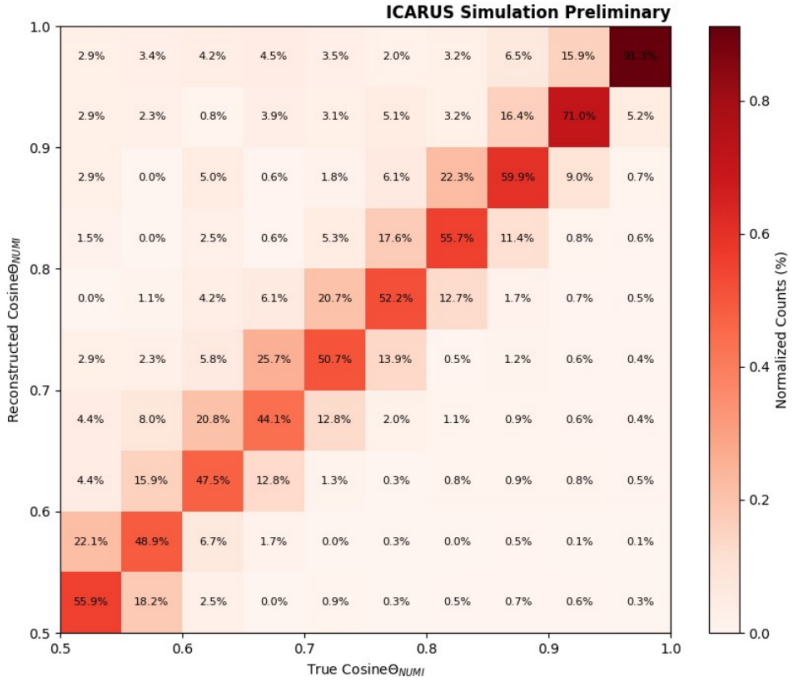

Figure 4.19: Reconstructed vs. true $\cos(\theta_{NuMI})$ for inclusive ν_μ CC signals. The histograms are normalized by columns (i.e., by true bin). The fraction of events appearing in each reconstructed bin for that true bin is indicated, in percentage, within each bin.

4.10 Systematic Uncertainties

Systematic uncertainties arise from various sources, including the physics modeling of neutrino interactions, the detector's response to these interactions, and uncertainties in the neutrino flux. This section describes the systematic uncertainties considered in the cross-section measurement of the ν_μ CC inclusive channel. In particular, it focuses on the uncertainties related to the flux and the physics modeling of neutrino interactions. It should be noted that the study of detector systematic uncertainties is still ongoing and is being conducted by another group within the ICARUS collaboration.

As mentioned above, the measurement of the cross-section is affected by three main categories of systematic uncertainties:

Beam Flux. These uncertainties stem from predicting the neutrino flux, which is crucial for calculating the cross-section accurately. Any variation in the beam flux directly affects the measurement's precision.

Cross-Section Modeling. These uncertainties arise from the parameters used in our neutrino event generator, GENIE [96]. The way we model neutrino interactions can introduce variations that impact our cross-section calculations.

Detector Effects. These uncertainties involve how well we model the detector's response. They primarily influence the reconstructed quantities, affecting the predicted rates of background events and the efficiency of detecting the signal.

Both statistical and systematic uncertainties are represented in the covariance matrix, E [97]. The total error matrix combines these uncertainties and is expressed as

$$E = \sqrt{E_{stat}^2 + E_{syst}^2}\,, \tag{4.8}$$

where E_{stat} represents the statistical errors (which are uncorrelated and form a diagonal matrix), and E_{syst} represents the systematic uncertainties. The total systematic covariance matrix, E_{syst}, is composed of independent matrices for each category of systematic uncertainties, $E^2_{flux} + E^2_{xsec} + E^2_{detector}$:

$$E^2_{syst} = E^2_{flux} + E^2_{xsec} + E^2_{detector}\,. \tag{4.9}$$

These systematic uncertainties will be discussed below.

4.10.1 Beam Flux

The Package to Predict the Flux (PPFX), previously utilized in the MINERvA and NOvA experiments, is also employed in NuMI at ICARUS to establish the nominal flux expectation and to characterize flux uncertainties. PPFX employs a multiverse approach, where flux uncertainties are assessed through a series of multiple variations, or "universes." These uncertainties can be represented either as a covariance matrix or as binned weights derived from a Principal Component Analysis (PCA) of the covariance matrix. The detailed work conducted by the ICARUS team is documented in a technical note [64].

The output from the PPFX study is provided in a ROOT file containing various products, including covariance matrices for different uncertainties, both separately and combined. Specifically, it includes matrices for hadron production and beam-focusing uncertainties. Fig. 4.20 illustrates the covariance matrix for hadron interaction uncertainties as detailed in [64].

4.10.2 Cross-Section Modeling

GENIE provides a built-in framework for event re-weighting to evaluate systematic uncertainties in an analysis. The *GENIE-Reweight* tool assigns weights to each event based on its cross-section. Recognizing that the predictions from the GENIE base

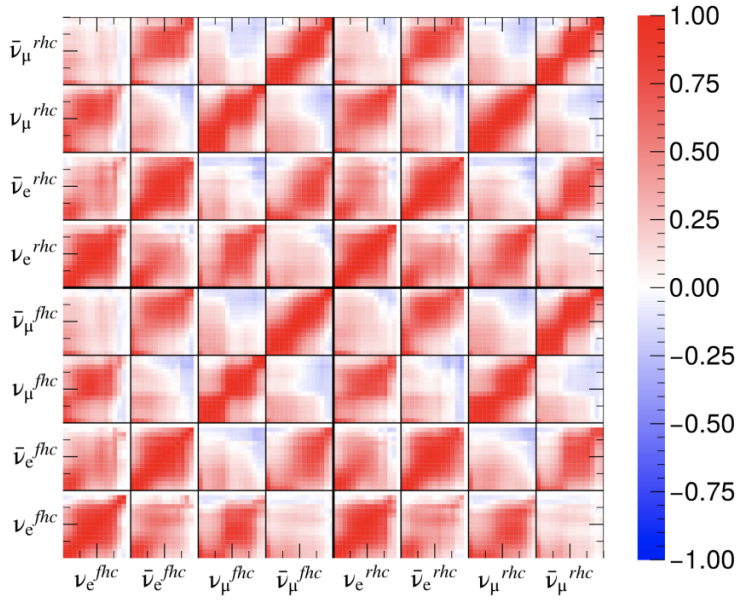

Figure 4.20: Hadron interaction covariance matrix from PPFX, developed by the NuMI at ICARUS flux team [64].

model will inevitably contain inaccuracies, we use weights to vary the cross-section model behind the simulations without the need for regeneration.

Each *dial* represents a different parameter or set of parameters within the generator that can alter the cross-section. By adjusting these dials up or down using weights, it is possible to observe the extent to which these parameters affect MC predictions, specifically noting changes in the histogram bins.

For parameters assumed to be uncorrelated with others, *multsigma* weights are used. These weights allow independent adjustment of each dial, enabling the assessment of changes in the model predictions. For each event, weights corresponding to $\pm1\sigma$, $\pm2\sigma$, and $\pm3\sigma$ variations are saved.

For groups of interdependent parameters, the *multism* approach is utilized. To evaluate the impact of these variations comprehensively, a brute-force method is employed, saving event weights across multiple (100 in the actual analysis) different "universes," each with the dials set to various positions. The spread of predictions

across these universes is then used to characterize the impact on the overall prediction.

4.10.3 Detector Effects

As mentioned above, the effects of the detector on the ICARUS analysis are currently being studied. A preliminary review can be found in the corresponding Technical Note [98].

Systematic uncertainties have been developed in the detector model to explain the reconstruction results. The energy scales for the calorimetric and multiple Coulomb scattering measurements have been specifically calibrated in ICARUS. Additionally, uncertainties arising from variations in the magnitude of field distortions due to space charge effects are considered. All these variations are included in the nominal simulation of the ICARUS detector. However, as discussed in Chapter 3, there are two regions in the detector that cause the tracks to split, and these have not yet been incorporated into the nominal simulation of the ICARUS detector.

The investigation into various sources of variation in the ICARUS detector that could impact the analysis of the ν_μ CC inclusive channel cross-section is still ongoing. This study is a prospect to be undertaken soon.

4.10.4 Preliminary Results

Although the effects of the detector on the analysis of the NuMI ν_μ CC inclusive channel have yet to be thoroughly studied, preliminary investigations into the contributions of uncertainties due to flux and cross-section modeling have been conducted.

Figs. 4.21a, 4.21b, and 4.21c provide an initial look at these contributions for the variables ϕ angle, track length, and $\cos(\theta_{NuMI})$, respectively. In the $\cos(\theta_{NuMI})$ distribution, it can be observed that around a value of one, the dominant source of uncertainty in the measurement arises from systematic effects rather than statistical

errors. It is important to note that the sample size is currently limited, and efforts are underway to increase the statistics to obtain more accurate results.

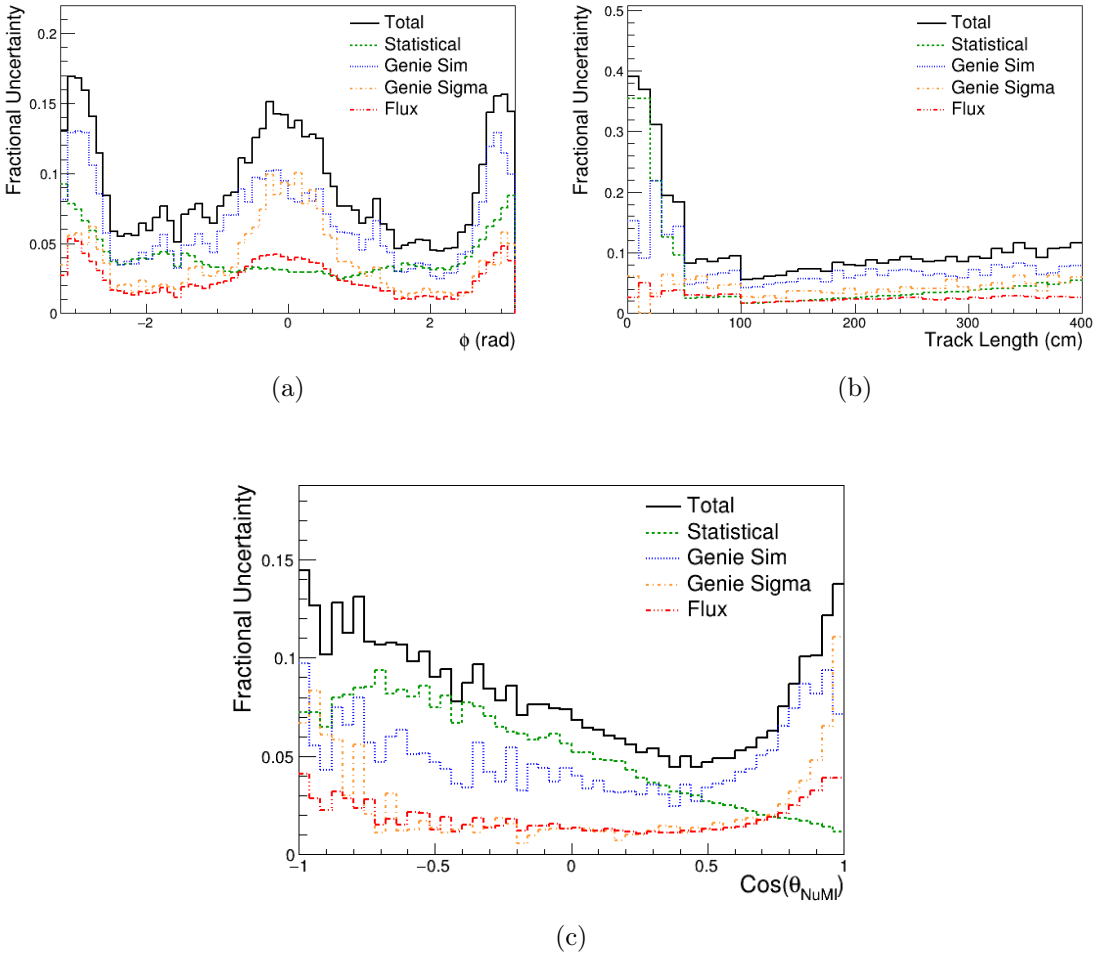

(a) (b)

(c)

Figure 4.21: Distributions of various error contributions for the variables (a) ϕ angle, (b) muon track length, and (c) $\cos(\theta_{NuMI})$. The black solid line represents the total errors, the green dashed line corresponds to the statistical errors, the blue dotted line indicates the Genie *multisim* approach, the yellow dash-dotted line represents the Genie *multisigma* weights, and the red dash-dotted line shows the flux contribution.

4.11 Summary and Future Prospects

In this chapter, the procedure for measuring the cross-section of the NuMI ν_μ CC inclusive channel was studied.

The next step in the analysis involves cross-section extraction using the open-source GUNDAM [99] likelihood fitting and cross-section extraction machinery developed by the T2K collaboration [100]. The implementation in ICARUS can be consulted in these documents [100–102]. The essential idea is to allow the signal cross-section to vary freely within predefined true bins during a simultaneous fit to both the signal and control samples. This fit also includes parameters for each systematic uncertainty, ensuring that all sources of error are considered. This approach estimates the number of selected signal events in truth space, effectively performing an unfolding and background subtraction. The unfolded event rate is then converted into a cross-section by dividing it by the efficiency and normalization factors: the number of targets and the neutrino flux integral for the total data exposure. Uncertainties are propagated via a multi-universe approach. The use of GUNDAM to extract the cross-section from the ν_μ CC inclusive channel is currently in the basic testing phase of installation and familiarization with the software.

Effective selection of the ν_μ CC candidates has been achieved, with a sample purity of 74%. Additionally, the background due to cosmic ray interactions reaching the ICARUS detector has been studied. In the inclusive selection, this background accounts for 16%. Although this value is small, preliminary studies using the CRT-PMT matching tool (in its test mode) have shown significant rejection of cosmic rays. The performance of this tool is currently being tested for integration into the event selection, as the Cosmic Ray Tagger (CRT) can be used as a muon telescope to help identify and further reject cosmic rays.

The unfolding studies, while showing good consistency between the true and reconstructed information of the MC sample studied, still require an examination of

the appropriate bin width for the variables under investigation.

In the work presented so far, muon momentum has not been included due to previous inconsistencies observed in the model when comparing the reconstruction information with the true information in the MC samples and when making comparisons with the data. More detailed studies with the multiple Coulomb scattering (MCS) model are currently underway, along with the incorporation of the latest detector calibration updates to the samples. The short-term plan is to perform a study similar to the one shown with the $\cos(\theta_{NuMI})$ variable but with muon momentum.

As mentioned above, the systematic uncertainties are still preliminary and conservative. Efforts are ongoing to better understand and improve the detector systematics.

It is worth mentioning that the event selection studies performed in this analysis have been used to validate and improve event reconstruction and particle identification.

Chapter 5

Neutrino-electron scattering radiative corrections in short baseline neutrino experiments

In our current era, precision tests have become essential to validate Standard Model (SM) predictions and, consequently, to venture reliably into the search for new physics. Within the neutrino sector, various scattering processes serve as valuable tools for conducting precision tests, allowing us to make highly accurate measurements of SM parameters. One such pivotal process is neutrino scattering off electrons [86, 103]. Characterized by its pure leptonic nature, this process has provided clear signatures in different predictions of the SM. Notably, it played an important role in confirming the existence of neutral currents [14–16, 104], observed in the 1973 Gargamelle experiment at CERN [105]. Furthermore, its purely leptonic character facilitates numerous precision tests on electroweak (EW) parameters, including accurate measurements of the weak mixing angle. Additionally, most Next-to-Leading Order (NLO) radiative corrections for this scattering process can be analytically evaluated, making it a prototype for more complex cases like neutrino scattering

with the nucleus, studied in previous chapters.

Furthermore, the radiative corrections of neutrino-electron scattering include flavor-dependent contributions unique to neutrino interactions. This flavor dependent correction is typically associated with the neutrino charge radius, serving as a novel test of the SM [106–110].

Following the confirmation of the neutrino oscillation mechanism by Takaki Kajita and Arthur B. McDonald, the experimental advancements in this sector have been remarkable. The constructions of long-baseline experiments anticipate precise measurements shortly, particularly in the pursuit of discovering a CP-violating phase. These experiments are especially promising since we expect intense neutrino beams from them. The near detectors (ND) of these experiments will be prepared to measure the neutrino-electron scattering process with a high sensitivity to radiative corrections.

This chapter will explore the sensitivity to the radiative corrections of neutrino-electron scattering, focusing on a future DUNE-PRISM-like [111,112] near detector. Additionally, we will study the potential to identify the contribution of an effective, gauge-independent neutrino charge radius [108,110].

5.1 The neutrino-electron scattering

The process of neutrino-electron scattering is a phenomenon predicted by the SM. This purely leptonic process involves a neutrino interacting with an electron through the exchange of a virtual vector boson, Z or W, depending on whether the interaction is mediated via neutral (NC) or charged current (CC), as shown in Fig. 5.1. In the case of the electron neutrino (ν_e), this interaction includes a charged component, which causes a larger cross-section; this is illustrated in Fig. 5.2.

In the following sections, we will focus on the interaction between ν_μ ($\bar{\nu}_\mu$) and electrons. This interaction only involves leptons and is a neutral current process

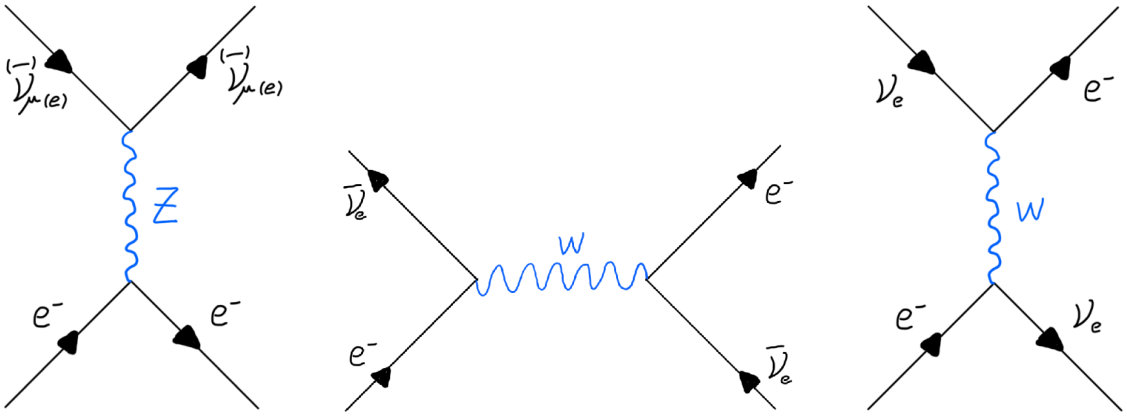

(a) NC: $\nu_i e^- \rightarrow \nu_i e^-$ and $\bar{\nu}_i e^- \rightarrow \bar{\nu}_i e^-$ (b) CC: $\bar{\nu}_e e^- \rightarrow \bar{\nu}_e e^-$ (c) CC: $\nu_e e^- \rightarrow \nu_e e^-$

Figure 5.1: Feynman diagrams for neutrino and antineutrino-electron scattering via (a) neutral current (for neutrino and antineutrino), (b) antineutrino charged current, and (c) neutrino charged current interaction.

mediated by the Z boson. Examining this process at low energies of the weak mixing angle allows us to conduct tests on the Standard Model. Additionally, we can explore the potential presence of an effective neutrino charge radius (NCR).

At tree level, the differential cross-section expression for the neutrino scattering off electrons in terms of the electron recoil energy, T, can be expressed as

$$\frac{d\sigma}{dT} = \frac{2m_e G_F^2}{\pi}\left\{g_L^2 + g_R^2\left(1 - \frac{T}{E_\nu}\right)^2 - g_R g_L m_e \frac{T}{E_\nu^2}\right\}, \tag{5.1}$$

where G_F is the Fermi constant, m_e is the mass of the electron, and E_ν is the incident neutrino energy. It is worth noting that at high energies, i.e., when $E_\nu >> m_e$, the third term in this expression becomes negligible. In this equation, the coupling constants g_L and g_R are defined as

$$g_L = \delta_{e\alpha} - \frac{1}{2} + \sin^2\theta_W \tag{5.2a}$$

and

$$g_R = \sin^2\theta_W\,, \tag{5.2b}$$

where θ_W refers to the weak mixing angle and the subscript α in the Kronecker Delta denotes either electron (e) or muon (μ) neutrinos. The term $\delta_{e\alpha}$ comes from the charged current contribution for the electron neutrino case, which is absent for the muon neutrino case. Moreover, in the case of antineutrino scattering, $\bar{\nu} - e^-$, we must interchange the coupling constants, $g_L \leftrightarrow g_R$ in Eq. (5.1).

The corresponding cross-sections will be

$$\sigma(\nu_\mu e^- \to \nu_\mu e^-) = \frac{m_e G_F^2 E_\nu}{2\pi}\left[1 - 4\sin^2\theta_W + \frac{16}{3}\sin^4\theta_W\right] \tag{5.3a}$$

$$\sigma(\bar{\nu}_\mu e^- \to \bar{\nu}_\mu e^-) = \frac{m_e G_F^2 E_\nu}{2\pi}\left[\frac{1}{3} - \frac{4}{3}\sin^2\theta_W + \frac{16}{3}\sin^4\theta_W\right] \tag{5.3b}$$

$$\sigma(\nu_e e^- \to \nu_e e^-) = \frac{m_e G_F^2 E_\nu}{2\pi}\left[1 + 4\sin^2\theta_W + \frac{16}{3}\sin^4\theta_W\right] \tag{5.3c}$$

and

$$\sigma(\bar{\nu}_e e^- \to \bar{\nu}_e e^-) = \frac{m_e G_F^2 E_\nu}{2\pi}\left[\frac{1}{3} + \frac{4}{3}\sin^2\theta_W + \frac{16}{3}\sin^4\theta_W\right]. \tag{5.3d}$$

These expressions show that the contribution from the charged current of the $\nu_e e^-$ scattering produces a larger cross-section than the $\nu_\mu e^-$ scattering resulting from only the neutral current.

Furthermore, considering the previous cross-sections, expressed now in terms of the coupling constants, we can compute the values of g_L and g_R that simultaneously fulfill the four different cross-sections. We can plot the result of such a computation, either in terms of g_L and g_R or in terms of the vector and axial couplings g_V and g_A by using the relationship [113]

$$2g_L = g_V + g_A \tag{5.4a}$$

and

$$2g_R = g_V - g_A\,, \tag{5.4b}$$

These curves are shown in Fig. 5.2, which shows two different intersection points, common to all four curves.

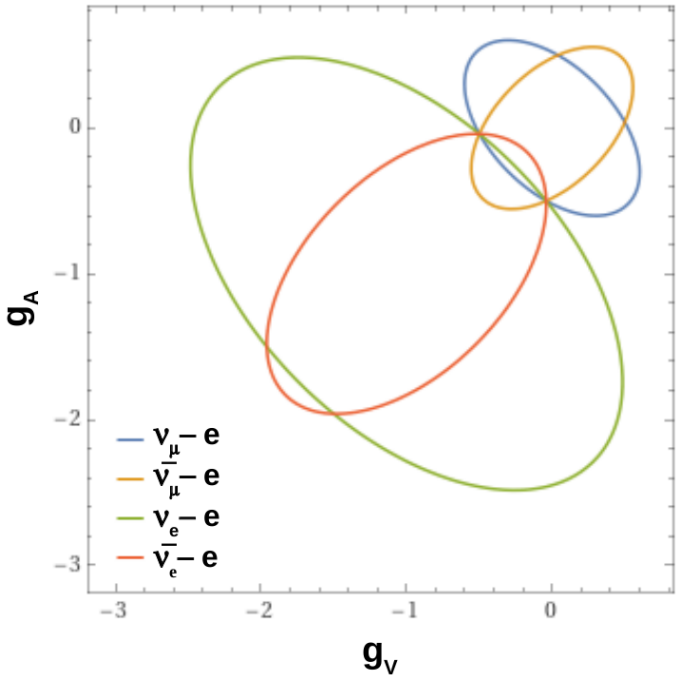

Figure 5.2: Contours of the cross-section for neutrino and antineutrino-electron interaction in the $g_V - g_A$ plane as in Ref. [113]. Each contour corresponds to ideal measurements with $\sin^2\theta_W = 0.23$.

5.2 Radiative corrections in the neutrino-electron scattering

Being free of QCD interactions, the leptonic electroweak sector serves as a precision physics probe, offering an ideal setting to search for the impact of higher-order contributions in the perturbation series, known as *radiative corrections*. Currently, experimental precision enables testing the standard model with quantum corrections, incorporating loops in scattering processes. In this context, despite the lower

statistics, neutrino scattering off electrons may offer a new independent window to make precision tests of the Standard Model.

In the context of neutrino scattering off electrons, radiative corrections divide into two types based on their dynamic origin [21, 114–121]: (a) Quantum Electrodynamics (QED) corrections, involving processes like the creation and absorption of photons in the electronic current, illustrated in Fig. 5.3a; (b) Electroweak (EW) corrections, arising from the exchange of W and Z bosons, which is exemplified in Fig. 5.3b.

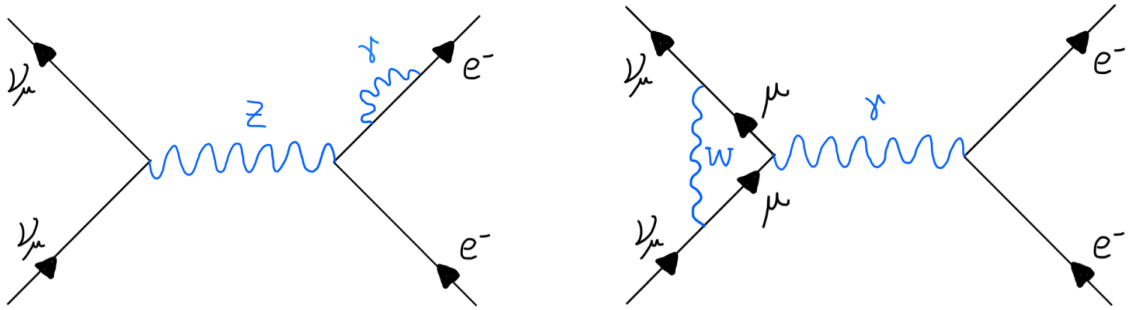

(a) Quantum Electrodynamics corrections.

(b) Electroweak corrections.

Figure 5.3: Feynman diagrams exemplifying higher-order radiative corrections (a) Quantum Electrodynamics (QED) effects with $e\gamma e$ vertices and (b) Electroweak (EW) corrections involving $\mu W \nu_\mu$ vertices.

For neutrino-electron elastic scattering, the differential cross-section, including the Electroweak and Quantum Electrodynamics corrections up to order $\mathcal{O}(\alpha)$ and utilizing the $\overline{MS}$ renormalization scheme, is expressed as [114]

$$\frac{d\sigma'}{dT} = \frac{2m_e G_F^2}{\pi}\left\{ g_L'^2(T)\left[1+\frac{\alpha}{\pi}f_-(z)\right] + g_R'^2(T)\left(1-\frac{T}{E_\nu}\right)^2\left[1+\frac{\alpha}{\pi}f_+(z)\right] \right.$$
$$\left. -g_R'(T)g_L'(T)m_e\frac{T}{E_\nu^2}\left[1+\frac{\alpha}{\pi}f_{+-}(z)\right]\right\}, \tag{5.5}$$

where α denotes the fine-structure constant, and the impact of QED corrections is contained within the functions $f_+(z)$, $f_-(z)$, and $f_{+-}(z)$, which are dependent

on $z = T/E_\nu$. The explicit forms of these functions are detailed in Appendix C. The values of the $f(z)$ functions exhibit significant variations with neutrino energy within the considered range. In the case of the antineutrino cross-section, the $g'_{L,R}$ couplings have to be interchanged $g'_L \leftrightarrow g'_R$, while the three $f(z)$ functions remain unaltered.

On the other hand, the contribution of the EW corrections is implicit in the new coupling constants, $g'_L(T)$ and $g'_R(T)$ that cease to remain constant. They now depend on the electron recoil energy T and are expressed as

$$g'_L(T) = \rho_{\mathrm{NC}} \left[\frac{1}{2} - \kappa_{\nu_l}(T) \sin^2 \theta_W^{(m_Z)} \right] \tag{5.6a}$$

and

$$g'_R(T) = -\rho_{\mathrm{NC}} \kappa_{\nu_l}(T) \sin^2 \theta_W^{(m_Z)} \,. \tag{5.6b}$$

Here, m_Z denotes the Z boson mass, and $\sin^2 \theta_W^{(m_Z)}$ represents $\sin^2 \theta_W$ calculated at the m_Z scale. In addition, the renormalization factor, ρ_{NC} is independent of the electron recoil energy T, and according to Ref. [117], its expression is given as

$$\rho_{\mathrm{NC}} = 1 + \frac{\hat{\alpha}}{4\pi \hat{s}^2} \left\{ \frac{3}{4\hat{s}^2} \ln c^2 - \frac{7}{4} + \frac{2\hat{c}_Z}{\hat{c}^2} + \frac{3}{4}\xi \left[\frac{\ln\left(\frac{c^2}{\xi}\right)}{c^2 - \xi} + \frac{1}{c^2} \frac{\ln \xi}{1 - \xi} \right] + \frac{3}{4} \frac{m_t^2}{m_W^2} \right\}, \tag{5.7}$$

where s and c denote the sine and cosine of θ_W, respectively. The hat over the parameters signifies their values calculated at the m_Z scale. Specifically, $\hat{c}_Z = \frac{19}{8} - \frac{7}{2}\hat{s}^2 + 3\hat{s}^4$, $\xi = \frac{m_H^2}{m_Z^2}$, and $m_{H,t,W}$ represent the masses of the Higgs boson, the top quark, and the W boson, respectively. The numerical value for ρ_{NC} is 1.014032.

Furthermore, the coupling constants 5.6a and 5.6b reveal that, unlike ρ_{NC}, the form factor $\kappa_{\nu_l}(T)$ depends on the electron recoil energy (T) or, equivalently, the square of the four-momentum transferred $q^2 = -2m_e T$, and its expression is given

as

$$\kappa_{\nu_l}(q^2) = 1 - \frac{\alpha}{2\pi\hat{s}^2}\left[\sum_i \left(C_{3i}Q_i - 4\hat{s}^2Q_i^2\right) J_i(q^2) - 2J_l(q^2) + \ln c\left(\frac{1}{2} - 7\hat{c}^2\right) + \frac{\hat{c}^2}{3} + \frac{1}{2} + \frac{\hat{c}_\gamma}{\hat{c}^2}\right]. \tag{5.8}$$

Here, the sum encompasses all charged fermions, and an additional factor of three must be accounted for the color degree of freedom of quarks. Q_i denotes the electric charge, C_{3i} represents twice the third component of weak isospin, $\hat{c}_\gamma = \frac{19}{8} - \frac{17}{4}\hat{s}^2 + 3\hat{s}^4$, and

$$J_i(q^2) = \int_0^1 x(1-x)\ln\left(\frac{m_i^2 - q^2x(1-x)}{m_Z^2}\right)dx\,, \tag{5.9}$$

where m_i represents the i-th fermion mass. Furthermore, the flavor dependence of the incident neutrino is expressed through the term $2J_l(q^2)$. In this work, we assume a ν_μ flux, hence we will have $2J_\mu(q^2)$.

To gain a broad understanding of the distinct dependencies on EW corrections for neutrino and antineutrino scattering off electrons, let us begin by examining the simple scenario of a monoenergetic neutrino beam. Our focus will be on the impact of κ_{ν_μ} (Eq (5.8) for muon neutrinos). The cross-section is now expressed through an equation kindred to Eq. (5.1), although modified with the corrected coupling constants

$$\tilde{g}_L \approx \frac{1}{2} - \kappa_{\nu_\mu}x \tag{5.10a}$$

and

$$\tilde{g}_R \approx -\kappa_{\nu_\mu}x, \tag{5.10b}$$

where we abbreviate $x = \sin^2\theta_W$.

The distinctions between the differential cross-sections, one incorporating EW radiative corrections ($d\sigma'_{\mathrm{EW}}/dT$) and the other at tree-level order and defined by

Eq. (5.1), are, for neutrinos and antineutrinos, respectively,

$$\Delta\sigma_{\nu_\mu e} \equiv \frac{d\sigma'_{\mathrm{EW}}}{dT} - \frac{d\sigma}{dT} \sim \Delta g_L + \Delta g_R \left(1 - 2\frac{T}{E_\nu} + \frac{T^2}{E_\nu^2}\right) - \Delta g_{R,L} m_e \frac{T}{E_\nu^2} \tag{5.11a}$$

and

$$\Delta\sigma_{\bar{\nu}_\mu e} \equiv \frac{d\bar{\sigma}'_{\mathrm{EW}}}{dT} - \frac{d\bar{\sigma}}{dT} \sim \Delta g_R + \Delta g_L \left(1 - 2\frac{T}{E_\nu} + \frac{T^2}{E_\nu^2}\right) - \Delta g_{R,L} m_e \frac{T}{E_\nu^2}\,, \tag{5.11b}$$

here, the terms Δg_L, Δg_R, and $\Delta g_{R,L}$ denote the differences:

$$\Delta g_L \equiv \tilde{g}_L^2 - g_L^2 = (\kappa_{\nu_\mu}^2 - 1)x^2 \left[1 - \frac{1}{(\kappa_{\nu_\mu} + 1)x}\right]\,, \tag{5.12a}$$

$$\Delta g_R \equiv \tilde{g}_R^2 - g_R^2 = (\kappa_{\nu_\mu}^2 - 1)x^2\,, \tag{5.12b}$$

and

$$\Delta g_{R,L} \equiv \tilde{g}_R \tilde{g}_L - g_R g_L = (\kappa_{\nu_\mu}^2 - 1)x^2 \left[1 - \frac{1/2}{(\kappa_{\nu_\mu} + 1)x}\right]\,. \tag{5.12c}$$

Considering $\kappa_{\nu_\mu} \approx 1$ and $x \approx 1/4$, it follows that $(\kappa_{\nu_\mu} + 1)x \approx 1/2$. This implies

$$\Delta g_L \approx -\Delta g_R \qquad \text{and} \qquad \Delta g_{L,R} \approx 0\,, \tag{5.13}$$

and, therefore:

$$\Delta\sigma_{\bar{\nu}_\mu e} \approx -\Delta\sigma_{\nu_\mu e} \approx \Delta g_R \left(-2 + \frac{T}{E_\nu}\right)\frac{T}{E_\nu}\,. \tag{5.14}$$

This result highlights an asymmetrical correlation between EW radiative corrections in neutrino and antineutrino scattering. In contrast, QED corrections result in the same relative deviation from the tree level for both neutrinos and antineutrinos. These phenomena are visualized in Fig. 5.4, illustrating the relative contributions (Eq. (5.15)) of different correction groups for a theoretical 10 GeV monoenergetic neutrino beam. The tree-level differential cross-section deviation is expressed as the ratio:

$$R_{\mathrm{X}} := \frac{\frac{d\sigma'_{\mathrm{X}}}{dT} - \frac{d\sigma}{dT}}{\frac{d\sigma}{dT}}\,, \tag{5.15}$$

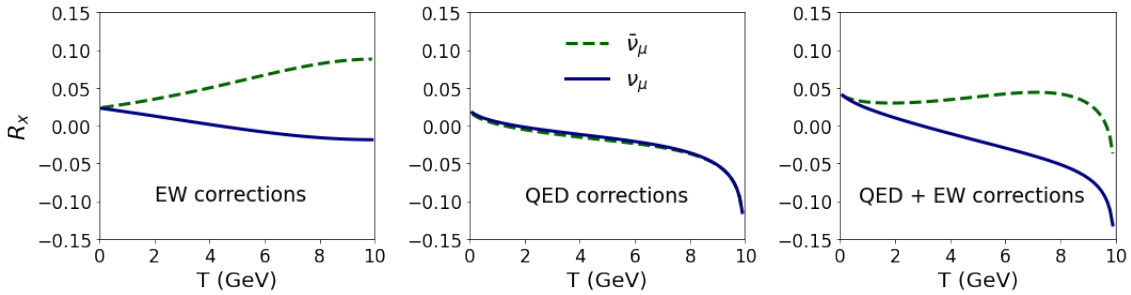

Figure 5.4: Contrast between the ratios of radiative corrections in neutrino and antineutrino beam modes at a constant neutrino energy of 10 GeV. a) Contribution of EW corrections, b) contribution of QED corrections, and c) overall contributions.

where X signifies the simultaneous inclusion of EW, QED, or both corrections. While this correlation's behavior was computed for fixed neutrino energy, the qualitative pattern remains consistent across the entire neutrino beam spectrum.

The combined impact of EW and QED corrections (Fig. 5.4c) induces changes in the cross-section of antineutrino-electron scattering, consistently resulting in an increment. This contrasts with the neutrino scenario, where radiative corrections increase the cross-section primarily in the low-energy range, below approximately 2 GeV in our illustrated case (Fig. 5.4). Beyond this threshold, the cross-section experiences a decrease. Understanding this behavior is crucial for investigating specific experimental configurations, as we will demonstrate in Sec. 5.4.

5.3 Effective neutrino charge radius

We now scrutinize the contribution of $\kappa_{\nu_l}(q^2)$, as defined in Eq. (5.8). This correction depends on the specific process, including different neutrino flavors, leading to distinct values. To better understand this, we can break down the expression into two parts. The first part, denoted as $\kappa_\nu(q^2)$, represents a common contribution

shared by all neutrino flavors:

$$\kappa_\nu(q^2) = 1 - \frac{\alpha}{2\pi\hat{s}^2}\left[\sum_i \left(C_{3i}Q_i - 4\hat{s}^2Q_i^2\right) J_i(q^2) + \ln c\left(\frac{1}{2} - 7\hat{c}^2\right) + \frac{\hat{c}^2}{3} + \frac{\hat{c}_\gamma}{\hat{c}^2}\right], \tag{5.16}$$

while the second part, which depends only on the neutrino flavor, will be

$$-\frac{\alpha}{2\pi\hat{s}^2}\left[-2J_l(q^2) + \frac{1}{2}\right]. \tag{5.17}$$

If we focus on the expression in parentheses, $-2J_l(q^2) + \frac{1}{2}$, and evaluating it at $q = 0$

$$-2J_l(0) + \frac{1}{2} = \frac{1}{6}\left[3 - 2\ln\left(\frac{m_l^2}{m_Z^2}\right)\right], \tag{5.18}$$

we get an expression linked to the neutrino charge radius (NCR):

$$\left\langle r_{\nu_l}^2 \right\rangle = \frac{G_F}{4\sqrt{2}\pi^2}\left[3 - 2\ln\left(\frac{m_l^2}{m_W^2}\right)\right], \tag{5.19}$$

for the μ neutrino flavor, the numerical value of $\left\langle r_{\nu_\mu}^2 \right\rangle$ is 2.4×10^{-33} cm^2 [122].

With the aid of this expression, we can further decompose the couplings $g'_L(T)$ and $g'_R(T)$ into two components. One component remains independent of the incoming neutrino flavor, while the other is expressed in terms of the NCR [122],

$$g_{L,R}^{\prime(\nu_\mu,e)}(T) \sim g_{L,R}^{\prime(\nu,e)}(T) + \left[\frac{2}{3}m_W^2\left\langle r_{\nu_\mu}^2 \right\rangle\right]\sin^2\theta_W^{(m_Z)}, \tag{5.20}$$

where the numerical value of $\left[\frac{2}{3}m_W^2\left\langle r_{\nu_\mu}^2 \right\rangle\right]\sin^2\theta_W^{(m_Z)}$ is approximately 0.0058.

Notably, the right-hand side of Eq. (5.18) can be written in terms of m_W by adding $\frac{1}{3}\ln\left(\frac{m_W^2}{m_Z^2}\right)$ to it. This addition contributes only to approximately 0.04% of the difference in the shaded region of Fig.5.5, which is the region of interest in this study. Specifically, we find $\kappa_{\nu_\mu}^{(m_Z)} = 0.9921$ and $\kappa_{\nu_\mu}^{(m_W)} = 0.9925$.

Now, revisiting Eq. (5.16), within the energy range interest to this study, this contribution is determined as $\kappa_\nu(q^2) = 1.017$. Simultaneously, the flavor-dependent

contribution from Eq. (5.17) yields a numerical value of -0.025 in this region. This value contributes to an approximate 3% difference between κ_{ν_μ} (Eq. (5.8)) and κ_ν (Eq. (5.16)), as illustrated in Fig. 5.5. As $Q \equiv \sqrt{-q^2}$ approaches zero, the values of κ, specifically the flavor-dependent part from Eq. (5.17), remain constant. This includes the energy range of interest in this study, delimited by the shaded vertical band in Fig. 5.5.

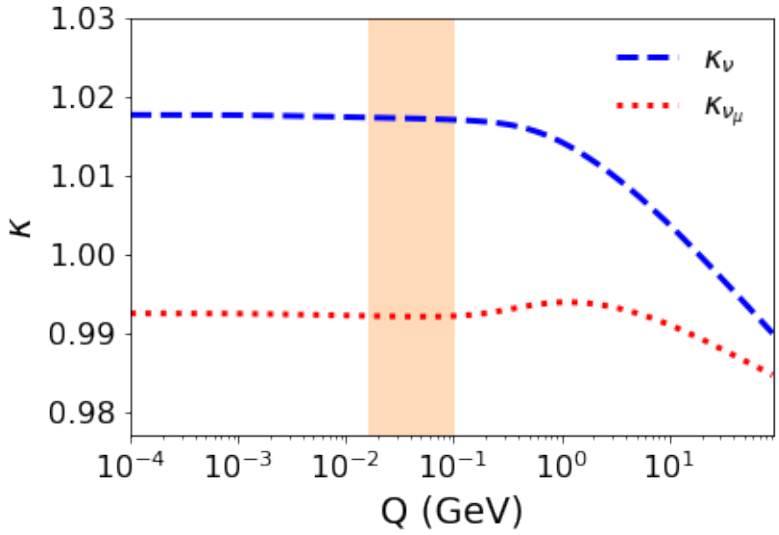

Figure 5.5: The functions κ_ν, and κ_{ν_μ} are illustrated as a function of Q. The dashed blue line corresponds to κ_ν, as given by Eq. (5.16), while the dotted red line corresponds to κ_{ν_μ} from Eq. (5.8). The shaded area corresponds to the electron recoil energy (T), within which we investigate the impact of radiative corrections and the experimental sensitivity to the neutrino charge radius.

The numerical values of κ and the coupling constants are presented in Table 5.1. The first row displays the flavor-independent values, excluding the term with the NCR. The second row presents the values incorporating the NCR term.

NCR	κ	g'_L	g'_R
no	1.0176	0.2684	-0.2386
yes	0.9925	0.2743	-0.2327

Table 5.1: Numerical value of κ (at $q^2 = 0$) and the couplings $g'_L(T)$ and $g'_R(T)$ are presented, subject to the incorporation of the neutrino charge radius term.

5.4 The DUNE case

The Deep Underground Neutrino Experiment (DUNE) [34] stands at the forefront of global neutrino research and is one of the most ambitious experimental programs worldwide. As mentioned previously, the main purpose of DUNE is to search for the existence of a CP-violating phase and the potential to measure neutrino oscillation properties with unprecedented precision, making it one of the most challenging neutrino experiments in the coming years. The baseline experimental setup involves two neutrino detectors corresponding to a long and a short baseline. The far detector (FD) [35] will be located at the Sanford Underground Research Laboratory in South Dakota with 40 kt at 1,300 km downstream from the source and a near detector (ND) [111] in Illinois at Fermilab.

The ND is strategically placed near the neutrino source to characterize the neutrino beam before oscillation, playing a pivotal role in accomplishing DUNE's precision measurement objectives. To address systematic uncertainties such as absolute and relative flux, nuclear effects, etc., the ND is planned to adopt LArTPC technology, similar to the FD, enabling highly precise measurements of neutrino interactions and the potential discovery of new physics beyond the Standard Model. As a part of the DUNE Near Detector system, the PRISM prototype will be situated 574 m from the beam target at Fermilab. PRISM [112, 123] will employ the same LArTPC technology as the DUNE FD and boasts a unique feature of mobility, allowing it to

operate off the axis of the beam up to 3.6°. This distinctive characteristic exposes PRISM to different fluxes and spectra, minimizing systematic uncertainties in the flux, cross-section, and detector effects within the energy spectrum. As a result, PRISM will enhance the sensitivity of neutrino interaction measurements.

To investigate the sensitivity of DUNE-PRISM to the radiative corrections, we compute the expected number of events for ν_μ scattering off electrons. This analysis covers various off-axis beam angles, allowing us to identify the optimal angular window and energy range for detecting differences in event numbers attributed to radiative corrections, particularly the NCR effect.

To conduct this analysis, we utilize predicted neutrino energy spectra corresponding to various angles of the incident beam. The flux data used in our study are sourced from Ref. [124]. Figure 5.6 shows the results after interpolating the data reported in Ref. [124] for each distinct beam direction (more flux spectra can be found in Appendix D).

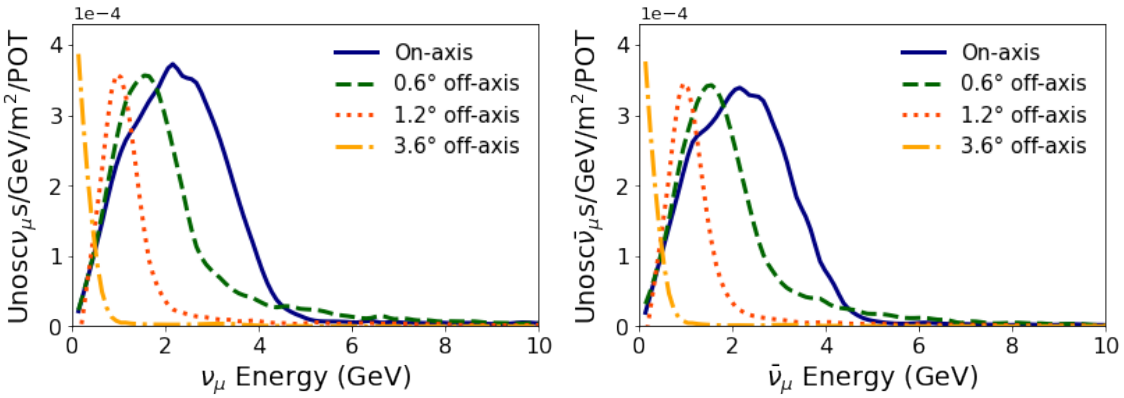

(a) ν_μ beam mode

(b) $\bar{\nu}_\mu$ beam mode

Figure 5.6: Interpolation of the fluxes at different off-axis locations, as detailed in Ref. [124]. (a) Neutrino mode (ν_μ) (b) Antineutrino mode ($\bar{\nu}_\mu$).

In our analysis, considering the neutrino-electron scattering, the number of tar-

gets in the detector corresponds to the total number of electrons within the liquid argon mass, estimated at 75 tons [112]. Assuming a runtime of 3.5 years for both neutrino and antineutrino modes, we calculate the expected number of events, both with and without radiative corrections. This enables us to effectively isolate and identify the specific contribution of the Neutrino Charge Radius to the overall corrections.

For each PRISM axis configuration based on angular location, it is necessary to compute the average cross-section. This computation involves integrating the electron recoil energy from its threshold energy, T_{min}, up to the maximum kinetically allowed value, T_{max}, which is approximately E_ν^{max}, then

$$\sigma = \int_{T_{min}}^{T_{max}} f(T) dT, \tag{5.21}$$

where $f(T)$ represents the integral of the differential cross-section, $\frac{d\sigma}{dT}(T, E_\nu)$, multiplied by the corresponding neutrino flux, $\lambda(E_\nu)$,

$$f(T) = \int_{E_\nu^{min}(T)}^{E_\nu^{max}} \frac{d\sigma}{dT}(T, E_\nu)\, \lambda(E_\nu) dE_\nu \,, \tag{5.22}$$

here, $E_\nu^{min}(T)$ is the minimum neutrino energy considered, determined by the detector's electron energy threshold.

After computing the cross section using Eq. (5.21), it is essential to determine the number of events by considering the detector's exposure, denoted as $\mathscr{C}$:

$$N = \sigma \times \mathscr{C} \,, \tag{5.23}$$

The exposure factor incorporates considerations such as the total number of target electrons in the detector, the number of protons on target per year 1.1×10^{21} POT/year [124], and a runtime of 3.5 years in the neutrino beam mode plus an additional 3.5 years in the antineutrino beam mode.

As discussed in Section 5.2, the inclusion of radiative corrections is anticipated to increase of the antineutrino-electron scattering cross-section when compared to the

tree-level calculation. Consequently, an increase in the expected number of events is foreseen. In contrast, for the neutrino mode, as discussed in the subsequent section, a decrease in the expected number of events is predicted for electron recoil energies exceeding approximately 0.7 GeV.

5.4.1 Results and Discussion

In this section, we analyze our results using two electron recoil energy thresholds: 0.2 GeV and 0.7 GeV. The latter is chosen to maximize distinctions between the number of events predicted at the tree level and those incorporating radiative corrections for the neutrino beam mode scenario. The 0.7 GeV threshold is particularly significant due to the contrasting behavior observed in the antineutrino channel, where radiative corrections consistently increase the expected number of events, independently of the energy range observed, contrary to the neutrino case. As discussed previously, radiative corrections induce a decrease in the number of neutrino events, particularly beyond the $\sim$ 0.7 GeV threshold. In the case of an on-axis neutrino beam, the impact of radiative corrections is opposite below and above the threshold of approximately 0.7 GeV. On the other hand, the integration of the differential cross-section reduces the total number of event differences. Therefore, we magnify the difference needed to detect neutrino scattering by choosing this crossing point as the threshold energy. By considering this crossing point as the threshold, we effectively amplify the difference between the predictions at the tree level and those at the one-loop level.

In Tables 5.2 and 5.3, we present a summary of the results concerning neutrino and antineutrino events, respectively. The energy range considered in our calculations spans from 0.2 GeV to 10 GeV. We provide results corresponding to the DUNE-PRISM axis location, ranging from 0° to 3.6° in intervals of 0.6°, while also accounting for the contribution of the NCR in the radiative corrections. Notably,

	Number of ν_μ Events					
			Without NCR		With NCR	
Axis location	Tree level	σ_{stat}	EW+QED	Δ	EW+QED	Δ
0.0°	27134	165	25859	-1275	26567	-567
0.6°	18099	135	17243	-856	17712	-387
1.2°	5884	77	5589	-295	5749	-135
1.8°	2600	51	2466	-134	2538	-62
2.4°	1397	37	1324	-73	1364	-33
3.0°	711	27	674	-37	694	-17
3.6°	440	21	418	-22	430	-10

Table 5.2: The total number of events resulting from $\nu_\mu e$ scattering within an energy range of 0.2 to 10 GeV is presented. Our analysis encompasses both the tree level and radiative corrections, accounting for the neutrino charge radius and without. The first column illustrates the DUNE-PRISM axis location, ranging from 0° to 3.6° off-axis. σ_{stat} denotes the statistical error while Δ represents the difference between the number of events calculated at the tree level and those including radiative corrections. Further information is detailed in the text.

upon considering the NCR, the difference in the number of events, denoted as $|\Delta|$, compared to the tree-level calculation, manifests more prominently for antineutrinos than for neutrinos. Furthermore, a noteworthy observation from these tables indicates that the discrepancy in the number of events exceeds the statistical error for off-axis angles equal to or less than 1.8°. Particularly, for the on-axis scenario, the statistical error is very small compared to the difference in the number of events. Hence, given appropriate control over systematic uncertainties, it appears feasible to determine the NCR contributions.

Table 5.2 presents the results for the neutrino beam mode, revealing that $|\Delta|$

	Number of $\bar{\nu}_\mu$ Events					
			Without NCR		With NCR	
Axis location	Tree level	σ_{stat}	EW+QED	Δ	EW+QED	Δ
0.0°	18775	137	19931	1156	19447	672
0.6°	11969	109	12715	746	12402	433
1.2°	3993	63	4251	258	4141	148
1.8°	1181	34	1260	79	1226	45
2.4°	645	25	689	44	670	25
3.0°	437	21	467	30	454	17
3.6°	315	18	336	21	327	12

Table 5.3: The total number of events resulting from $\bar{\nu}_\mu e$ scattering within an energy range of 0.2 to 10 GeV is presented. Our analysis encompasses both the tree level and radiative corrections, accounting for the neutrino charge radius as well as without. The first column illustrates the DUNE-PRISM axis location, ranging from 0° to 3.6° off-axis. σ_{stat} denotes the statistical error, while Δ represents the difference between the number of events calculated at the tree level and those including radiative corrections. Further information is detailed in the text.

(with NCR) exhibits a smaller magnitude compared to the antineutrino mode, as presented in Table 5.3. It is noteworthy that the neutrino mode is expected to produce a greater number of events than its antineutrino counterpart. However, the reduced $|\Delta|$ (with NCR) for neutrinos can be attributed to a change in the sign of the radiative corrections, as illustrated in Fig. 5.4.

Another case to consider involves a threshold of 0.7 GeV, corresponding to the previously mentioned crossing point for the neutrino mode. From this energy threshold, the radiative corrections for $\nu_\mu e^-$ interactions give negative values, making the effect more discernible than the 0.2 GeV threshold. Please refer to Table 5.4 for de-

	Number of Events					
			Without NCR		With NCR	
	Tree level	σ_{stat}	EW+QED	Δ	EW+QED	Δ
$\bar{\nu}_\mu$	12935	114	13850	915	13420	485
ν_μ	19947	141	18715	-1232	19318	-629

Table 5.4: The total number of events on-axis for $\bar{\nu}_\mu$ and ν_μ beam modes spans from 0.7 to 10 GeV in energy range. We consider both the tree level and radiative corrections, accounting for the presence and absence of the neutrino charge radius. σ_{stat} denotes the statistical error while Δ represents the difference between the number of events calculated at the tree level and those with radiative corrections. Further information is provided in the text.

tailed insights. Given the typically higher neutrino production rates in such beams, we can expect this observation to be a prevalent feature in similar experiments. Furthermore, this shows the importance of establishing energy thresholds based on the type of physics measurement to be conducted rather than simply relying on detector characteristics for threshold determination.

In Fig. 5.7, we illustrate the number of events expected per electron recoil energy bin for two distinct incident antineutrino beam angles. The selection of a 2 GeV range for each bin is conservative, considering that the expected energy resolution for a DUNE ND-like detector stands at approximately 10% for energies above 0.2 GeV [125]. As previously mentioned, there is an enhanced statistical significance when considering the on-axis position, resulting in lower error margins. Conversely, the statistics are worse at other angles for antineutrino fluxes, as shown in the right panel of the same Fig. 5.7, particularly for a 1.2° angle. Furthermore, the statistics decrease even further for larger angles (Appendix D shows this behavior for more off-axis angles). Additionally, we can observe from this figure that the initial en-

ergy bin demonstrates the most notable difference between the number of events at the tree level and the expected measurements with radiative corrections. Lastly, the figure emphasizes that in the antineutrino mode, a low energy threshold proves advantageous in discerning such signatures.

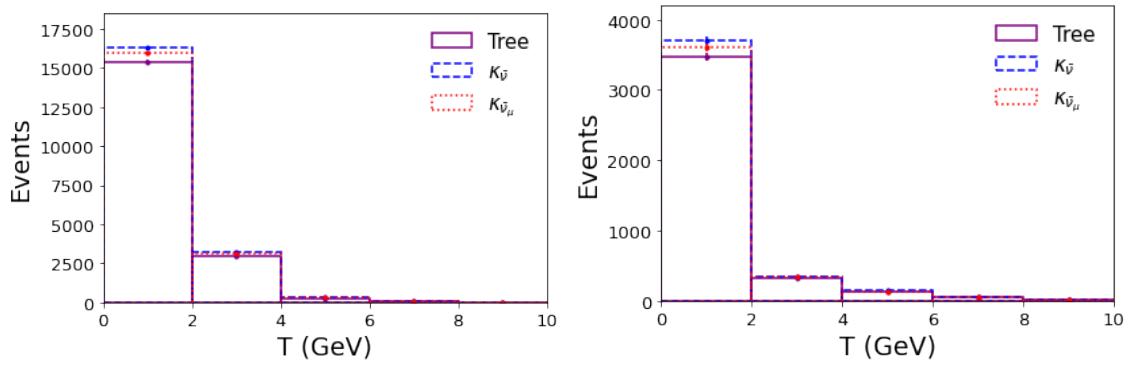

(a) On-axis

(b) 1.2° off-axis

Figure 5.7: Comparison of the expected number of $\bar{\nu}_\mu$ events at tree-level (solid purple line) and with radiative corrections, both with and without the inclusion of neutrino charge radius (represented by dotted red and dashed blue lines, respectively). Two DUNE-PRISM spectra are presented: (a) On-axis configuration on the left and (b) 1.2° off-axis on the right side. The comprehensive analysis of other cases where the beam is off-axis is found in Appendix D.

Figure 5.8 illustrates the findings regarding muon neutrinos. We observe an inverse impact of radiative corrections on the expected number of events, as previously anticipated. Notably, the overall effect of radiative corrections is comparatively smaller in the neutrino mode than in the antineutrino mode. Such difference arises from a cancellation effect observed when considering two distinct energy intervals: within the neutrino mode, the radiative corrections undergo a sign reversal within the initial energy bin. Specifically, these corrections yield a positive contribution for energies below approximately 0.7 GeV and a negative contribution for energies

exceeding this threshold, as previously discussed.

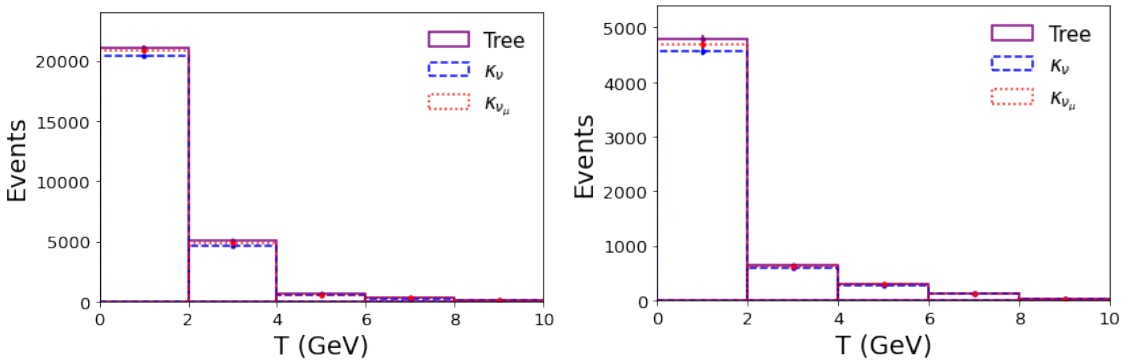

(a) On-axis (b) 1.2° off-axis

Figure 5.8: Comparison of the expected number of ν_μ events at tree-level (solid purple line) and with radiative corrections, both with and without the inclusion of neutrino charge radius (represented by dotted red and dashed blue lines, respectively). Two DUNE-PRISM spectra are presented: (a) On-axis configuration on the left and (b) 1.2° off-axis on the right side. The comprehensive analysis of other cases where the beam is off-axis is found in Appendix D.

To evaluate the sensitivity to radiative corrections, we perform a χ^2 analysis, taking into account the expected number of events at a DUNE-PRISM-like experiment along with its statistical and systematic uncertainties. In this context, we consider that the experiment will measure the Standard Model (SM) prediction, incorporating radiative corrections. The χ^2 function is defined as follows:

$$\chi^2 = \sum_{i=1}^{5} \frac{(N_i^{exp} - N_i^{theo})^2}{(\sigma_{stat}^2 + \sigma_{syst}^2)_i}\,, \tag{5.24}$$

here, i denotes the energy bin, N^{exp} represents the expected number of events predicted by the Standard Model, incorporating electroweak and QED radiative corrections, and N^{theo} signifies the theoretically calculated number of events for various κ values (as described in Eq. (5.8)). Statistical and systematic uncertainties are

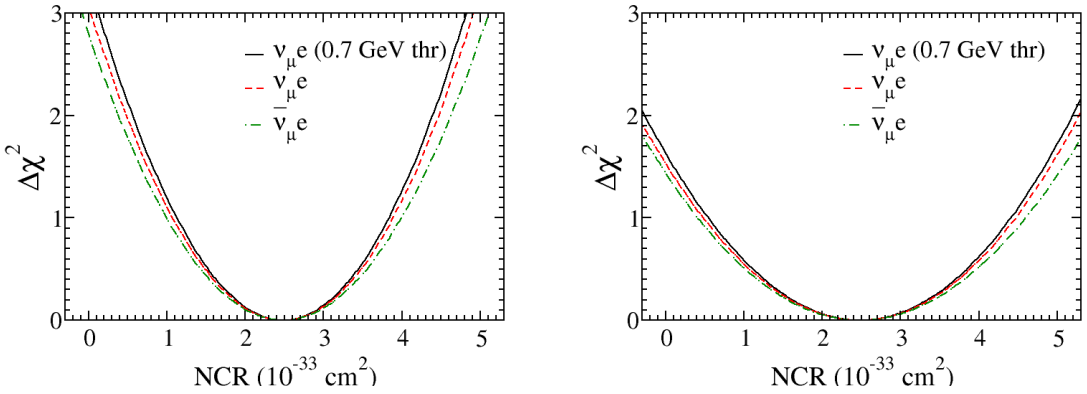

(a) 3% systematics (b) 5% systematics

Figure 5.9: The expected sensitivity to electroweak radiative corrections is presented for two systematic error scenarios: (a) Left, with a 3% systematic error, and (b) Right, with a 5% systematic error. The variation in $\Delta\chi^2$, defined as $\chi^2 - \chi^2_{\rm min}$, is shown as a function of the neutrino charge radius (NCR). The red dashed and green dot-dashed lines correspond to a 0.2 GeV threshold in ν and $\bar{\nu}$ scattering, while the black line corresponds to the 0.7 GeV ν scattering threshold. Our analysis indicates that neutrino data with a 0.7 GeV threshold and a 3% systematic error can achieve better than 90% confidence level sensitivity to the NCR under the assumptions outlined herein. Further details are provided in the text.

denoted by σ_{stat} and σ_{syst}, respectively. We assume the statistical uncertainty to be the square root of the number of events, expressed as $\sigma_{stat} = \sqrt{N^{exp}}$, and the systematic uncertainty to be either 3% or 5%. Additionally, we define $\Delta\chi^2 = \chi^2 - \chi^2_{\rm min}$, where $\chi^2_{\rm min}$ represents the minimum value of χ^2.

The results in Fig. 5.9 demonstrate the potential for discerning between predictive models, notably $\kappa_{\nu_\mu} = 0.9925$, which incorporates radiative corrections with NCR, and the scenario lacking NCR, represented by $\kappa_\nu = 1.0176$. With a 3% systematic error, the analysis shows sensitivity, achieving 1σ precision, within specific

NCR ranges: 1.0 to 4.0 $\times 10^{-33}$ cm^2 for the antineutrino channel, 1.1 to 3.9$\times 10^{-33}$ cm^2 for the neutrino channel, and 1.1 to 3.8 $\times 10^{-33}$ cm^2 for the neutrino channel with an energy threshold of 0.7 GeV. Even with a 5% systematic error, precision surpassing 1σ remains feasible. Notably, the current constraint reported in the PDG [21] for $\nu_\mu e$ scattering falls within the range of -5.3 to 6.8×10^{-33} cm^2, thus aligning with the absence of NCR.

In addition to this analysis, we have conducted an alternative assessment, as shown in Fig. 5.10. In this evaluation, we compute the $\Delta\chi^2$ considering a theoretical prediction devoid of any radiative corrections, representing the tree-level scenario. The figure illustrates that the distinguishability of radiative corrections from tree level varies depending on the magnitude of the systematic uncertainties. For the neutrino scenario discussed earlier, we adopt an energy range spanning from 0.7 to 10 GeV to enhance sensitivity, while for the antineutrino scenario, we initiate from 0.2 GeV. We employ five energy bins in both cases and present the results for two distinct incoming neutrino angles. The neutrino scenario exhibits considerable promise in its capacity to discern radiative corrections, even for relatively large systematic errors and varying incoming neutrino fluxes, due to the combination of robust statistical data and an appropriately selected energy range. Conversely, the difference is also achievable in the antineutrino scenario; however, effective control of systematic errors, ideally below 4%, is imperative.

Enhanced differentiation of radiative corrections could be achieved through the amalgamation of neutrino and antineutrino signals. It is discernible that radiative corrections manifest divergent effects on neutrino and antineutrino electron scattering, leading to a reduction in cross-section for muon neutrino interactions with electrons while inducing an increase in antineutrino interactions. This observation suggests the feasibility of defining the disparity between these signals as an observable for a more precise assessment of the neutrino charge radius. Nonetheless, a

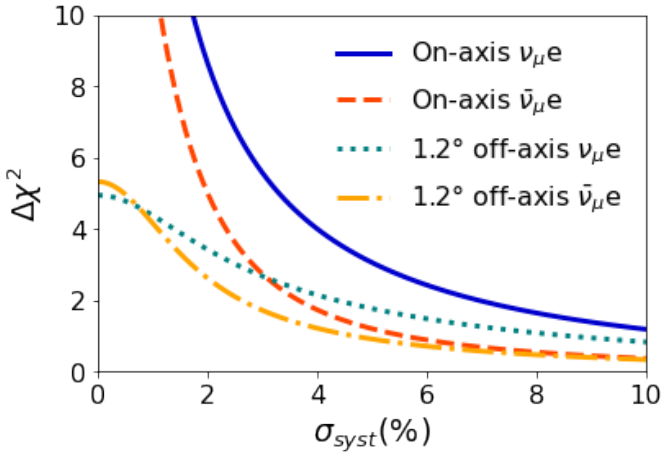

Figure 5.10: This figure depicts the expected sensitivity, represented by $\Delta\chi^2 = \chi^2 - \chi^2_{\text{min}}$, to distinguish between the tree-level scenario and the incorporation of radiative corrections according to the systematic error. Results are presented for two detector locations (on-axis and 1.2°) and both neutrino (solid and dotted lines) and antineutrino (dashed and dash-dotted lines) electron scattering scenarios. A threshold of 0.7 GeV is applied for neutrino-electron interactions to enhance sensitivity.

thorough exploration in this direction mandates a comprehensive understanding of the correlation between both signals.

5.5 Prospects for measuring the neutrino-electron scattering in current and future experiments

The prospect of measuring neutrino-electron interactions in current experiments such as SBND [3] is promising. While SBND may not offer the high statistics expected in experiments like DUNE-PRISM, it is expected to yield a substantial number of events, in the order of four hundred ν-e elastic scattering events in 6.6 $\times$

10^{20} POT [3]. This significant event count presents an opportunity to measure the cross-section of neutrino-electron interactions with considerable precision.

The ability to measure the neutrino-electron cross-section in SBND holds significant implications, particularly regarding determining the weak mixing angle. The weak mixing angle, a fundamental parameter in the electroweak theory, governs the strength of the neutral current interaction between neutrinos and electrons. By precisely measuring the neutrino-electron cross-section, SBND has the potential to provide valuable insights into the weak mixing angle, thus advancing our understanding of the fundamental forces governing particle interactions.

While SBND may not match the statistical power of larger experiments like DUNE-ND, its ability to yield hundreds of events offers a unique opportunity to probe neutrino-electron interactions. Through meticulous analysis and precise measurements, SBND can contribute significantly to our knowledge of neutrino properties and the fundamental parameters of particle physics.

On the other hand, we are spearheading an initiative to develop the foundational computational frameworks for measuring the cross-section of neutrinos scattering off electrons in preparation for the future DUNE-ND experiment. Our efforts involve the creation of foundational software tailored specifically for this purpose, focusing on employing machine learning methodologies to reconstruct the events resulting from this interaction, enhance precision, and expedite data analysis in the future. By exploiting the power of machine learning techniques, we anticipate achieving greater efficiency in managing the intricacies of neutrino interactions and deriving meaningful insights from experimental data.

While the construction of the DUNE-ND is still underway, we recognize the importance of laying the groundwork for future measurements. To this end, we have started the development of foundational codes to simulate the neutrino-electron interactions in anticipation of the DUNE-ND experiment. This endeavor encompasses

the initial stages of creating fundamental analysis software tools tailored to identify events resulting from neutrino-electron interactions.

Given that the neutrino-electron scattering cross-section per energy unit is of the order of 10^{-42} cm^2/GeV [113], significantly smaller than other interactions such as neutrino-nucleus scattering, which is of the order of 10^{-38} cm^2/GeV, the identification of events poses a formidable challenge. Thus, the development of sensitive and finely-tuned analysis software is imperative. To this end, we are employing machine learning tools to optimize the measurement process, enhance precision, and expedite data analysis in the future. By integrating machine learning methodologies, we anticipate achieving greater efficiency in managing the complexities inherent in neutrino interactions and extracting valuable insights from experimental data.

Considering the design of the DUNE-ND that employs the same technology as the DUNE-FD, i.e., LArTPC, the utilization of machine learning methodologies offers several advantages for event reconstruction as

- Complex Pattern Recognition: Machine learning excels at recognizing intricate patterns, enabling accurate reconstruction of particle trajectories and identification of interaction points.

- Adaptability to Varied Event Topologies: Neutrino interactions can manifest in diverse event topologies. Machine learning models can adapt to different event types, enhancing reconstruction accuracy across a broad spectrum of scenarios.

- Handling Noisy Data: Machine learning models can be trained to effectively handle noisy data, ensuring robust reconstruction even in the presence of uncertainties or noise in LArTPC data.

By integrating machine learning into the reconstruction process, LArTPC neutrino experiments benefit from improved precision, efficiency, and adaptability to

the complex nature of neutrino interactions, including neutrino-electron scattering.

This is an initiative that we have recently started, and we hope to develop it in the future, incorporating new members to join this effort.

5.6 Summary and Future Prospects

The precise determination of radiative corrections at low energies is crucial for testing the Standard Model (SM). Accurate measurements of the weak mixing angle in the low-energy region of accelerator-based neutrino experiments are essential. Additionally, experimental verification of the neutrino charge radius (NCR) as an effective observable in these processes is necessary. Furthermore, the ability to accurately test physics beyond the SM will be limited if these observables are not well determined.

The sensitivity of future near detectors, such as those in long-baseline neutrino experimental facilities, to radiative corrections in neutrino-electron scattering, has been studied, with DUNE-PRISM serving as an illustrative example. We focused on the NCR as an effective observable characteristic of this process. Since the primary effect of the NCR is a shift in the weak mixing angle, our study investigated the detector's sensitivity to radiative corrections, isolating the NCR effect.

Using the DUNE-PRISM configuration, which allows for multiple beam angle setups, different neutrino energy spectra were analyzed. The on-axis neutrino spectrum is found to provide a better determination of radiative corrections and potentially the NCR due to its higher statistics. It is shown that with a systematic error of approximately 3%, there are promising prospects for measuring the NCR with an error of the order of 1.5×10^{-33} cm^2.

The analysis indicates that for a ν_μ beam mode, selecting the appropriate energy window could enable the determination of the existence of the NCR, provided systematic uncertainties are well controlled. This is achievable due to the high statistics

expected in this beam mode. Conversely, for the $\bar{\nu}_\mu$ mode, the best opportunity to measure this effective observable is at small electron recoil energy values. Therefore, in this scenario, the lower the threshold, the better the measurement.

Fig. 5.11 illustrates κ_e (i.e., the κ function measured in electron-electron scatterings, as reported in the PDG [21, 119]), κ_ν, κ_{ν_μ}, and κ_{ν_e} (the latter corresponding to the κ studied in section 5.3 but with ν_e flavor instead of ν_μ flavor) as a function of the electron recoil energy, T. This is aimed at investigating the energy ranges in which measurements of both the weak mixing angle and the NCR could be made. As illustrated, the behavior of each κ is different, suggesting that measurements over a broader range of energies (particularly at low energies, where the differences between κ values are most pronounced) may provide more insight into the contribution of radiative correction effects (such as the NCR) to standard parameters. This represents a precision test of the SM in the neutrino sector.

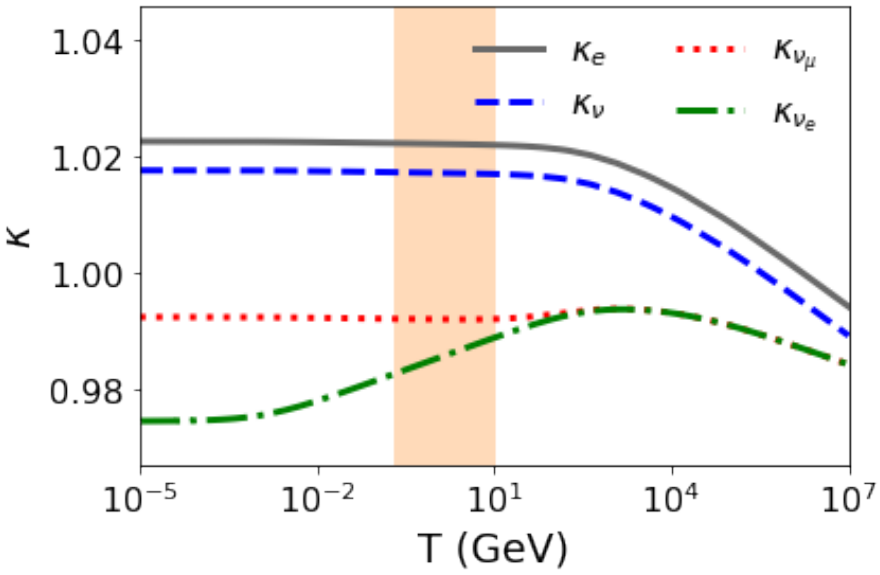

Figure 5.11: The functions κ_e, κ_ν, κ_{ν_μ}, and κ_{ν_e} are illustrated as a function of T (electron recoil energy). The solid gray line corresponds to κ_e; the dashed blue line represents κ_ν, as given by Eq. (5.16); while the dotted red and dot-dashed green lines correspond to κ_{ν_μ} and κ_{ν_e} from Eq. (5.8), respectively. The shaded area indicates the range of T within which a DUNE-ND-like experiment can investigate the impact of radiative corrections and the experimental sensitivity to the neutrino charge radius.

Chapter 6

Conclusions and Future Prospects

Neutrino physics is currently experiencing an exciting era, driven by both present and future experiments that promise to deliver high-statistics data. This data will allow unprecedented accuracy in measuring crucial parameters within the Standard Model. These experiments are not only advancing our understanding of the fundamental properties of neutrinos but also providing vital insights into neutrino-nucleus interactions. These interactions play a significant role in nuclear physics, offering a deeper understanding of the nucleus and its behavior when interacting with other particles, in this case, neutrinos.

This era of neutrino physics is marked by a collaborative effort to extend the boundaries of our knowledge through innovative experiments and cutting-edge technology. The results are expected to have deep implications for our understanding of both the SM and the fundamental nature of neutrino and nuclear interactions. This work presented the analysis of various aspects of neutrino physics and the current advancements in experimental techniques to explore fundamental parameters and phenomena in this field.

The following sections present the conclusions and future perspectives on the experimental analysis of the NuMI ν_μ CC inclusive cross-section measurement and

the study of neutrino-electron scattering phenomenology in a DUNE-PRISM experiment, presented in this work.

6.1 Measurement of the cross-section of the NuMI muon neutrino CC inclusive channel at ICARUS

The ICARUS detector, as the far detector of the SBN program, aims to search for sterile neutrino signatures while offering extensive physics capabilities, including searches beyond the Standard Model (SM) and cross-section measurements. In particular, the measurements of the muon neutrino cross-section from the NuMI beam play a highly relevant role, as the measurements performed at ICARUS will serve as a benchmark for future measurements expected to be performed in the DUNE experiment, given the similar energy ranges of both NuMI in ICARUS and DUNE.

Currently, ICARUS is in its third period of physics-quality data collection. As studied, the reconstruction of events is vital for the analysis, making it imperative to validate the reconstruction process. Validation through cross-checks between visual scans and Pandora software TPC reconstructions has shown good agreement, although several inconsistencies or pathologies have been identified. These pathologies, particularly in muon and proton track studies, are the focus of ongoing research to improve reconstruction quality and reduce systematic errors.

Understanding neutrino-nucleus interactions is essential for both neutrino and nuclear physics. These cross-sections are important for interpreting the results of neutrino experiments and for improving our knowledge of nuclear structure and dynamics. The detailed study of these interactions helps to refine models of the nucleus and provides insights into the fundamental forces at play.

The procedure for measuring the cross-section of the NuMI ν_μ CC inclusive

channel was studied in this work. The next step involves the implementation of the open-source GUNDAM likelihood fitting and cross-section extraction machinery, developed by the T2K collaboration, into the ICARUS framework. This process allows the signal cross-section to vary within predefined truth bins during a simultaneous fit to both the signal and control samples. It includes parameters for each systematic uncertainty, ensuring comprehensive error consideration.

Effective selection of ν_μ CC candidates has been achieved, yielding a sample purity of 74%. Background due to cosmic ray interactions has also been studied, accounting for 16% of the inclusive selection background. Preliminary studies using the CRT-PMT matching tool show significant cosmic ray rejection, and its integration into event selection is being tested.

Unfolding studies have shown good consistency between true and reconstructed MC sample information, though further examination of appropriate bin widths for variables is needed. In the presented work, muon momentum was excluded due to inconsistencies observed in model comparisons. Detailed studies with the multiple Coulomb scattering (MCS) model are ongoing, alongside incorporating the latest detector calibration updates. A study similar to that performed with the $\cos(\theta_{NuMI})$ variable will soon be conducted with muon momentum.

Systematic uncertainties are currently preliminary and conservative. Ongoing efforts aim to understand detector systematics better and improve them. Event selection studies performed in this analysis have validated and improved event reconstruction and particle identification.

6.2 Neutrino-electron scattering

High-statistics data from current and upcoming experiments will enable more precise determinations of fundamental parameters, such as the weak mixing angle and the neutrino charge radius (NCR). These measurements are essential for precision testing

the predictions of the Standard Model (SM) and for probing potential new physics beyond the SM.

The precise determination of radiative corrections at low energies is crucial for testing the SM. Accurate measurements of the weak mixing angle and experimental verification of the NCR are essential. Studies have shown that future near detectors, like those in long-baseline neutrino facilities, are sensitive to radiative corrections in neutrino-electron scattering. Using DUNE-PRISM as an example, the focus has been on the NCR as an effective observable. The primary effect of the NCR is a shift in the weak mixing angle, and the study has investigated the detector's sensitivity to these corrections.

The DUNE-PRISM configuration, with multiple beam angle setups, allows for the analysis of different neutrino energy spectra. The on-axis neutrino spectrum provides a better determination of radiative corrections and potentially the NCR due to higher statistics. With a systematic error of approximately 3%, there are promising prospects for measuring the NCR with an error of the order of 1.5×10^{-33} cm^2.

For a ν_μ beam mode, selecting the appropriate energy window could enable the determination of the NCR's existence, given controlled systematic uncertainties. Conversely, for the $\bar{\nu}_\mu$ mode, the best measurement opportunities are at small electron recoil energy values, suggesting lower thresholds are preferable.

The measurement of neutrino-electron interactions in experiments such as SBND shows promise, with SBND expected to yield substantial event counts. This offers a significant opportunity to measure the neutrino-electron cross-section with precision, providing insights into the weak mixing angle—a fundamental parameter in electroweak theory. While SBND may not match the statistical power of larger experiments like DUNE-PRISM, its ability to yield hundreds of events allows for significant contributions to our understanding of neutrino properties and fundamental

particle physics parameters.

Efforts are also underway to develop computational frameworks and machine learning methodologies for the future DUNE-ND experiment. These tools aim to improve event reconstruction and data analysis efficiency, addressing the complexities of neutrino interactions. By developing these techniques, it is expected to make an estimate with MC simulations on the study of the neutrino-electron interaction in DUNE-ND in the next few years.

Furthermore, the distinct behavior of each κ indicates that measurements over a broader energy range, particularly at low energies where differences are most pronounced, could provide deeper insights into radiative correction effects and the NCR's contribution to standard parameters. Therefore, the follow-up of the phenomenology work will consist of studying neutrino-electron scattering in other neutrino experiments to cover a broader and more complete energy range of this interaction and its implications in the measurement of SM parameters.

Another promising area of neutrino phenomenology is the study of the Heavy Sterile Neutrino Decay model. This model offers a potential solution to the anomalies observed in short-baseline experiments. Ongoing research aims to analyze this model within the context of a DUNE-PRISM-like experiment. This work is currently in progress and is expected to be published soon.

This work underscores the importance of precise measurements in neutrino physics. The ongoing studies and prospects highlight the potential for significant contributions to our understanding of the SM and beyond, driven by innovative techniques and thorough analysis of neutrino interactions. The continuous improvement in event reconstruction, background rejection, and systematic error reduction remains crucial to the success of these efforts.

Appendix A

Neutrino Oscillation in Vacuum

In the standard theory of neutrino oscillations, at $t = 0$ a neutrino characterized by flavor α and momentum $\vec{p}$, originating from a Charged Current interaction involving either a charged lepton l_α^- or an anti-lepton l_α^+, is represented by the *flavor state*

$$|\nu_\alpha\rangle = \sum_k U_{\alpha k}^* |\nu_k\rangle \quad (\alpha = e, \mu, \tau)\,, \tag{A.1}$$

where the flavor states can be one of the active flavor neutrinos: ν_e, ν_μ, ν_τ. The *mass states*, $|\nu_k\rangle$, must be equal to or greater than three: ν_1, ν_2, ν_3, etc.

The unitary mixing matrix, denoted as U, is commonly referred to as the PMNS (Pontecorvo, Maki, Nakagawa, and Sakata) matrix. When dealing with three mass eigenstates and three flavor eigenstates, the matrix U assumes the following form:

$$U = \begin{pmatrix} U_{e1} & U_{e2} & U_{e3} \\ U_{\mu 1} & U_{\mu 2} & U_{\mu 3} \\ U_{\tau 1} & U_{\tau 2} & U_{\tau 3} \end{pmatrix}, \tag{A.2}$$

The PMNS matrix is usually expressed by 3 rotation matrices, in terms of three mixing angles, θ_{12}, θ_{23}, and θ_{13} and a single complex phase δ_{CP}

$$U = \begin{pmatrix} 1 & 0 & 0 \\ 0 & \cos\theta_{23} & \sin\theta_{23} \\ 0 & -\sin\theta_{23} & \cos\theta_{23} \end{pmatrix} \begin{pmatrix} \cos\theta_{13} & 0 & \sin\theta_{13}e^{-i\delta_{CP}} \\ 0 & 1 & 0 \\ -\sin\theta_{13}e^{i\delta_{CP}} & 0 & \cos\theta_{13} \end{pmatrix} \begin{pmatrix} \cos\theta_{12} & \sin\theta_{12} & 0 \\ -\sin\theta_{12} & \cos\theta_{12} & 0 \\ 0 & 0 & 1 \end{pmatrix}, \tag{A.3}$$

The determination of the neutrino mixing angles is achieved through different experiments. The matrix, wherein mixing angle θ_{23} is relevant in experiments involving atmospheric and accelerator neutrinos. Conversely, the matrix containing the mixing angle θ_{12} is associated principally with neutrino oscillations observed in solar experiments. A matrix of pivotal importance termed the cross-mixing matrix, incorporates two parameters: the mixing angle θ_{13} and the CP-violating phase δ_{CP}. This matrix plays an important role in experiments involving reactor and accelerator neutrinos.

The introduction of non-zero δ_{CP} results in a complex unitary matrix U and imparts distinct probabilities to CP-conjugate oscillations, denoted as $P(\nu_\alpha \to \nu_\beta) \neq P(\bar{\nu}_\alpha \to \bar{\nu}_\beta)$. Such a discrepancy in probabilities constitutes a significant discovery with implications for our understanding of neutrino physics.

Now, if we consider the time evolution of a flavor state is

$$|\nu_\alpha(t)\rangle = \sum_k U^*_{\alpha k} e^{-iE_k t} |\nu_k\rangle \,, \tag{A.4}$$

then considering the unitary relation of the U matrix

$$U^\dagger U = 1 \iff \sum_\alpha U^*_{\alpha k} U_{\alpha j} = \delta_{jk} \,, \tag{A.5}$$

with this, we will have

$$|\nu_k\rangle = \sum_\alpha U_{\alpha k} |\nu_\alpha\rangle \,. \tag{A.6}$$

If we substitute this relation into the expression for the time evolution of a flavor state Eq. (A.4), we get

$$|\nu_\alpha(t)\rangle = \sum_{\beta=e,\mu,\tau} \left(\sum_k U^*_{\alpha k} e^{-iE_k t} U_{\beta k} \right) |\nu_\beta\rangle \,, \tag{A.7}$$

with this, the amplitude of $\nu_\alpha \to \nu_\beta$ transition as a function of time is

$$A_{\nu_\alpha \to \nu_\beta}(t) \equiv \langle \nu_\beta | \nu_\alpha(t) \rangle = \sum_k U^*_{\alpha k} U_{\beta k} e^{-iE_k t}. \tag{A.8}$$

Then the transition probability is

$$P_{\nu_\alpha \to \nu_\beta}(t) = |A_{\nu_\alpha \to \nu_\beta}(t)|^2 = \sum_{k,j} U^*_{\alpha k} U_{\beta k} U_{\alpha j} U^*_{\beta j} e^{-i(E_k - E_j)t}. \tag{A.9}$$

From the dispersion relation $E_k = \sqrt{\vec{p}^2 + m_k^2}$, for ultra-relativistic neutrinos we can approximate

$$E_k \simeq E + \frac{m_k^2}{2E} \,, \tag{A.10}$$

where we can consider $E = |\vec{p}|$. Thus, we have

$$E_k - E_j \simeq \frac{\Delta m^2_{kj}}{2E} \,, \tag{A.11}$$

where $\Delta m^2_{kj} \equiv m^2_k - m^2_j$ is the difference in masses between the neutrino mass states.

Since ultra-relativistic neutrinos propagate almost at the speed of light, it is possible to approximate $t \sim L$, where L is the distance between the source and the detector:

$$P_{\nu_\alpha \to \nu_\beta}(L, E) = \sum_{k,j} U^*_{\alpha k} U_{\beta k} U_{\alpha j} U^*_{\beta j} \exp -i \frac{\Delta m^2_{kj} L}{2E}. \tag{A.12}$$

Considering the unitary relation, given by the Eq. (A.5) we have for $L = 0$, the transition probability is

$$P_{\nu_\alpha \to \nu_\beta}(L = 0, E) = \delta_{\alpha\beta}\,, \tag{A.13}$$

this means that a transition between flavors manifests only for $L > 0$.

Another form to write the transition probability is separating the product of the U elements in its real and imaginary parts:

$$P_{\nu_\alpha \to \nu_\beta}(L, E) = \delta_{\alpha\beta} - 4 \sum_{k>j} \Re e \left[U^*_{\alpha k} U_{\beta k} U_{\alpha j} U^*_{\beta j} \right] \sin^2 \left(\frac{\Delta m^2_{kj} L}{4E} \right) \tag{A.14}$$

$$+ 2 \sum_{k>j} \Im m \left[U^*_{\alpha k} U_{\beta k} U_{\alpha j} U^*_{\beta j} \right] \sin \left(\frac{\Delta m^2_{kj} L}{2E} \right)\,, \tag{A.15}$$

It is worth noting that matter effects differ for neutrinos and antineutrinos, and these differences must be considered in genuine CP violation searches.

Appendix B

Cosmic rays production

In many experiments, such as ICARUS, MicroBooNE, etc., as they are surface detectors, cosmic rays are a significant source of background that must be studied to ensure the reliability of the physical measurements being made.

In this appendix we will study cosmic ray production and the impact of cosmic ray interactions on our detectors.

B.1 Cosmic rays

The cosmic ray cascade consists of a series of decays that occur when cosmic rays of galactic or extragalactic origin interact with our atmosphere. The primary particles that initiate this cascade include protons, light nuclei up to iron, and photons, among others. These primary particles travel through the atmosphere until they react with air nuclei or, in the case of unstable secondary particles, disintegrate. The cosmic ray cascade has three main components: the electromagnetic component (comprising electrons $e^{\pm}$ and photons γ), the muonic component (comprising muons $\mu^{\pm}$ coming from the decay of charged mesons, typically $\pi^{\pm}$ and $K^{\pm}$), and the hadronic component (comprising hadrons, nucleons, and some light nuclei). In

our study of the ν_μ CC inclusive channel, the muonic component constitutes the primary source of background.

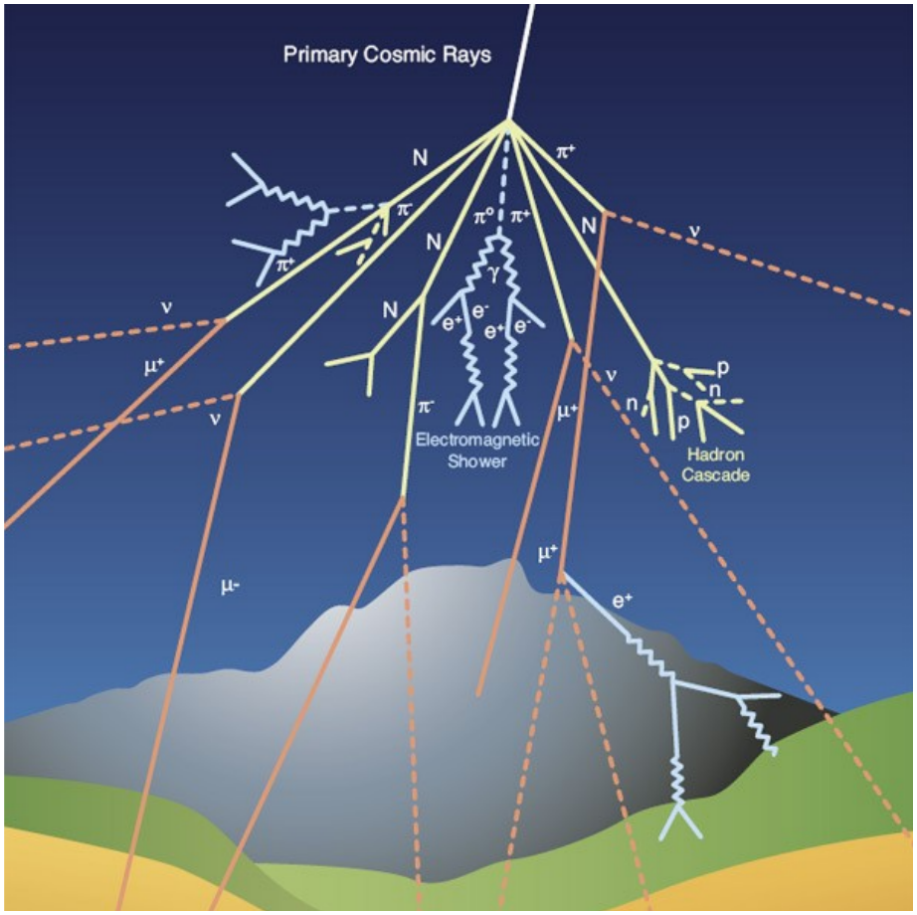

Figure B.1: Cosmic rays cascade [126]

Appendix C

QED corrections

In this appendix, we show the explicit form of the functions $f_{-}(z)$, $f_{+}(z)$, and $f_{+-}(z)$ that are introduced in Eq. (5.5). We consider the expressions given in Ref. [114] (numerical expressions can be found in Ref. [115]) and that for the case of $f_{-}(z)$ is

$$\begin{aligned} f_{-}(z) = & \left[\frac{E}{l}\ln\left(\frac{E+l}{m_e}\right) - 1\right]\left[2\ln\left(1 - z - \frac{m_e}{E+l}\right) - \ln(1-z) - \frac{1}{2}\ln z - \frac{5}{12}\right] \\ & + \frac{1}{2}\left[L(z) - L(\beta)\right] - \frac{1}{2}\ln^2(1-z) - \left(\frac{11}{12} + \frac{z}{2}\right)\ln(1-z) \\ & + z\left[\ln z + \frac{1}{2}\ln\left(\frac{2E_\nu}{m_e}\right)\right] - \left(\frac{31}{18} + \frac{1}{12}\ln z\right)\beta - \frac{11}{12}z + \frac{z^2}{24}\,, \end{aligned} \tag{C.1}$$

where $l = \sqrt{E^2 - m_e^2}$ is the three-momentum of the electron, $E = T + m_e$, $\beta = l/E$, and $L(x)$ is in Spence's function space corresponding to the following dilogarithm:

$$L(x) = -Li_2(x) = \int_0^x \frac{\ln|1-t|}{t} dt\,. \tag{C.2}$$

Figure C.1 shows the trend followed by the function $f_{-}(z)$ for different values of the incident neutrino energy E_ν.

The $f_{+}(z)$ function (illustrated by the figure C.2) is given by:

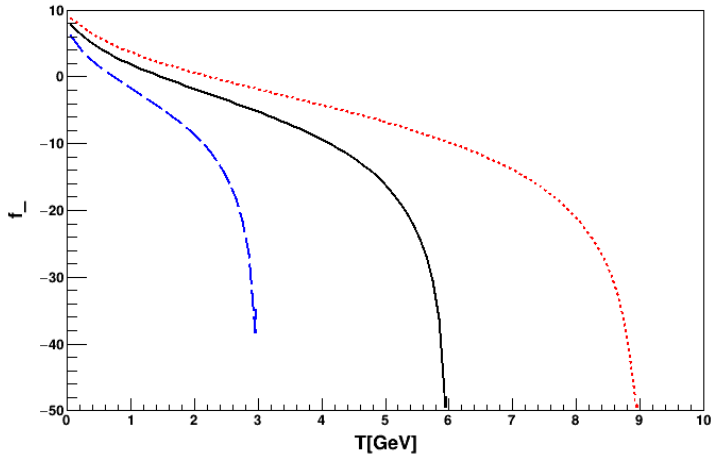

Figure C.1: Function $f_{-}(z)$ in terms of T for different incident neutrino energies (E_ν). The dashed blue line is for $E_\nu = 3$ GeV, the solid black line is for $E_\nu = 6$ GeV, and the dotted red line is for $E_\nu = 9$ GeV.

$$
\begin{aligned}
(1-z)^2 f_{+}(z) = & \left[\frac{E}{l}\ln\left(\frac{E+l}{m_e}\right)-1\right]\left\{(1-z)^2\left[2\ln\left(1-z-\frac{m_e}{E+l}\right)\right.\right. \\
& \left.\left.-\ln(1-z)-\frac{1}{2}\ln z-\frac{2}{3}\right]-\frac{z^2\ln z+1-z}{2}\right\} \\
& -\frac{(1-z)^2}{2}\left\{\ln^2(1-z)+\beta\left[L(1-z)-\ln z\ln(1-z)\right]\right\} \\
& +\ln(1-z)\left[\frac{z^2}{2}\ln z+\frac{1-z}{3}\left(2z-\frac{1}{2}\right)\right]-\frac{z^2}{2}L(1-z) \\
& -\frac{z(1-2z)}{3}\ln z-\frac{z(1-z)}{6} \\
& -\frac{\beta}{12}\left[\ln z+(1-z)\left(\frac{115-109z}{6}\right)\right], \qquad \text{(C.3)}
\end{aligned}
$$

and the $f_{+-}(z)$ function (illustrated by the figure C.3) is:

$$
f_{+-}(z) = \left[\frac{E}{l}\ln\left(\frac{E+l}{m_e}\right)-1\right]2\ln\left(1-z-\frac{m_e}{E+l}\right). \qquad \text{(C.4)}
$$

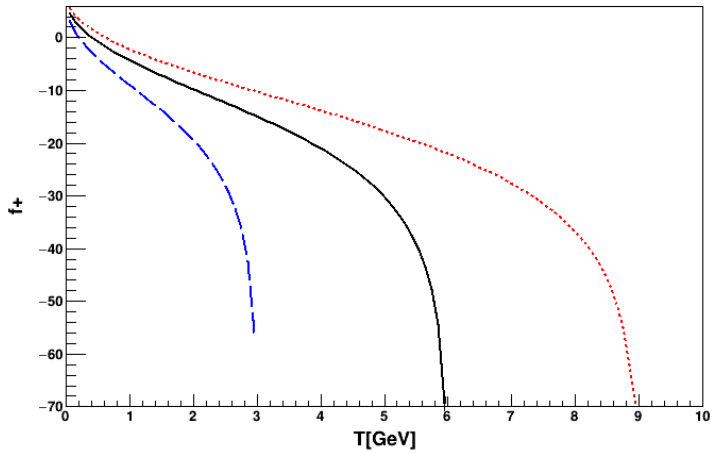

Figure C.2: Function $f_+(z)$ in terms of T for different incident neutrino energies (E_ν). The dashed blue line is for $E_\nu = 3$ GeV, the solid black line is for $E_\nu = 6$ GeV, and the dotted red line is for $E_\nu = 9$ GeV.

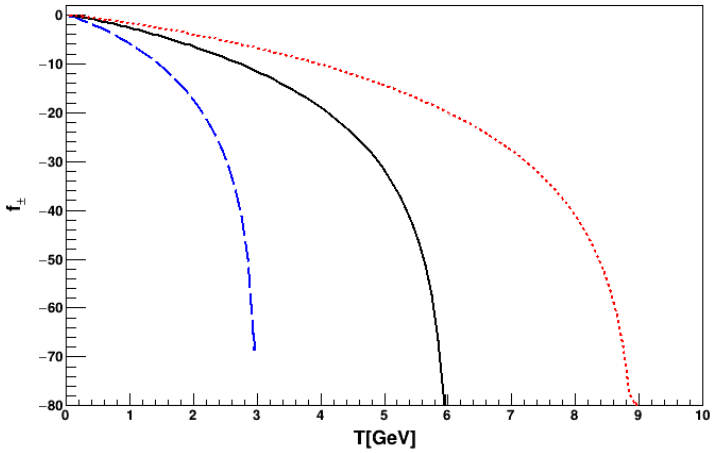

Figure C.3: Function $f_\pm(z)$ in terms of T for different incident neutrino energies (E_ν). The dashed blue line is for $E_\nu = 3$ GeV, the solid black line is for $E_\nu = 6$ GeV, and the dotted red line is for $E_\nu = 9$ GeV.

Appendix D

Analysis for radiative corrections and neutrino charge radius at several DUNE-PRISM off-axis fluxes

In this appendix, we present the analysis of the sensitivity of DUNE-PRISM to radiative corrections, with a particular focus on the Neutrino Charge Radius (NCR), for the most off-axis fluxes of the neutrino beam. The main objective is to provide a detailed account of the computed number of events in neutrino-electron scattering scenarios, shedding light on the impact of radiative corrections, and discerning the nuanced contributions of the NCR.

The computations delve into various off-axis beam angles, facilitating the identification of optimal angular windows and energy ranges crucial for achieving heightened sensitivity to radiative corrections. By emphasizing the most off-axis fluxes, this analysis aims to capture and scrutinize the distinctive features of the beam that are essential for understanding and measuring the NCR effect.

The results presented herein contribute valuable insights into the experimental capabilities of DUNE-PRISM, offering a nuanced perspective on its potential for

precise measurements of radiative corrections, and specifically, the NCR, within the context of the most extreme off-axis flux configurations.

D.1 Fluxes off-axis

Figure 1 shows the different on-axis and off-axis fluxes expected for the DUNE-PRISM detector. These fluxes range from the on-axis case, 0°, to the 3.6°off-axis case.

It is worth noting that the greater the off-axis angle, the narrower the flux distribution (spike) becomes, with lower energy values.

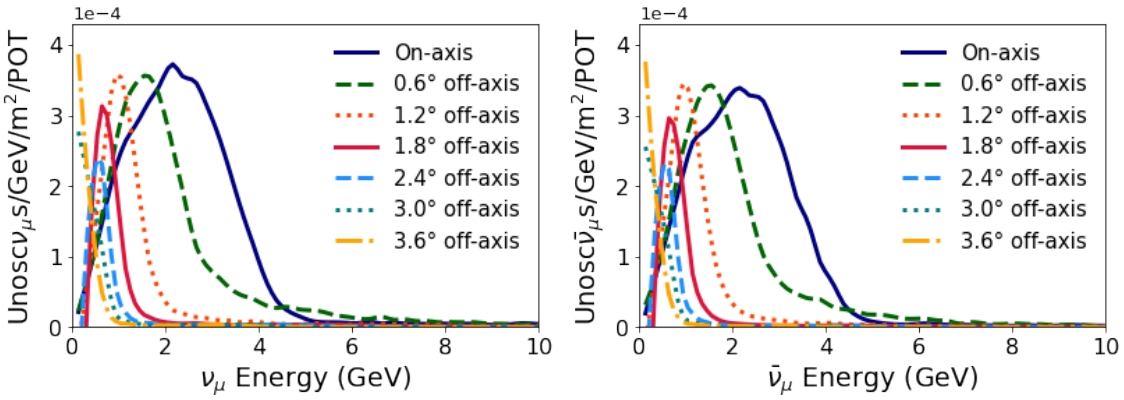

(a) ν_μ beam mode

(b) $\bar{\nu}_\mu$ beam mode

Figure D.1: Fluxes at several off-axis locations [124]. Neutrino mode (a), on the left side, and antineutrino mode (b), on the right side.

D.2 Number of Events

The number of events obtained for each on-axis and off-axis case is shown below.

D.2.1 Anti-neutrino mode

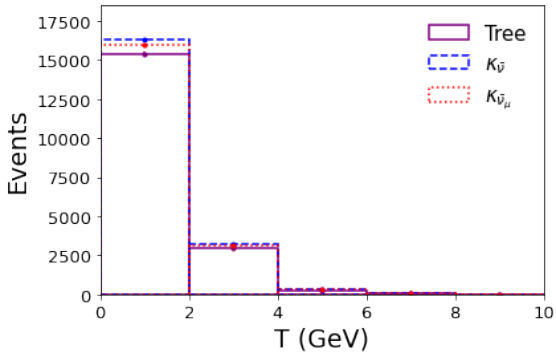

(a) On-axis

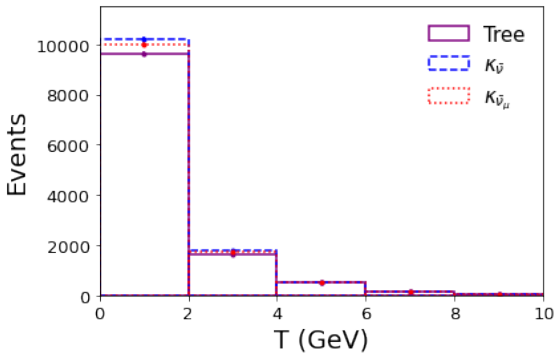

(b) 0.6° off-axis

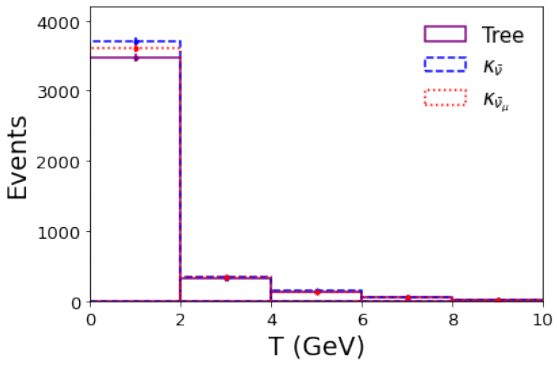

(c) 1.2° off-axis

Figure D.2: Comparison among the number of $\bar{\nu}_\mu$ event expectations at tree-level (solid black line) and considering radiative corrections, with and without neutrino charge radius (dashed red and dot-dashed blue line, respectively). We show two DUNE-PRISM spectra: (a) On axis on the top, (b) 0.6° on the left, and (c) 1.2° on the right side.

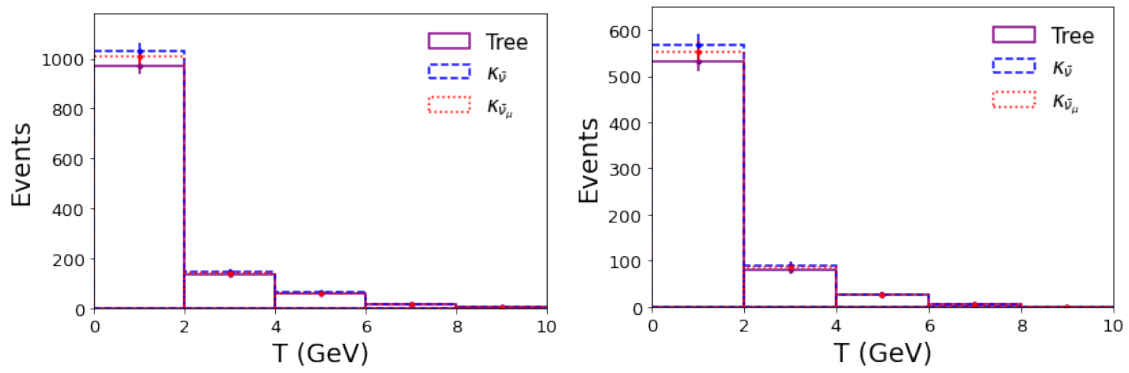

(a) 1.8° off-axis (b) 2.4° off-axis

Figure D.3: Comparison among the number of $\bar{\nu}_\mu$ event expectations at tree-level (solid black line) and considering radiative corrections, with and without neutrino charge radius (dashed red and dot-dashed blue line, respectively). We show two DUNE-PRISM spectra: (a) 1.8° on the left and (b) 2.4° on the right side.

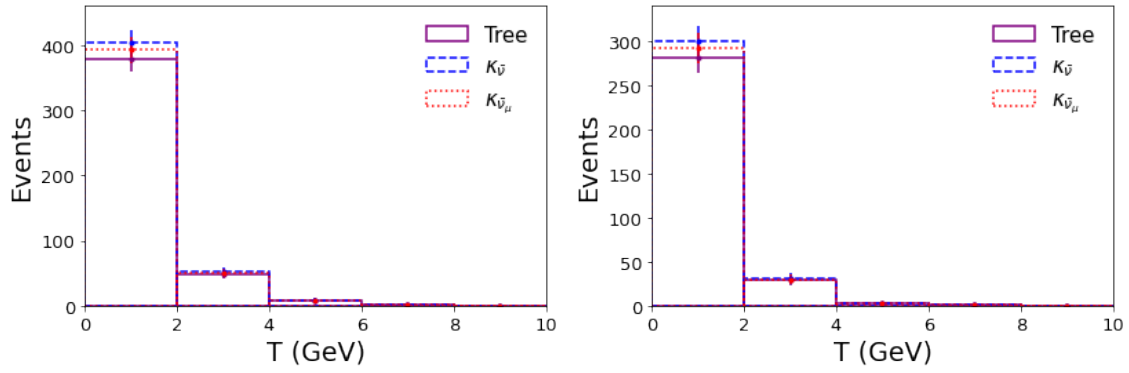

(a) 3.0° off-axis (b) 3.6° off-axis

Figure D.4: Comparison among the number of $\bar{\nu}_\mu$ event expectations at tree-level (solid black line) and considering radiative corrections, with and without neutrino charge radius (dashed red and dot-dashed blue line, respectively). We show two DUNE-PRISM spectra: (a) 3.0° on the left and (b) 3.6° on the right side.

D.2.2 Neutrino mode

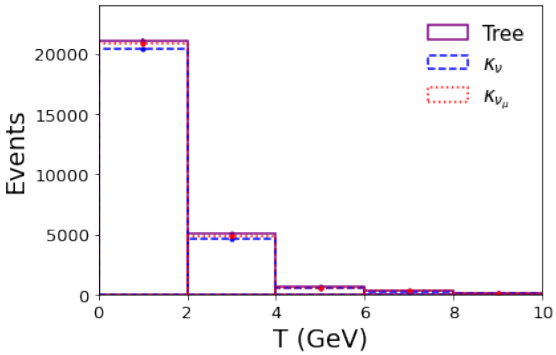

(a) On-axis

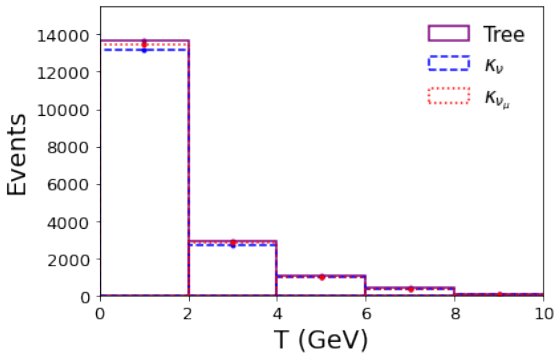

(b) 0.6° off-axis

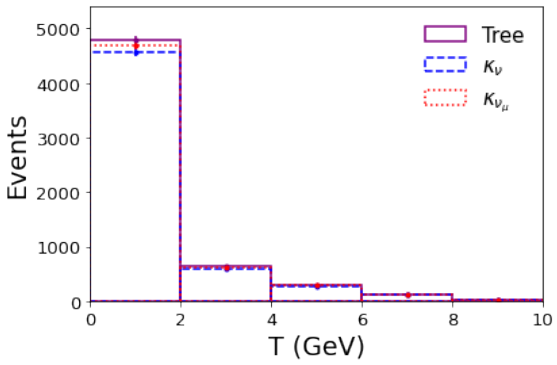

(c) 1.2° off-axis

Figure D.5: Comparison among the number of ν_μ event expectations at tree-level (solid black line) and considering radiative corrections, with and without neutrino charge radius (dashed red and dot-dashed blue line, respectively). We show two DUNE-PRISM spectra: (a) On axis on the top, (b) 0.6° on the left, and (c) 1.2° on the right side.

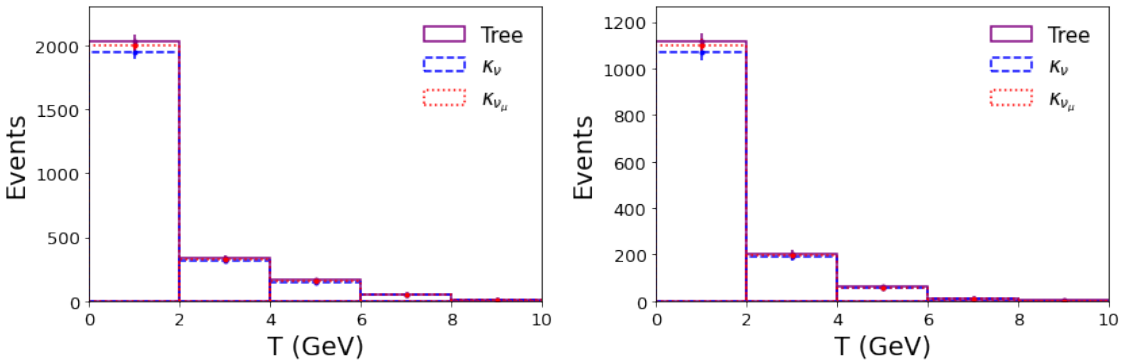

(a) 1.8° off-axis (b) 2.4° off-axis

Figure D.6: Comparison among the number of ν_μ event expectations at tree-level (solid black line) and considering radiative corrections, with and without neutrino charge radius (dashed red and dot-dashed blue line, respectively). We show two DUNE-PRISM spectra: (a) 1.8° on the left and (b) 2.4° on the right side.

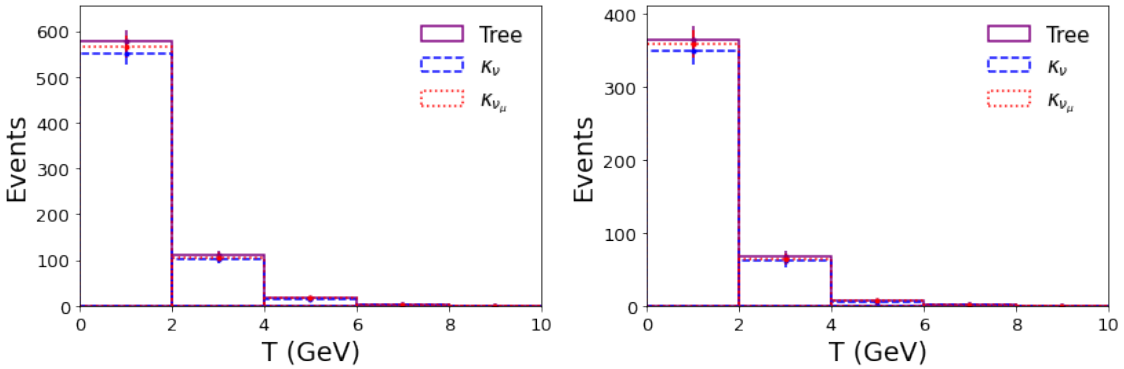

(a) 3.0° off-axis (b) 3.6° off-axis

Figure D.7: Comparison among the number of ν_μ event expectations at tree-level (solid black line) and considering radiative corrections, with and without neutrino charge radius (dashed red and dot-dashed blue line, respectively). We show two DUNE-PRISM spectra: (a) 3.0° on the left and (b) 3.6° on the right side.

It is noted that the on-axis case shows the greatest difference between the number of events at tree level and the next leading order cases.

Published Articles

Published Articles

1. O. G. Miranda, G. Moreno-Granados and C. A. Moura, "Sensitivity of accelerator based neutrino experiments to neutrino-electron scattering radiative corrections", Phys. Rev. D 104, 013007 (2021).

   [Extension of my M.Sc. dissertation work.]

2. Abratenko, P. et al. ICARUS at the Fermilab Short-Baseline Neutrino program: initial operation. Eur. Phys. J. C 83, 467 (2023).

   [My contribution consisted in validating the reconstruction of the first neutrino interactions in ICARUS. This work is shown in Figure 35.]

3. L. Bagby et al. [ICARUS], "Overhaul and Installation of the ICARUS-T600 Liquid Argon TPC Electronics for the FNAL Short Baseline Neutrino Program", JINST 16, P01037(2021).

   [Part of my participation in the ICARUS commissioning activities, testing TPC electronics and detector chimneys.]

Proceedings

1. O. G. Miranda, G. Moreno-Granados and C. A. Moura, "ν-e Scattering radiative corrections in a short baseline experiment", Rev.Mex.Fis.Suppl. 3 (2022) 2, 020711.

In progress

1. G. Moreno-Granados, P. Roy, M. Betancourt, S. Dolan, "Technical note: muon neutrino CC inclusive channel with the off-axis NuMI beam at ICARUS".

2. Luis A. Delgadillo, O. G. Miranda, G. Moreno-Granados and C. A. Moura, "Limits from a long-baseline neutrino experiment on $CPT-$odd coefficients of the Standard Model Extension".

3. Sabya Sachi Chatterjee, Stéphane Lavignac, O. G. Miranda, and G. Moreno-Granados, "Sterile neutrino decay at a NuMI Fermilab near detector".

Bibliography

[1] A. Aguilar *et al.*, "Evidence for neutrino oscillations from the observation of $\bar{\nu}_e$ appearance in a $\bar{\nu}_\mu$ beam," *Phys. Rev. D*, vol. 64, p. 112007, 2001.

[2] A. A. Aguilar-Arevalo *et al.*, "Significant Excess of ElectronLike Events in the MiniBooNE Short-Baseline Neutrino Experiment," *Phys. Rev. Lett.*, vol. 121, no. 22, p. 221801, 2018.

[3] P. A. Machado, O. Palamara, and D. W. Schmitz, "The Short-Baseline Neutrino Program at Fermilab," *Ann. Rev. Nucl. Part. Sci.*, vol. 69, pp. 363–387, 2019.

[4] V. A. Naumov and D. S. Shkirmanov, "Reactor antineutrino anomaly reanalysis in context of inverse-square law violation," *Universe*, vol. 7, no. 7, 2021.

[5] P. Abratenko *et al.*, "ICARUS at the Fermilab Short-Baseline Neutrino program: initial operation," *Eur. Phys. J. C*, vol. 83, no. 6, p. 467, 2023.

[6] W. Pauli, "Dear radioactive ladies and gentlemen," *Phys. Today*, vol. 31N9, p. 27, 1978.

[7] W. Pauli, "On the Earlier and more recent history of the neutrino," *Camb. Monogr. Part. Phys. Nucl. Phys. Cosmol.*, vol. 14, pp. 1–22, 2000.

[8] J. Chadwick, "The Existence of a Neutron," *Proc. Roy. Soc. Lond. A*, vol. 136, no. 830, pp. 692–708, 1932.

[9] E. Fermi, "An attempt of a theory of beta radiation. 1.," *Z. Phys.*, vol. 88, pp. 161–177, 1934.

[10] G. Gamow and E. Teller, "Selection rules for the beta-disintegration," *Phys. Rev.*, vol. 49, pp. 895–899, 1936.

[11] C. Giunti and C. W. Kim, *Fundamentals of Neutrino Physics and Astrophysics*. Oxford University Press, 2007.

[12] B. Pontecorvo, "Electron and Muon Neutrinos," *Zh. Eksp. Teor. Fiz.*, vol. 37, pp. 1751–1757, 1959.

[13] F. Reines and C. L. Cowan, "Detection of the free neutrino," *Phys. Rev.*, vol. 92, pp. 830–831, 1953.

[14] S. L. Glashow, "Partial Symmetries of Weak Interactions," *Nucl. Phys.*, vol. 22, pp. 579–588, 1961.

[15] S. Weinberg, "A Model of Leptons," *Phys. Rev. Lett.*, vol. 19, pp. 1264–1266, 1967.

[16] A. Salam, "Weak and Electromagnetic Interactions," *Conf. Proc. C*, vol. 680519, pp. 367–377, 1968.

[17] A. de Gouvea, "The neutrino mass puzzle," *CERN Cour.*, vol. 64, no. 3, pp. 29–33, 2024.

[18] C.-S. Wu, "The discovery of the parity violation in weak interactions and its recent developments," *Lect. Notes Phys.*, vol. 746, pp. 43–70, 2008.

[19] M. Goldhaber, L. Grodzins, and A. W. Sunyar, "Helicity of Neutrinos," *Phys. Rev.*, vol. 109, pp. 1015–1017, 1958.

[20] M. Thomson, *Modern Particle Physics*. Cambridge University Press, 2013.

[21] P. A. Zyla *et al.*, "Review of Particle Physics," *PTEP*, vol. 2020, no. 8, p. 083C01, 2020.

[22] B. Pontecorvo, "Inverse beta processes and nonconservation of lepton charge," *Zh. Eksp. Teor. Fiz.*, vol. 34, p. 247, 1957.

[23] Z. Maki, M. Nakagawa, and S. Sakata, "Remarks on the unified model of elementary particles," *Prog. Theor. Phys.*, vol. 28, pp. 870–880, 1962.

[24] R. Davis, Jr., D. S. Harmer, and K. C. Hoffman, "Search for neutrinos from the sun," *Phys. Rev. Lett.*, vol. 20, pp. 1205–1209, 1968.

[25] F. Bergsma *et al.*, "A Search for Neutrino Oscillations," *Z. Phys. C*, vol. 40, p. 171, 1988.

[26] P. Astier *et al.*, "Search for nu(mu) —> nu(e) oscillations in the NOMAD experiment," *Phys. Lett. B*, vol. 570, pp. 19–31, 2003.

[27] A. A. Aguilar-Arevalo *et al.*, "A Search for Electron Neutrino Appearance at the $\Delta m^2 \sim 1eV^2$ Scale," *Phys. Rev. Lett.*, vol. 98, p. 231801, 2007.

[28] L. Mellet, "Latest Neutrino Oscillation Results from T2K," *PoS*, vol. TAUP2023, p. 204, 2024.

[29] P. Adamson *et al.*, "Improved search for muon-neutrino to electron-neutrino oscillations in MINOS," *Phys. Rev. Lett.*, vol. 107, p. 181802, 2011.

[30] Y. Fukuda *et al.*, "Evidence for oscillation of atmospheric neutrinos," *Phys. Rev. Lett.*, vol. 81, pp. 1562–1567, 1998.

[31] Y. Ashie *et al.*, "Evidence for an oscillatory signature in atmospheric neutrino oscillation," *Phys. Rev. Lett.*, vol. 93, p. 101801, 2004.

[32] M. A. Acero *et al.*, "Improved measurement of neutrino oscillation parameters by the NOvA experiment," *Phys. Rev. D*, vol. 106, no. 3, p. 032004, 2022.

[33] K. Abe *et al.*, "Hyper-Kamiokande Design Report," 5 2018.

[34] B. Abi *et al.*, "Deep Underground Neutrino Experiment (DUNE), Far Detector Technical Design Report, Volume I Introduction to DUNE," *JINST*, vol. 15, no. 08, p. T08008, 2020.

[35] B. Abi *et al.*, "Deep Underground Neutrino Experiment (DUNE), Far Detector Technical Design Report, Volume II: DUNE Physics," *FERMILAB-PUB-20-025-ND, FERMILAB-DESIGN-2020-02*, 2 2020.

[36] J. N. Bahcall, N. A. Bahcall, and R. K. Ulrich, "Sensitivity of the Solar-Neutrino Fluxes," *Astrophys. J.*, vol. 156, pp. 559–568, 1969.

[37] J. N. Bahcall, W. F. Huebner, S. H. Lubow, P. D. Parker, and R. K. Ulrich, "Standard Solar Models and the Uncertainties in Predicted Capture Rates of Solar Neutrinos," *Rev. Mod. Phys.*, vol. 54, p. 767, 1982.

[38] J. Boger *et al.*, "The Sudbury neutrino observatory," *Nucl. Instrum. Meth. A*, vol. 449, pp. 172–207, 2000.

[39] M. G. Aartsen *et al.*, "Observation of High-Energy Astrophysical Neutrinos in Three Years of IceCube Data," *Phys. Rev. Lett.*, vol. 113, p. 101101, 2014.

[40] K. Eguchi *et al.*, "First results from KamLAND: Evidence for reactor anti-neutrino disappearance," *Phys. Rev. Lett.*, vol. 90, p. 021802, 2003.

[41] S. Abe *et al.*, "Precision Measurement of Neutrino Oscillation Parameters with KamLAND," *Phys. Rev. Lett.*, vol. 100, p. 221803, 2008.

[42] B. T. Cleveland, T. Daily, R. Davis, Jr., J. R. Distel, K. Lande, C. K. Lee, P. S. Wildenhain, and J. Ullman, "Measurement of the solar electron neutrino flux with the Homestake chlorine detector," *Astrophys. J.*, vol. 496, pp. 505–526, 1998.

[43] W. Hampel *et al.*, "Final results of the Cr-51 neutrino source experiments in GALLEX," *Phys. Lett. B*, vol. 420, pp. 114–126, 1998.

[44] J. N. Abdurashitov *et al.*, "Measurement of the response of the Russian-American gallium experiment to neutrinos from a Cr-51 source," *Phys. Rev. C*, vol. 59, pp. 2246–2263, 1999.

[45] K. S. Hirata *et al.*, "Experimental Study of the Atmospheric Neutrino Flux," *Phys. Lett. B*, vol. 205, p. 416, 1988.

[46] Q. R. Ahmad *et al.*, "Direct evidence for neutrino flavor transformation from neutral current interactions in the Sudbury Neutrino Observatory," *Phys. Rev. Lett.*, vol. 89, p. 011301, 2002.

[47] T. Kajita, "Nobel Lecture: Discovery of atmospheric neutrino oscillations," *Rev. Mod. Phys.*, vol. 88, no. 3, p. 030501, 2016.

[48] A. B. McDonald, "Nobel Lecture: The Sudbury Neutrino Observatory: Observation of flavor change for solar neutrinos," *Rev. Mod. Phys.*, vol. 88, no. 3, p. 030502, 2016.

[49] R. Acciarri *et al.*, "A Proposal for a Three Detector Short-Baseline Neutrino Oscillation Program in the Fermilab Booster Neutrino Beam," 3 2015.

[50] A. A. Aguilar-Arevalo *et al.*, "Unexplained Excess of Electron-Like Events From a 1-GeV Neutrino Beam," *Phys. Rev. Lett.*, vol. 102, p. 101802, 2009.

[51] A. A. Aguilar-Arevalo *et al.*, "A Search for Electron Antineutrino Appearance at the $\Delta m^2 \sim 1$ eV^2 Scale," *Phys. Rev. Lett.*, vol. 103, p. 111801, 2009.

[52] A. A. Aguilar-Arevalo *et al.*, "Improved Search for $\bar{\nu}_\mu \to \bar{\nu}_e$ Oscillations in the MiniBooNE Experiment," *Phys. Rev. Lett.*, vol. 110, p. 161801, 2013.

[53] R. Acciarri *et al.*, "Design and Construction of the MicroBooNE Detector," *JINST*, vol. 12, no. 02, p. P02017, 2017.

[54] G. Mention, M. Fechner, T. Lasserre, T. A. Mueller, D. Lhuillier, M. Cribier, and A. Letourneau, "The Reactor Antineutrino Anomaly," *Phys. Rev. D*, vol. 83, p. 073006, 2011.

[55] T. A. Mueller *et al.*, "Improved Predictions of Reactor Antineutrino Spectra," *Phys. Rev. C*, vol. 83, p. 054615, 2011.

[56] P. Huber, "On the determination of anti-neutrino spectra from nuclear reactors," *Phys. Rev. C*, vol. 84, p. 024617, 2011. [Erratum: Phys.Rev.C 85, 029901 (2012)].

[57] A. C. Hayes, J. L. Friar, G. T. Garvey, G. Jungman, and G. Jonkmans, "Systematic Uncertainties in the Analysis of the Reactor Neutrino Anomaly," *Phys. Rev. Lett.*, vol. 112, p. 202501, 2014.

[58] C. Zhang, X. Qian, and M. Fallot, "Reactor antineutrino flux and anomaly," *Prog. Part. Nucl. Phys.*, vol. 136, p. 104106, 2024.

[59] E. Di Valentino, S. Gariazzo, and O. Mena, "Neutrinos in Cosmology," 4 2024.

[60] A. A. Aguilar-Arevalo *et al.*, "Testing meson portal dark sector solutions to the MiniBooNE anomaly at the Coherent CAPTAIN Mills experiment," *Phys. Rev. D*, vol. 109, no. 9, p. 095017, 2024.

[61] M. Dentler, I. Esteban, J. Kopp, and P. Machado, "Decaying Sterile Neutrinos and the Short Baseline Oscillation Anomalies," *Phys. Rev. D*, vol. 101, no. 11, p. 115013, 2020.

[62] A. de Gouvêa, O. L. G. Peres, S. Prakash, and G. V. Stenico, "On The Decaying-Sterile Neutrino Solution to the Electron (Anti)Neutrino Appearance Anomalies," *JHEP*, vol. 07, p. 141, 2020.

[63] J. A. Formaggio and G. P. Zeller, "From eV to EeV: Neutrino Cross Sections Across Energy Scales," *Rev. Mod. Phys.*, vol. 84, pp. 1307–1341, 2012.

[64] A. Aduszkiewicz, D. Cherdak, and A. Wood, "Prediction of numi electron and muon neutrino flux in icarus." `https://sbn-docdb.fnal.gov/cgi-bin/sso/ShowDocument?docid=27384`.

[65] C. Rubbia, "The Liquid Argon Time Projection Chamber: A New Concept for Neutrino Detectors," *CERN-EP-INT-77-08, CERN-EP-77-08*, 5 1977.

[66] M. Nebot-Guinot, "Status of the Short-Baseline Near Detector at Fermilab," *Phys. Sci. Forum*, vol. 8, no. 1, p. 22, 2023.

[67] A. Ereditato and A. Rubbia, "The Liquid argon TPC: A Powerful detector for future neutrino experiments and proton decay searches," *Nucl. Phys. B Proc. Suppl.*, vol. 154, pp. 163–178, 2006.

[68] M. Antonello, "ArgoNeuT and MicroBooNE: LAr-TPC's at Fermilab," *AIP Conf. Proc.*, vol. 1222, no. 1, pp. 257–261, 2010.

[69] M. Convery, M. Lindgren, S. Nagaitsev, and V. Shiltsev, "Fermilab accelerator complex: Status and improvement plans," *FERMILAB-TM-2693-AD 1748441*, vol. 53, 12 2018.

[70] Fermilab, "Fermilab's accelerator complex." https://www.fnal.gov/pub/science/particle-accelerators/accelerator-complex.html.

[71] P. Adamson *et al.*, "The NuMI Neutrino Beam," *Nucl. Instrum. Meth. A*, vol. 806, pp. 279–306, 2016.

[72] M. Antonello *et al.*, "Search for anomalies in the ν_e appearance from a ν_μ beam," *Eur. Phys. J. C*, vol. 73, p. 2599, 2013.

[73] S. Amerio *et al.*, "Design, construction and tests of the ICARUS T600 detector," *Nucl. Instrum. Meth. A*, vol. 527, pp. 329–410, 2004.

[74] FERMILAB, "Icarus." https://icarus.fnal.gov/detector/.

[75] L. Bagby *et al.*, "Overhaul and Installation of the ICARUS-T600 Liquid Argon TPC Electronics for the FNAL Short Baseline Neutrino Program," *JINST*, vol. 16, no. 01, p. P01037, 2021.

[76] J. S. Marshall and M. A. Thomson, "The Pandora Software Development Kit for Pattern Recognition," *Eur. Phys. J. C*, vol. 75, no. 9, p. 439, 2015.

[77] R. Acciarri *et al.*, "The Pandora multi-algorithm approach to automated pattern recognition of cosmic-ray muon and neutrino events in the MicroBooNE detector," *Eur. Phys. J. C*, vol. 78, no. 1, p. 82, 2018.

[78] T. E. o. E. Britannica, "delta ray." https://www.britannica.com/science/delta-ray.

[79] C. Adams and M. Del Tutto, "TITUS: Visualization of Neutrino Events in Liquid Argon Time Projection Chambers," *Instruments*, vol. 4, no. 4, p. 31, 2020.

[80] K. Yonehara, S. Ganguly, D. A. Wickremasinghe, P. Snopok, and Y. Yu, "Exploring the Focusing Mechanism of the NuMI Horn Magnets," *FERMILAB-PUB-23-169-AD*, 5 2023.

[81] Y. Nakajima *et al.*, "Measurement of Inclusive Charged Current Interactions on Carbon in a Few-GeV Neutrino Beam," *Phys. Rev. D*, vol. 83, p. 012005, 2011.

[82] Q. Wu *et al.*, "A Precise measurement of the muon neutrino-nucleon inclusive charged current cross-section off an isoscalar target in the energy range 2.5 < E(nu) < 40-GeV by NOMAD," *Phys. Lett. B*, vol. 660, pp. 19–25, 2008.

[83] P. Adamson *et al.*, "Neutrino and Antineutrino Inclusive Charged-current Cross Section Measurements with the MINOS Near Detector," *Phys. Rev. D*, vol. 81, p. 072002, 2010.

[84] L. Ren *et al.*, "Measurement of the antineutrino to neutrino charged-current interaction cross section ratio in MINERvA," *Phys. Rev. D*, vol. 95, no. 7, p. 072009, 2017. [Addendum: Phys.Rev.D 97, 019902 (2018)].

[85] K. Abe *et al.*, "Measurement of the inclusive ν_μ charged current cross section on carbon in the near detector of the T2K experiment," *Phys. Rev. D*, vol. 87, no. 9, p. 092003, 2013.

[86] C. Anderson *et al.*, "First Measurements of Inclusive Muon Neutrino Charged Current Differential Cross Sections on Argon," *Phys. Rev. Lett.*, vol. 108, p. 161802, 2012.

[87] M. Del Tutto, *First Measurements of Inclusive Muon Neutrino Charged Current Differential Cross Sections on Argon at 0.8 GeV Average Neutrino Energy with the MicroBooNE Detector*. PhD thesis, Oxford U., 2019.

[88] P. Abratenko *et al.*, "First Measurement of Inclusive Muon Neutrino Charged Current Differential Cross Sections on Argon at E_ν ∼0.8 GeV with the MicroBooNE Detector," *Phys. Rev. Lett.*, vol. 123, no. 13, p. 131801, 2019.

[89] S. Gardiner, "Mathematical methods for neutrino cross-section extraction," *FERMILAB-PUB-23-692-CSAID*, 1 2024.

[90] D. Heck, J. Knapp, J. N. Capdevielle, G. Schatz, and T. Thouw, "CORSIKA: A Monte Carlo code to simulate extensive air showers," *FZKA-6019*, 2 1998.

[91] T. Huege and T. Pierog, "Corsika." `https://www.iap.kit.edu/corsika/`.

[92] D. E. Groom, N. V. Mokhov, and S. I. Striganov, "Muon stopping power and range tables 10-MeV to 100-TeV," *Atom. Data Nucl. Data Tabl.*, vol. 78, pp. 183–356, 2001.

[93] R. Acciarri *et al.*, "Michel Electron Reconstruction Using Cosmic-Ray Data from the MicroBooNE LArTPC," *JINST*, vol. 12, no. 09, p. P09014, 2017.

[94] P. Abratenko *et al.*, "Determination of muon momentum in the MicroBooNE LArTPC using an improved model of multiple Coulomb scattering," *JINST*, vol. 12, no. 10, p. P10010, 2017.

[95] G. D'Agostini, "A Multidimensional unfolding method based on Bayes' theorem," *Nucl. Instrum. Meth. A*, vol. 362, pp. 487–498, 1995.

[96] C. Andreopoulos, C. Barry, S. Dytman, H. Gallagher, T. Golan, R. Hatcher, G. Perdue, and J. Yarba, "The GENIE Neutrino Monte Carlo Generator: Physics and User Manual," *FERMILAB-FN-1004-CD*, 10 2015.

[97] T. M. Collaboration, "First Muon-Neutrino Charged-Current Inclusive Differential Cross Section Measurement for MicroBooNE Run 1 Data," *MICROBOONE-NOTE-1045-PUB*, 8 2018.

[98] H. Hausner, M. J. Jung, G. Putnam, N. Rowe, and J. Zettlemoyer, "Search for a long-lived dimuon resonance in the numi beam at the icarus experiment: Technical note." https://sbn-docdb.fnal.gov/cgi-bin/sso/ShowDocument?docid=34448.

[99] S. Dolan *et al.*, "Gundam." https://github.com/gundam-organization/gundam.

[100] M. B. Avanzini, "Gundam: an ideal binned likelihood fitter framework for cross-section analyses." https://sbn-docdb.fnal.gov/cgi-bin/sso/RetrieveFile?docid=32028&filename=GUNDAMforXSEC%40ICARUS.pdf&version=1.

[101] B. Howard and J. Kim, "Updates to 1munp0pi analysis." https://sbn-docdb.fnal.gov/cgi-bin/sso/ShowDocument?docid=32777.

[102] B. Howard and J. Kim, "Cc0pi x-sec analysis updates." https://sbn-docdb.fnal.gov/cgi-bin/sso/ShowDocument?docid=34502.

[103] P. Vilain *et al.*, "Precision measurement of electroweak parameters from the scattering of muon-neutrinos on electrons," *Phys. Lett. B*, vol. 335, pp. 246–252, 1994.

[104] S. L. Glashow and S. Weinberg, "Natural Conservation Laws for Neutral Currents," *Phys. Rev. D*, vol. 15, p. 1958, 1977.

[105] F. J. Hasert *et al.*, "Observation of Neutrino Like Interactions Without Muon Or Electron in the Gargamelle Neutrino Experiment," *Phys. Lett. B*, vol. 46, pp. 138–140, 1973.

[106] S. Sarantakos, A. Sirlin, and W. J. Marciano, "Radiative Corrections to Neutrino-Lepton Scattering in the SU(2)-L x U(1) Theory," *Nucl. Phys. B*, vol. 217, pp. 84–116, 1983.

[107] J. L. Lucio, A. Rosado, and A. Zepeda, "Neutrino Charge in the Linear R(xi) Gauge," *Phys. Rev. D*, vol. 29, p. 1539, 1984.

[108] L. G. Cabral-Rosetti, J. Bernabeu, J. Vidal, and A. Zepeda, "Charge and magnetic moment of the neutrino in the background field method and in the linear R-L(xi) gauge," *Eur. Phys. J. C*, vol. 12, pp. 633–642, 2000.

[109] K. Fujikawa and R. Shrock, "On a neutrino electroweak radius," *Phys. Rev. D*, vol. 69, p. 013007, 2004.

[110] J. Papavassiliou, J. Bernabeu, D. Binosi, and J. Vidal, "The Effective neutrino charge radius," *Eur. Phys. J. C*, vol. 33, pp. S865–S867, 2004.

[111] D. Hongyue, "DUNE Near Detector with focus on cross section and prospects from the oscillation perspective," *PoS*, vol. NuFact2017, p. 058, 2018.

[112] V. De Romeri, K. J. Kelly, and P. A. N. Machado, "DUNE-PRISM Sensitivity to Light Dark Matter," *Phys. Rev. D*, vol. 100, no. 9, p. 095010, 2019.

[113] G. Radel and R. Beyer, "Neutrino electron scattering," *Mod. Phys. Lett. A*, vol. 8, pp. 1067–1088, 1993.

[114] J. N. Bahcall, M. Kamionkowski, and A. Sirlin, "Solar neutrinos: Radiative corrections in neutrino - electron scattering experiments," *Phys. Rev. D*, vol. 51, pp. 6146–6158, 1995.

[115] M. Passera, "QED corrections to neutrino electron scattering," *Phys. Rev. D*, vol. 64, p. 113002, 2001.

[116] M. Passera, "QED corrections to the scattering of solar neutrinos and electrons," *J. Phys. G*, vol. 29, pp. 141–152, 2003.

[117] A. Sirlin and A. Ferroglia, "Radiative Corrections in Precision Electroweak Physics: a Historical Perspective," *Rev. Mod. Phys.*, vol. 85, no. 1, pp. 263–297, 2013.

[118] A. Ferroglia, G. Ossola, and A. Sirlin, "The Electroweak form-factor kappa-hat (q**2) and the running of sin**2 theta-hat (W)," *Eur. Phys. J. C*, vol. 34, pp. 165–171, 2004.

[119] J. Erler and R. Ferro-Hernández, "Weak Mixing Angle in the Thomson Limit," *JHEP*, vol. 03, p. 196, 2018.

[120] O. Tomalak and R. J. Hill, "Theory of elastic neutrino-electron scattering," *Phys. Rev. D*, vol. 101, no. 3, p. 033006, 2020.

[121] I. Bischer and W. Rodejohann, "General Neutrino Interactions at the DUNE Near Detector," *Phys. Rev. D*, vol. 99, no. 3, p. 036006, 2019.

[122] C. Giunti and A. Studenikin, "Neutrino electromagnetic interactions: a window to new physics," *Rev. Mod. Phys.*, vol. 87, p. 531, 2015.

[123] V. Cristovao, "Dune prism." `https://doi.org/10.5281/zenodo.2642370`.

[124] L. Fields, "Dune fluxes." `https://home.fnal.gov/~ljf26/DUNEFluxes/`.

[125] V. Hewes *et al.*, "Deep Underground Neutrino Experiment (DUNE) Near Detector Conceptual Design Report," *Instruments*, vol. 5, no. 4, p. 31, 2021.

[126] CERN, "Cosmic rays: particles from outer space." `https://home.cern/science/physics/cosmic-rays-particles-outer-space`.